Quantum Hall effect

in a strongly disordered system

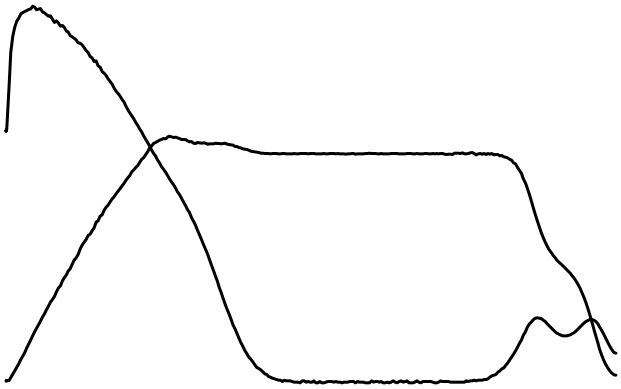

Dissertation

zur Erlangung des akademischen Grades des
Doktors der Naturwissenschaften
an der Universität Konstanz
Fachbereich Physik

vorgelegt von

Markus Weiss

Tag der mündlichen Prüfung: 1.10.2004

Referent: Prof. Dr. P. Wyder
Referent: Prof. Dr. G. Schatz

Contents

Chapter 1

Introduction

In 1980 Klaus von Klitzing, who was investigating the magneto-galvanometric properties of the two-dimensional electron gas in high quality Silicon MOSFETs at the Grenoble High Magnetic Field Laboratory, discovered that the anomalies that he had observed in the Hall resistivity when sweeping the gate voltage were actually plateaus at integer fractions of the fundamental resistance quantum $R_K = h/e^2 = 25812.807\ \Omega$ [1]. The plateaus were accompanied by a vanishing longitudinal resistivity. It turned out, that the quantization of the Hall resistivity was exact to one part in 10^8, a fact which has since then made this *quantum Hall effect* a useful tool to maintain the standard of electrical resistance. Together with the exact value of the speed of light c, the resistance quantum has also been used to determine a precise value of the fine structure constant $\alpha = e^2/\hbar c$.
It soon became clear, that the high precision of the quantization of the Hall resistivity was due to localization of charge carriers in a disorder potential. Surprisingly, in the case of the quantum Hall effect, it is randomness and imperfection, that leads to a high precision effect - a necessarily dirty semiconductor sample allowed to determine precise values of physical constants of fundamental importance.
Although a basic theoretical understanding was established already some years after its discovery, the quantum Hall effect continues to attract a considerable interest both in experimental and theoretical physics. On the theoretical side, a global, unified theory for the quantum Hall effect is still missing, and experimentally many new features (e. g. the fractional quantum Hall effect [2] and very recently the discovery of zero resistance states at small magnetic fields under microwave illumination [3]) have been and continue to be discovered thanks to an enormous progress in sample fabrication technology. The perfection of the most widely used molecular beam epitaxy (MBE) technique (used to grow high quality AlGaAs/GaAs modu-

lation doped heterostructures) has allowed to push the value of the carrier mobility from values of 10^4 cm^2/Vs, which were common at the time of the discovery of the quantum Hall effect, to values of the order of 10^7 cm^2/Vs, which are available nowadays.
In the present work, we have gone the opposite way, in fabricating a dedicated low mobility, strongly disordered sample with an electron mobility of about 2000 cm^2/Vs. Using a radically different approach of creating a confinement potential, we were furthermore able to create a GaAs based quantum well system without long range potential fluctuations, that complicate a lot of experiments in the widely used AlGaAs/GaAs heterostructures. This quantum well system, which has almost remained unnoticed in the literature has allowed us to observe some new features of the integer quantum Hall effect, that shed a different light onto this effect that, more than 20 years after its discovery, continues to attract attention from the whole physical community. Working with a new kind of sample, that due to the strong disorder potential is moreover difficult to describe theoretically, we are aware that there is little theoretical work in the literature, that can directly be applied to our data. We hope that our work will show that dedicated, strongly disordered samples can elucidate different aspects of the integer quantum Hall effect, and that it will stimulate interest in the quantum Hall effect in strongly disordered systems.

Chapter 2

The integer quantum Hall effect - an overview

In the following we give some simple theoretical models which reflect the properties of a two-dimensional electron gas (2DEG) in a strong magnetic field. Starting from the Drude model, we show how Landau quantization occurs in the simplest quantummechanical model, and give a rather simplified model (the high field model) that incorporates a disorder potential and shows the occurrence of localized and extended states. The sequence of different plateaus seen in the Hall resistivity in a field sweep experiment can be described theoretically as a sequence of phase transitions between different quantum Hall states. This results in scaling laws for the transport coefficients in the proximity of the transition points, that can be verified experimentally. An open question is how the quantum Hall effect will vanish at small magnetic fields in the limit of zero temperature. We will present one possibility, the levitation of extended states. We will mention the gauge argument put forward by R. Laughlin, that explains the exact quantization of the Hall conductivity by gauge invariance. Last we will mention the open conductor approach to the quantum Hall effect by M. Büttiker, that describes electronic transport in terms of reflection and transmission of charge carriers.

2.1 Classical theories

As there are some limiting cases where a classical description of a disordered two-dimensional electron systems is very instructive for the understanding of the quantum Hall effect, we will give the results of a classical description of an electron in a magnetic field.

2.1.1 The Drude model

The basic theoretical model for electrical transport is the Drude model, which, although a very simplified model, still gives a reasonably good description of transport at high temperature and usually is a good starting point for more sophisticated models. Electrons are treated as classical particles moving under the influence of external fields and a friction term represented by an average scattering time τ:

$$m\dot{\mathbf{v}} = -e\ \mathbf{v} \times \mathbf{B} - e\ \mathbf{E} - \frac{m}{\tau}\mathbf{v} \tag{2.1}$$

Here m is the electron mass, $\mathbf{v}$ the velocity vector, $\mathbf{B}$ and $\mathbf{E}$ are the magnetic and electric field vectors, respectively. Choosing $\mathbf{B}$ along the z-direction ($\mathbf{B} = (0, 0, B)$), setting $\dot{\mathbf{v}} \equiv 0$ (steady state condition) and using the equation $\mathbf{j} = -en\mathbf{v}$ for the current density, we get the following expression for the conductivity tensor $\underset{\approx}{\sigma}$ ($\mathbf{j} = \underset{\approx}{\sigma}\mathbf{E}$):

$$\begin{gathered} \underset{\approx}{\sigma} = \begin{pmatrix} \sigma_{xx} & -\sigma_{yx} & 0 \\ \sigma_{yx} & \sigma_{xx} & 0 \\ 0 & 0 & \sigma_{zz} \end{pmatrix} \\ \sigma_{xx} = \frac{\sigma_0}{1 + (\omega_c\tau)^2}, \qquad \sigma_{zz} = \sigma_0, \qquad \sigma_{yx} = \sigma_0\frac{\omega_c\tau}{1 + (\omega_c\tau)^2} = \sigma_{xx}\omega_c\tau, \\ \sigma_0 = \frac{ne^2\tau}{m} = ne\mu \end{gathered} \tag{2.2}$$

with the mobility $\mu = e\tau/m$ and the cyclotron frequency $\omega_c = eB/m$. As experiments usually measure resistances, it is convenient to convert these results to the corresponding resistivity tensor $\underset{\approx}{\rho}$:

$$\begin{gathered} \underset{\approx}{\rho} = (\underset{\approx}{\sigma})^{-1} = \begin{pmatrix} \rho_{xx} & \rho_{xy} & 0 \\ -\rho_{xy} & \rho_{xx} & 0 \\ 0 & 0 & \rho_{xx} \end{pmatrix} \\ \rho_{xx}(B) = \rho_0 = \frac{1}{\sigma_0}, \quad \rho_{xy}(B) = \frac{B}{en}. \end{gathered} \tag{2.3}$$

The Drude model gives a magnetic field independent diagonal resistivity ρ_{xx} and a Hall (transverse) resistivity ρ_{xy} which is linear in B.

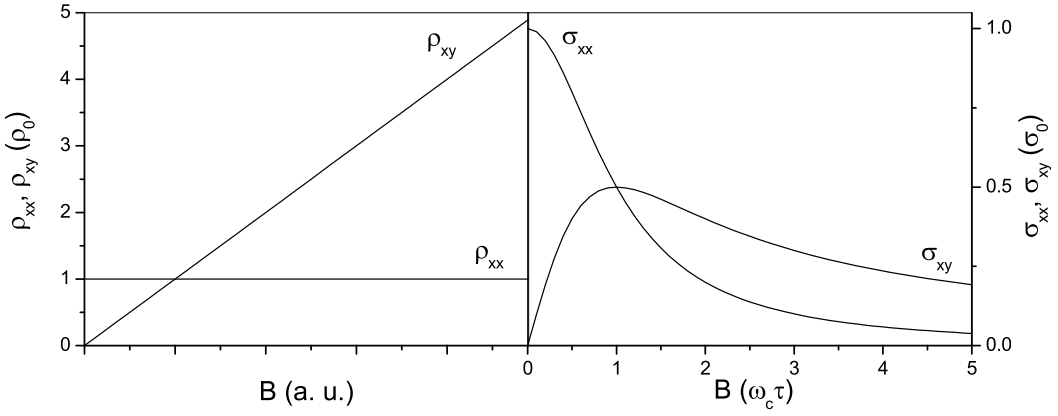

Figure 2.1: Resistivities and conductivities in the Drude model

2.1.2 Classical electron trajectories

To find the actual electron trajectories one has to solve the equation of motion for a classical charged particle under the influence of a magnetic and electric field, as it is done e.g. in [4] using the Hamilton formalism. The results for a homogenous magnetic field along z ($\mathbf{B} = (0, 0, B)$) and a homogenous electric field along x ($\mathbf{E} = (E, 0, 0)$) are:

$$\begin{aligned} x(t) = X(t) + \zeta(t), \qquad & y(t) = Y(t) + \eta(t) \\ X(t) = X, \qquad & Y(t) = Y + v_D t \\ \zeta(t) = R\sin(\omega_c t + \alpha) + \frac{v_D}{\omega_c}, \qquad & \eta(t) = R\cos(\omega_c t + \alpha) \end{aligned} \tag{2.4}$$

$v_D = -E/B$ is called the drift velocity. The coordinates have been separated into a slowly varying part $(X(t), Y(t))$, and a rapidly varying part $(\zeta(t), \eta(t))$, where the slow motion is a constant drift with velocity v_D along y, and the rapid motion is a cyclotron motion around the center coordinates $(X + v_D/\omega_c, Y)$ with the frequency ω_c. The electron performs a cycloid motion, drifting perpendicular both to the magnetic and electric field, along an equipotential line.

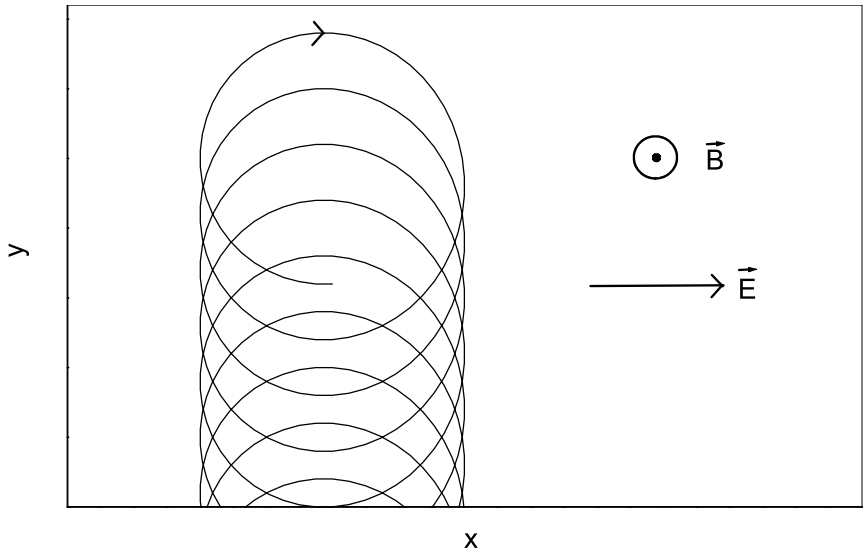

Figure 2.2: Electron trajectory in a classical picture

2.2 Quantum mechanical treatment

The origins of the quantum Hall effect can only be found by a quantum mechanical calculation. For this, a starting point is the Hamiltonian for an electron in a homogenous magnetic field:

$$\hat{H} = \frac{1}{2m}\left(\hat{\mathbf{p}} - e\hat{\mathbf{A}}\right)^2 + V\left(\hat{\mathbf{r}}\right). \tag{2.5}$$

Choosing the direction of $\mathbf{B}$ along the z-axis, one can use the Landau gauge for the vector potential: $\mathbf{A} = (0, Bx, 0)$. This gauge is appropriate for systems with translational symmetry along y. Another possible gauge is the symmetric gauge $\mathbf{A} = \frac{1}{2}\mathbf{B} \times \mathbf{r}$, which is a good choice for systems with axial symmetry.
Assuming further that $V(\mathbf{r}) = V(x, y) + V_z(z)$, the Schrödinger equation will separate into a part depending on z, and the remaining, now effectively two-dimensional part depending on x and y. Note that $V_z(z)$ can be zero (as assumed by Landau for the 3D case), or can be given by a confinement potential imposed e. g. by a semiconductor heterostructure, therefore creating a "real" 2D system. In any of the two cases the results for the remaining 2D problem in the (x,y)-plane are the same.

2.2.1 Landau model

In the case originally considered by Landau, the external potential is assumed to vanish ($V(\mathbf{r}) = 0$, no electric field). The Hamiltonian then doesn't depend on y, we get a plane wave solution in the y-direction, and in the x-direction the problem becomes equivalent to a harmonic oscillator:

$$\hat{H} = \frac{\hat{p}_x^2}{2m} + \frac{m\omega_c^2}{2}(\hat{x} - X)^2 \tag{2.6}$$

with the center coordinate $X = -l_B^2 k (l_B = \sqrt{\hbar/eB})$, and the solution

$$\begin{aligned} \Psi(x,y) &= \frac{1}{\sqrt{W}} e^{iky} \phi_n(x) \\ k = \frac{2\pi}{W} m, \qquad \phi_n(x) &= \frac{1}{l_B} e^{-x^2/2l_B^2} H_n(x/l_B). \end{aligned} \tag{2.7}$$

W is the extension of the system in y-direction, m is an integer, and H_n are the Hermite polynomials. The states $\Psi(x,y)$ are delocalized (plane waves) in y-direction, and localized (harmonic oscillator states) around X in x-direction. Note however that the shape of the wave functions depend strongly on the gauge used for $\mathbf{A}$. The energy eigenvalues

$$\epsilon_n = \hbar\omega_c \left(n + \frac{1}{2} \right) \tag{2.8}$$

are called *Landau levels*.
As the energy of an electron is independent of its x-position, the eigenvalues are infinitely degenerate, and the density of states (DOS)

$$\rho(E) = \lim_{L,W\to\infty} \frac{1}{L \cdot W} \sum_{n,k} \delta(E - \epsilon_n) \tag{2.9}$$

is ill-defined (L is the extension of the system in x-direction). To get around this problem, one considers only states with

$$-\frac{L}{2} \leq X \leq \frac{L}{2} \tag{2.10}$$

and takes the limit $L \longrightarrow \infty$ afterwards. This method, also called the Landau counting of states, gives a DOS consisting of equidistant δ-peaks separated by $\Delta\epsilon = \hbar\omega_c$ and a degeneracy of $2\pi l_B^2$ per Landau level:

$$\rho\,(E) = \frac{1}{2\pi l_B^2} \sum_n \delta(E - \epsilon_n) \tag{2.11}$$

The actual wave function is delocalized across the sample along y, and localized in an area of width $\sqrt{n+1/2}\, l_B$ around X in x-direction.
Note that using the symmetric gauge for $\mathbf{A}$, one gets the same energy Eigenvalues, but the wavefunctions are localized on a circle with radius $\sqrt{2m}\, l_B$ (m is a non-negative integer) [5].

2.2.2 Disorder

In real semiconductor samples some kind of disorder potential, caused for example by lattice defects or ionized donors is always present. The exact calculation of the effect of a random potential onto the energy spectrum of the problem is not possible in a straightforward way, on one hand because it is by far not clear what shape the disorder potential should have (one can think of the whole range from an unscreened $1/r$ Coulomb potential to a completely screened δ-potential), and on the other hand the mathematical effort even for the simplest situation of a random arrangement of δ-potentials is considerable. It is clear however, that the degeneracy of the Landau levels will be lifted by an additional potential, and the delta-peaks in the density of states transform into structures with a finite width. A prominent approach to calculate the shape of the disorder-broadened Landau levels is the self consistent Born approximation (SCBA), where only single scattering events are taken into account. The SCBA gives an elliptic function as shape for the broadened Landau levels, models including multiple scattering events [6] give a Gaussian shape

$$\rho(E) = \frac{1}{2\pi l_B^2} \sum_n \frac{\sqrt{2/\pi}}{\Gamma_n} \exp\left[-2\left(E-\epsilon_n\right)^2/\Gamma_n^2\right] \tag{2.12}$$

where Γ_n is a Landau level dependent width. In addition to the broadening of the Landau levels, a disorder potential will change the nature of most of the electronic states in the Landau level. Except the states in the middle of the level, which will be extended over the sample, all electronic states will localize. This can be shown easily with the help of the semi-phenomenological high field model [4].

2.2.3 The high field model

Using the separation of the coordinates introduced in chapter 2.1.2, the Hamiltonian for an electron in a magnetic field and a disorder potential

$V(x, y)$ looks as follows:

$$\hat{H} = \frac{m\omega_c^2}{2}\left(\zeta^2 + \eta^2\right) + V(X + \zeta, Y + \eta) \tag{2.13}$$

The x- and y- coordinates do not commute

$$[X, Y] = il_B^2, \qquad [\zeta, \eta] = -il_B^2. \tag{2.14}$$

Taking the limit $B \to \infty$, one can neglect ζ and η in the argument of V, as their expectation values are of the order of $l_B \propto 1/\sqrt{B}$. The Hamiltonian then separates, and the first part is equivalent to the Landau level energies

$$\hat{H} = \epsilon_n + V(X, Y). \tag{2.15}$$

As the commutator of $[X, Y]$ is proportional to $1/B$, X and Y can be treated as classical variables for $B \to \infty$, and the problem can be calculated classically, resulting in the following equations of motion

$$\dot{X} = \frac{l_B^2}{\hbar} \cdot \frac{\partial V}{\partial Y}, \qquad \dot{Y} = -\frac{l_B^2}{\hbar} \cdot \frac{\partial V}{\partial X}. \tag{2.16}$$

This implies that dV/dt vanishes, so the potential energy of the electron is

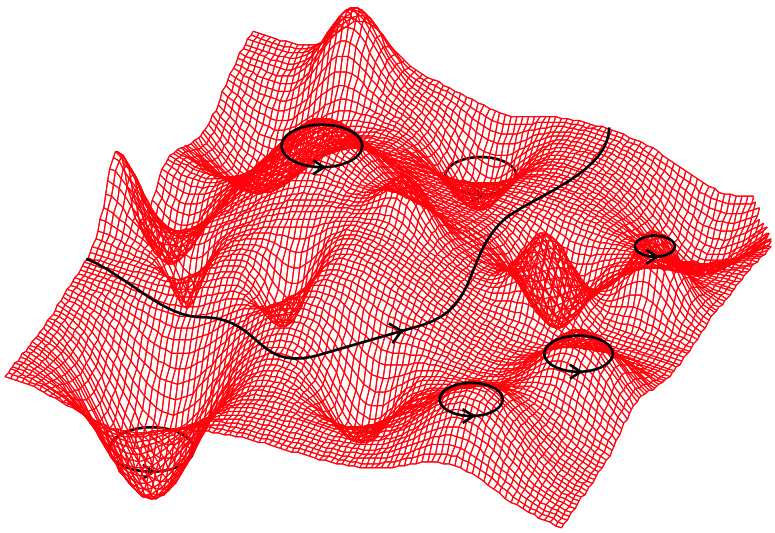

Figure 2.3: Disorder potential with closed orbits (localized states) and open orbits (extended states)

constant. We can say that, in the limit of high B, the electron is delocalized on an area of approxmately l_B^2 and moves on the equipotential lines of the

disorder potential. If V is symmetric around $V = 0$, then electron orbits for $E \neq \hbar\omega_c/2$ (lowest Landau level), will circle around valleys or peaks of the disorder potential and will therefore be localized as shown in figure 2.3, and only for $E = \hbar\omega_c/2$ the trajectory will traverse the sample and give a delocalized state[1]. The electronic density of states for the Landau model with and without disorder is sketched in figure 2.4. Depending on the value of E_F

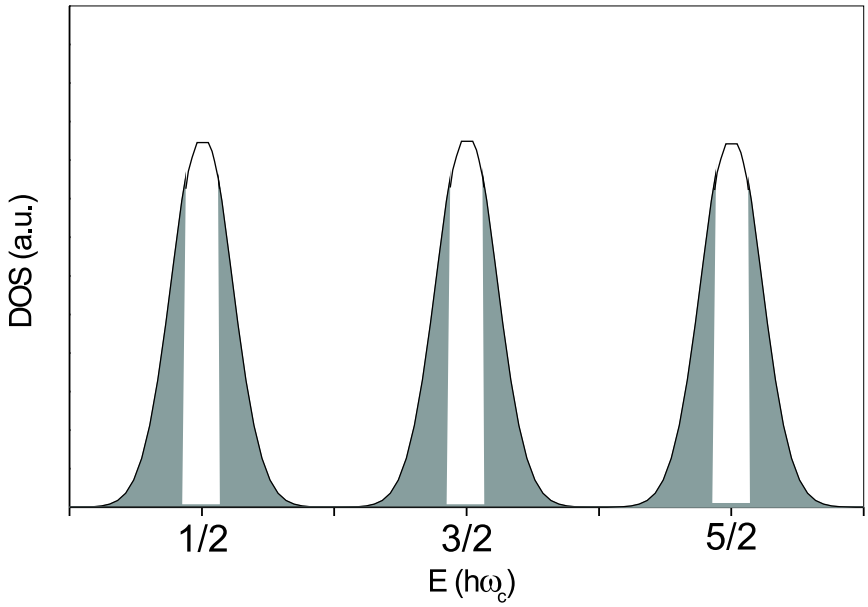

Figure 2.4: Schematic density of states for the disordered Landau model. The grey regions represent localized states.

with respect to $\hbar\omega_c$, there will be either localized states in the vicinity of the Fermi energy and the system will be insulating, or extended states, resulting in the sample to show a metallic-like behavior. Changing the ratio of E_F to $\hbar\omega_c$, either by changing the carrier density or by sweeping the magnetic field, will cause a series of transitions between metallic and insulating states.
Note that because V will rise strongly at the boundaries of a sample in x- and y-direction (as only in this case the wave function will vanish outside the sample), there will always be an extended state for all ratios of E_F to $\hbar\omega_c$ propagating at the edge of the sample. This edge state can carry a current, even if all other states around E_F are localized.

[1] Strictly speaking this is only true for a sample of infinite size L, a finite size sample will show a narrow band of extended states with a finite width around the Landau level center.

2.3 Transitions between quantum Hall states

At low temperatures the DOS of a 2DEG will decay into areas of extended states (in the vicinity of the Landau level centers) and areas of localized states, that surround the former (in the Landau level tails). We can identify two extremal transport regimes: the plateau region, when the Fermi energy is situated in a range of localized states, and the transition region between two plateaus, when the Fermi energy lies in an area of extended states. Electron

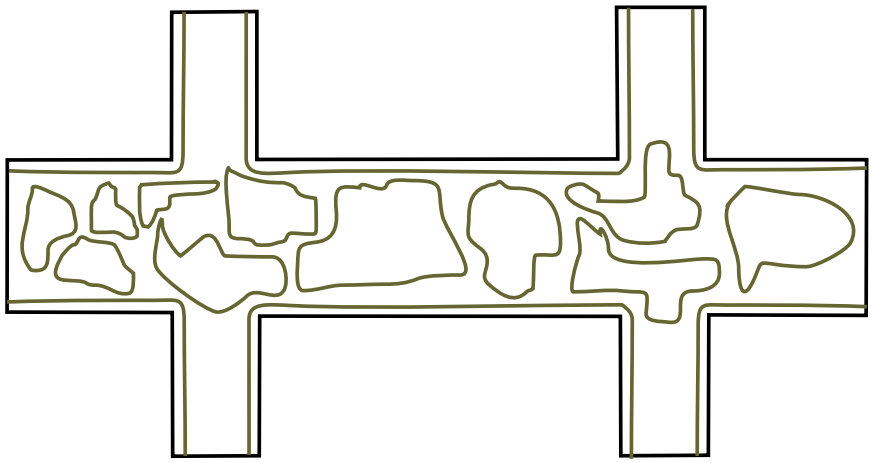

Figure 2.5: electron trajectories for the plateau region

trajectories for the plateau regime are shown in figure 2.5. There is no net current flowing in the bulk of the sample, and transport takes place only in the edge states of the sample. As there are no extended states in the vicinity of E_F, the longitudinal conductivity σ_{xx} vanishes. The Hall conductivity is determined by the number n of occupied Landau levels below E_F, and can be shown to be equal to $n \cdot e^2/h$. In the transition regime, when E_F lies in a region of extended states, electron transport in the bulk of the sample is possible, and therefore dissipative currents will flow in the sample giving a nonzero longitudinal conductivity and a Hall conductivity that lies between two quantized values. Typical electron trajectories for the transition region are shown in figure 2.6. An interesting question is, how the crossover between these two regimes will look like. According to the high field model (chapter 2.2.2), electron trajectories in the plateau region are closed, with the diameter of the closed loops increasing as the Fermi energy approaches an area of extended states. For a real world (finite size) sample, the system should enter the transition regime as soon as the average diameter of the electron trajectories exceeds the sample size L. Note that for finite temperatures, L has to be

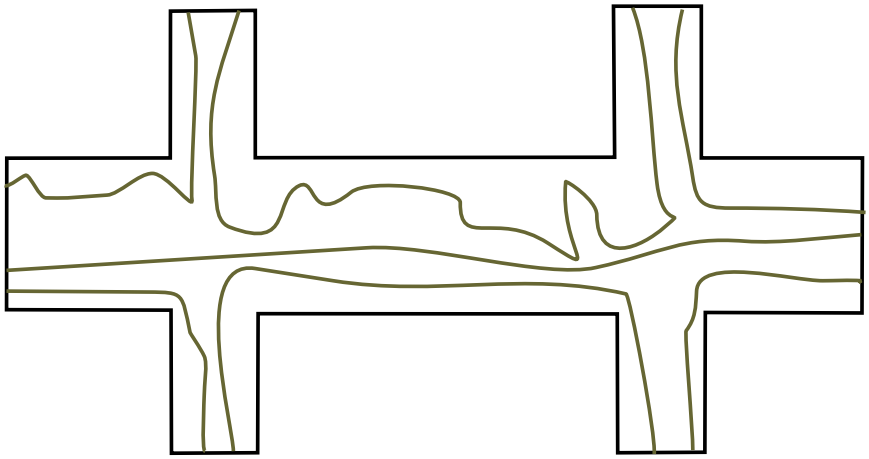

Figure 2.6: electron trajectories for the transition region between two plateaus

replaced by an effective sample size, which corresponds to the phase coherence length of the charge carriers [7]. This length, which is usually given by L_Φ or L_{in}, depends on temperature with a powerlaw ($L_{in} = \sqrt{D\tau_{in}} \propto T^{-\frac{p}{2}}$). Theoretically the transition between two quantum Hall states is being described as a continuous quantum phase transition, order parameter being the localization length ξ, which corresponds to the mean diameter of a closed electron trajectory. At the transition point, when different localized trajectories come close to each other, electrons are able to tunnel between different localized states close to a saddle point. In this picture, the transition between the two regimes is a quantum-percolation transition. The order parameter ξ has been predicted to diverge with a power law at the critical energy of the transition: $\xi \propto |E - E_c|^{-\nu}$. The most prominent model for the calculation of the critical exponent ν is the Chalker-Coddington model, which calculates the percolation exponent for a regular lattice of saddle points [8]. The result for an analytic solution is $\nu = 7/3$, a value which has been verified numerically by lattice models for different disorder potentials. The critical conductivity $\sigma_{xx}(E_c)$ was found to be $e^2/2h$.
In a typical quantum Hall experiment one therefore sees a series of phase transitions between different plateau states, with a values of $\sigma_{xx} = 0$ in the two neighboring plateau regions, reaching a value of $\sigma_{xx} = 1/2$ at the transition field B_c. B_c corresponds to the critical energy $E_c = \hbar\omega_c$. As an electronic state has to be considered extended as soon as its localization length is larger than the effective sample size ($\xi > L_{in}$), the width of the area of extended states around the critical energy E_c will shrink with decreasing temperature. As L_{in} increases with a powerlaw for decreasing temperature, the area of

extended states should shrink to zero width for $T \to 0$. The transition region between two quantum Hall states should therefore become more and more narrow for decreasing temperature. As it was shown by Pruisken [9], the transport coefficients in the transition region should be determined by a regular function that only depends on a singe scaling variable:

$$\rho_{ij}(B,T) \propto f(\kappa), \quad \kappa = |B - B^*| \cdot T^{-\mu}, \quad \mu = \frac{p}{2\nu} \tag{2.17}$$

This makes it possible to observe the product of the localization length exponent ν and the exponent of the inelastic scattering length p for example in the half width $\Delta B_{1/2}$ of the peak in ρ_{xx}, or the slope of ρ_{xy} at B_c:

$$\Delta B_{1/2} \propto T^{\mu}, \quad \frac{\partial \rho_{xy}}{\partial B}|_{B=B_0} \propto T^{-\mu} \tag{2.18}$$

Theoretical calculations predict a value of $\mu = 0.43$.

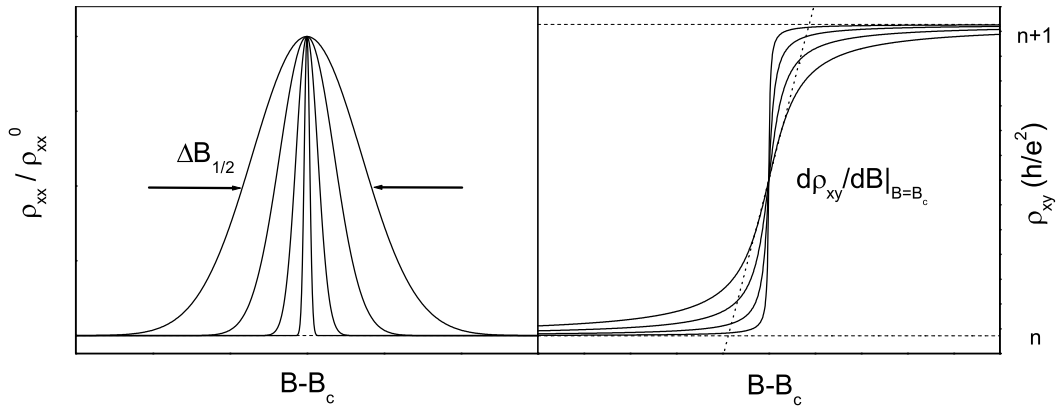

Figure 2.7: Sharpening of the transition between two quantum Hall plateaus for decreasing temperature

The critical field B_c usually corresponds to a magnetic field value where the Fermi energy E_F coincides with the center of a Landau level. However, there exists an exception to this rule.

2.4 Low field quantum Hall effect

In the limit $T \to 0$ the single parameter localization theory predicts all two-dimensional systems to be localized at $B = 0$, there can be no extended states at zero field. For the quantum Hall effect in high magnetic fields however, extended states are essential, and their existence is well established. The

question is what will happen to the extended states that are connected with the Landau level centers, as the magnetic field is decreased. Theoretically the possibility that these states just dissappear is difficult to establish. It were R. Laughlin [10] and D. Khmelnitzkii [11] who suggested that these extended states will float up in energy as the magnetic fields approaches zero. The values of the magnetic field, where the extended state associated with the n-th Landau level will cross the Fermi energy when floating up was taken to be the value where the Drude Hall conductivity corresponds to the quantum value $(n + 1/2) \cdot e^2/h$. This *floating up scenario* therefore predicts quantum Hall phases to exist even at low magnetic field ($\omega_c\tau < 1$). As will be shown in chapter 3.2.2, a necessary condition for the observability of a Hall plateau is a value of $\sigma_{xx} \ll 1$. As the only available microscopic mechanism, that could lead to a decrease of σ_{xx} in low magnetic fields is weak localization, which gives much smaller corrections than strong localization that occurs in high fields, the condition $\sigma_{xx} \ll 1$ is usually not fulfilled at experimentally accessible temperatures, and the quantum Hall effect at low magnetic fields cannot be observed [12]. The only experimental observations

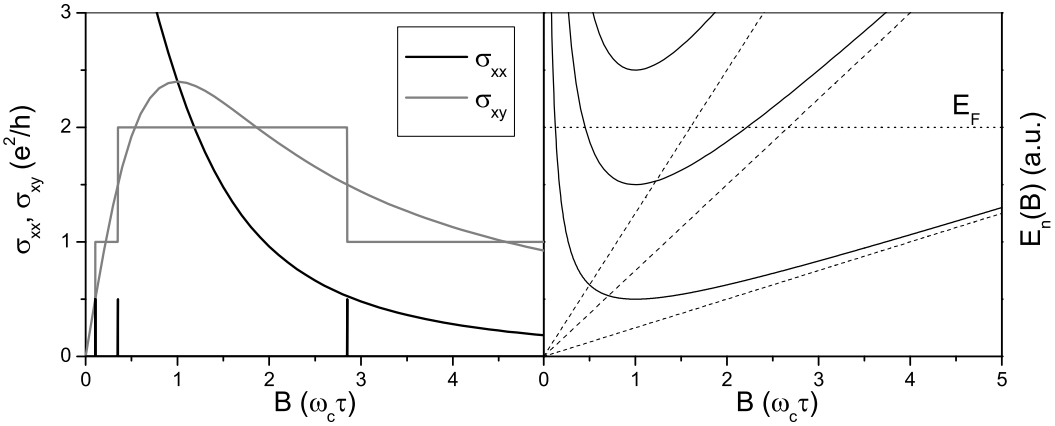

Figure 2.8: Left: Magnetoconductance for a quantum Hall system according to the floating up scenario, in the limit of very high temperature (Drude) and zero temperature. Right: Extended states in the floating up scenario. Dashed lines represent the conventional Landau levels. Any time an extended state crosses the Fermi level, there will be a quantum Hall transition visible in the transport data.

of a quantum Hall transition at low magnetic fields were made in strongly disordered systems, that only show a single quantum Hall phase, and where a clear transition from the low field insulating state to the corresponding quantum Hall plateau at $\sigma_{xy} = 1$ exists [13]. Transitions between higher

quantum Hall states have only been observed in the high field regime ($\omega_c\tau > 1$) up to now.
The transport coefficients for a system in the limit $T \to 0$, according to the floating up scenario, are shown in figure 2.8.

2.5 Gauge arguments

In one of the first theoretical papers dealing with the quantum Hall effect [14], R. Laughlin proposed an explanation for the exact quantization of the Hall conductance that was based on gauge considerations. An extension of his paper was published by B. Halperlin [15] later.
Both authors consider a two-dimensional system in a continuous but multiply connected geometry like a cylinder or ring geometry, e.g. as shown in figure 2.9. The 2D electron gas is assumed to be subject to a magnetic field

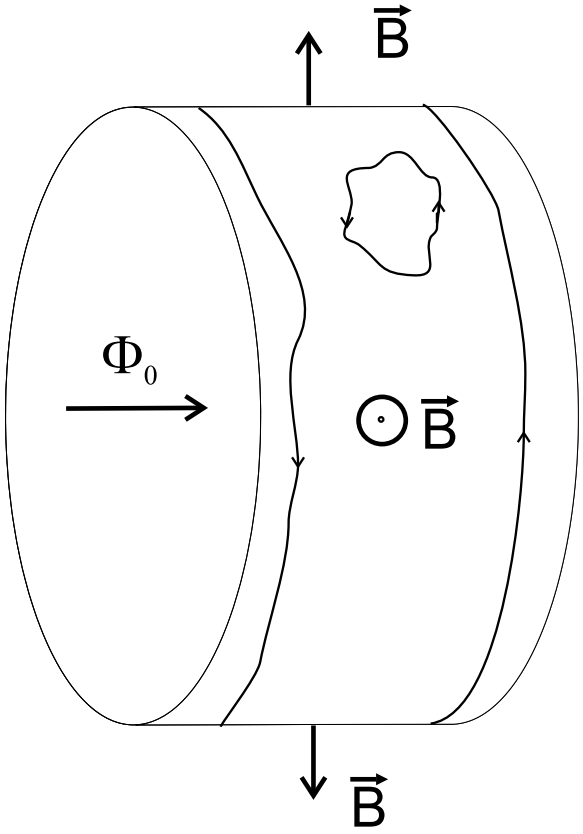

Figure 2.9: Geometry considered by R. B. Laughlin in [14] in his gauge argument for the exact quantization of the Hall conductance.

B perpendicular to its surface, and it is assumed that there is an additional magnetic flux Φ_0, that can be varied freely without changing the value of B, passing through the hole of the system. The system then should be gauge invariant under a flux change $\Delta\Phi$ by an integral multiple of the flux quantum h/e. An adiabatic change of Φ_0 by a single flux quantum should therefore leave the system unchanged. Assuming a DOS as shown in the previous chapter, the effect of the flux change $\Delta\Phi$ onto the electronic wave functions will depend on the nature of the states at the Fermi energy. Localized states will just acquire an additional phase factor, they won't be affected otherwise. Extended states however will suffer an electromotive force, and will be pushed to the exterior of the sample. After Laughlin, gauge invariance requires an integer number of electrons to be transferred across the sample under a flux change $\Delta\Phi = h/e$, which in turn requires the Hall conductivity to be quantized.
It should be noted that some authors claim the gauge argument presented in [14] to be incomplete. After [16], Laughlin's gauge argument has been superceded of what is nowadays called the topological approach to the quantum Hall effect. In this theoretical approach the Hall conductivity is identified with the Chern number, which is a topological invariant (for details see [16],[17] chapter 4).

2.6 The open conductor approach

A theory treating the QHE from a totally different point of view has been worked out by M. Büttiker [18]. Based on a theory of Landauer viewing conductances in terms of transmission of electrons, this theory inherently includes the presence of contacts, a fact which had been neglected in the previously mentioned theories. Associating each contact or probe of the system with an electrochemical potential V_i, the resistance of a four probe conductor is given by

$$R_{kl,mn} = \frac{V_m - V_n}{I}, I = I_k = -I_l, I_m = I_n = 0, \tag{2.19}$$

where the two current contacts are labeled by k and l, the voltage probes m and n. the conductance coefficients are defined by

$$I_m = \sum_n g_{mn}(V_m - V_n). \tag{2.20}$$

The main point of Büttiker's theory is the relation of the conductance coefficients g_{mn} to the transmission probabilities of an electron incident at contact

m:

$$g_{m\neq n} = \frac{e^2}{h} \sum_{\alpha\beta} t_{mn}^{\alpha\beta} \left(t_{mn}^{\alpha\beta}\right)^* = \frac{e^2}{h} Tr\left\{\mathbf{t}_{mn} t_{mn}^{\dagger}\right\} =: \frac{e^2}{h} T_{mn} \tag{2.21}$$

with the transmission probabilities $t_{mn}^{\alpha\beta}$ of an electron incident at point n in quantum state β leaving the conductor at probe m in state α. The main

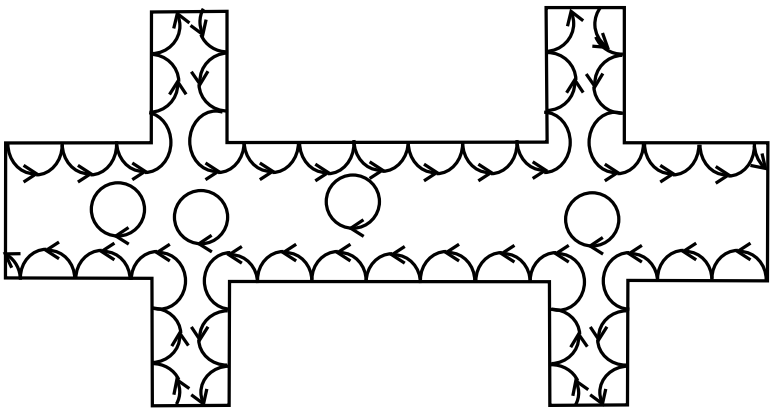

Figure 2.10: Classical representation for perfectly transmitting edge channels and localized, non-current carrying states in the Büttiker picture.

problem in this approach is the calculation of the coefficients T_{mn}, which is simplified a little bit in the case of the quantum Hall effect. In the case of the plateau regime (E_F located in a region of localized states) the only current carrying states are the previously mentioned edge states. As these edge states are moreover sufficiently isolated from all other current carrying states (e. g. on the opposite side of the sample), they are perfectly transmitting ($T_{mn} = 1$), as there are no states an electron could scatter to. As a consequence of this *absence of backscattering* the longitudinal conductance of the sample vanishes ($g_{xx} = 0$), and the Hall conductance corresponds to e^2/h times the number of occupied edge states or *channels* ($g_{xy} = n \cdot e^2/h$). An illustration of the classically calculated electron orbits in the quantum Hall plateau regime is shown in figure 2.10.

Chapter 3

Transport regimes

In the following we will introduce a number of rather specialized theories that, each one in a specific range of magnetic field and temperature, describe the electronic transport in the systems that are subject of this thesis. Their results may be considered as corrections to the classical Drude conductivities (chapter 2.1.1). After the Shubnikov-de Haas oscillations in the resistivity, which occur already at relatively high temperatures where no signs of quantization are visible yet, we will give a short introduction to the theoretical description of the localization problem with and without magnetic field. Then there are single particle interference and interaction corrections to conductivity, that occur at low temperatures and in small magnetic fields, and at last hopping conduction, which dominates in the quantum Hall effect regime at low temperatures for diagonal conductivities close to zero.

3.1 Quasiclassical transport: the Shubnikov-de Haas effect

Due to Landau quantization of the conduction electrons, the density of states at the Fermi energy E_F shows oscillations as soon as the Landau level separation $\hbar\omega_c$ becomes comparable to the disorder broadening $\hbar/\tau$ of a Landau level.[1] As the transport properties of a Fermi system are determined by electrons occupying states in a range of $\approx \pm k_B T$ around E_F, the oscillations in the DOS manifest themselves in the resistivity ρ_{xx} of the system, giving the well known Shubnikov-de Haas oscillations. There is a quantitative theory

[1] Note that we assume the thermal broadening to be negligible with respect to the static disorder broadening, an assumption which is well justified for the strongly disordered system subject of this thesis in the temperature range ($T \leq 4.2$ K) it is being investigated.

of these oscillations in ρ_{xx}, using a calculation in the Kubo-formalism assuming isotropic impurity scattering [19]. Because connected to the Landau level structure of the DOS, the resulting oscillations in $\rho_{xx}(B)$ are periodic in $1/B$. In principle the theory of Roth et al. [19] allows the determination of the effective mass m of the charge carriers (from the temperature dependence of the oscillation amplitude at fixed field), the carrier concentration n^{3D} or the Fermi energy E_F (from the oscillation period in $1/B$) and the elastic scattering time τ or the Dingle temperature T_D (from the envelope of the oscillations at fixed T). As in the systems described in this thesis, only a small number of SdH oscillations were visible, and as they moreover showed no pronounced evolution with temperature, we only used the periodicity of the oscillations to determine the carrier concentration n^{3D}: For the period of the oscillations in ρ_{xx} in a three-dimensional system we get

$$\Delta\left(\frac{1}{B}\right) = \frac{2e}{\hbar}\left(3\pi^2 n^{3D}\right)^{-\frac{2}{3}} \tag{3.1}$$

As a sidenote we should mention that, according to [19], also the Hall resistivity ρ_{xy} will show Shubnikov-de Haas oscillations although they are much less pronounced than in ρ_{xx}. This is a consequence of the fact that ρ_{xy} is only affected by higher order scattering, which has a smaller effect compared to first order scattering, mainly being responsible for the oscillations in ρ_{xx}.

3.2 Localization

As it was mentioned in chapter 2, the mechanism that leads to the vanishing of both ρ_{xx} and σ_{xx} at a quantum Hall plateau is localization in a disorder potential. From a theoretical point of view localization is difficult to treat, because established techniques of perturbation theory cannot be applied due to the lack of a small parameter. The most successful approach to the problem of localization is a field-theoretical approach called the nonlinear sigma model, an approach which has mainly been worked out by Thouless [20] and Wegner [21]. In this theory, in order to be able to average over the disorder potential, it is necessary to do a mathematical transformation (the replica trick) that leaves one with four-dimensional matrix fields in the lagrangian of the problem. Based on this field-theoretical approach, Abrahams et al. [22] were able to derive the famous scaling theory of localization in zero magnetic field. Following this, considerable efforts have been made to describe localization in strong magnetic fields by a similar Ansatz.

3.2.1 Localization in zero magnetic field

The scaling theory of localization describes the dimensionless conductance $g = G/(e^2/h)$ of a sample (more specific: a hyper cube of volume L^d, d being the dimensionality of the system) as the fundamental observable (instead of conductivity) as a function of its size L. The main statement is that the conductance of a system expressed as a function of the appropriate length scale L is determined by a single scaling function:

$$\beta\left(g(L)\right) = \frac{\partial \ln g}{\partial \ln L}. \tag{3.2}$$

This so called β-function allows to calculate the conductance of a system

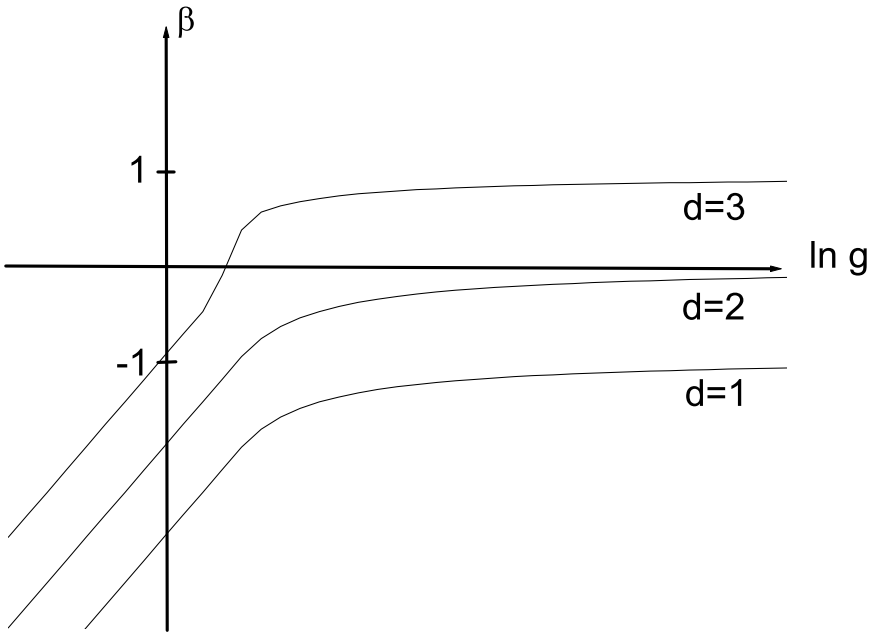

Figure 3.1: Beta function for $d = 1, 2, 3$

in the thermodynamic limit. β depends on the dimensionality of a system. It is sketched for $d = 1, 2, 3$ in figure 3.1. General considerations give the behavior of β for the limiting cases of very large g ($g \gg 1$)

$$g = \sigma L^{d-2} \Rightarrow \beta(g) = d - 2 \tag{3.3}$$

and very small g ($g \ll 1$, the regime of strong localization)

$$g = g_0 \exp\left(-\alpha L\right) \Rightarrow \beta = \ln(g/g_0). \tag{3.4}$$

Microscopic models, usually solving the Hamiltonian for a noninteracting electron in a disorder potential, exist only for the case of small deviations from the ohmic case. It can be seen that in the frame of this theory, a metallic state ($\beta > 0$) can only exist for $d > 2$. On the other hand this means that for $d <= 2$ all systems become localized for large enough L.
As already indicated in chapter 2.3, L corresponds to the real sample size only for the case of zero temperature. It has to be replaced by the coherence length of the electron wave function L_{in} for nonzero temperature.
As the most important result we can note that the scaling theory of localization predicts all systems of dimension $d \leq 2$ to become insulating for large $L \to \infty$ or $T \to 0$, respectively. At zero magnetic field, there can be no delocalized, current carrying states in a two-dimensional system for $T \to 0$.

3.2.2 Localization in a magnetic field

It is evident that the results of the scaling theory of localization are strongly modified in the presence of a magnetic field. As both g_{xx} and g_{xy} are affected by localization (or they are renormalized, theoretically speaking), there are two beta functions β_{xx} and β_{xy}, which give the coupled evolution of the two components of the conductance tensor as a function of L. This has lead to the name of *two parameter scaling* for this theoretical approach. Up to now, the only microscopic calculation for β_{xx} and β_{xy} has been performed by Pruisken and coworkers [23, 24, 25]. Their approach is based on the nonlinear sigma model for the zero field case, which they extended by adding a topological term, proportional to σ_{xy}, to the lagrangian. To calculate β_{xx} and β_{xy}, they used the so called dilute instanton gas approximation, a mathematical method borrowed from quantum-chromodynamics. For $\sigma_{xx} \gg \sigma_{xy}$ their results given in [17], chapter 5 are[2]:

$$\begin{aligned} \beta_{xx} &= \frac{\partial \sigma_{xx}}{\partial \ln L} = \frac{-1}{2\pi^2 \sigma_{xx}} - \sigma_{xx} \underline{D} \exp(2\pi\sigma_{xx}) \cos(2\pi\sigma_{xy}) \\ \beta_{xy} &= \frac{\partial \sigma_{xy}}{\partial \ln L} = -\sigma_{xx} \underline{D} \exp(2\pi\sigma_{xx}) \sin(2\pi\sigma_{xy}) \end{aligned} \tag{3.5}$$

($\underline{D}$ is a constant). An initially purely phenomenological approach to this problem has been undertaken by Khmelnitzkii [26], who visualized the coupled evolution of g_{xx} and g_{xy} with increasing L (the *renormalization group*

[2] Note that we give β_{xx} and β_{xy} in the notation used by Pruisken in [17], writing them as a function of the conductivites and not conductances. As for the case of localization in magnetic field we limit ourselves to two dimensions, the distinction between conductivities and conductances becomes useless

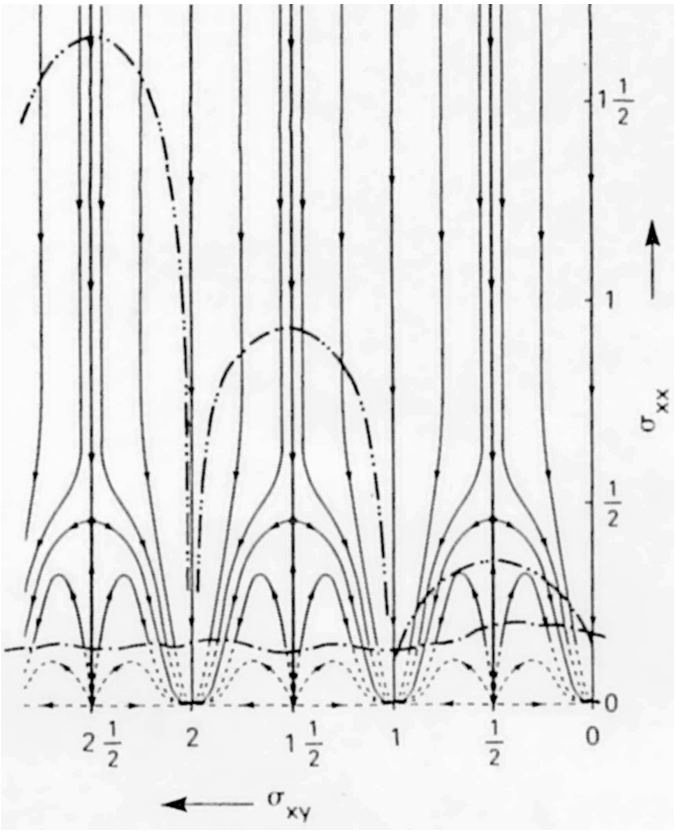

Figure 3.2: Flow diagram given by A. Pruisken in [17] in 1987. The solid lines are the flow lines, the upper dash-dotted lines are the starting point for the renormalization calculated in the SCBA-approximation, and the lower dash-dotted lines are the limit of validity of the renormalization group equations (3.5). Conductivities are given in untis of e^2/h.

flow) in the form of a flow diagram [26], a plot of g_{xx} versus g_{xy}. We reproduce the flow diagram given by A. Pruisken in [17] in figure 3.2.

Despite the fact that microscopic models have turned out to be not very successful for the problem of two parameter scaling, some progress has been made recently by an approach exploiting certain symmetries of the quantum Hall plateau transition. These symmetry relations, that had initially been used to construct the global phase diagram of the quantum Hall effect [27] are commonly labeled as the law of corresponding states. It was later noted by Lütken et al. [28], that the validity of the law of corresponding states can be exploited to predict the behavior of the transport coefficients of a quantum Hall system, which have to be invariant under symmetry transformations that are derived from the law of corresponding states. In detail these

symmetry relations are:

1. Landau level addition: $\nu \leftrightarrow \nu + 1$

$$\sigma_{xy}(\nu+1) \longleftrightarrow \sigma_{xy}(\nu) + 1, \qquad \sigma_{xx}(\nu+1) \longleftrightarrow \sigma_{xx}(\nu) \tag{3.6}$$

(ν is the filling factor given by nh/eB, conductivities are given in units of e^2/h). This symmetry relation expresses the fact that the transition between Landau different quantum Hall plateaus (including the transition between the plateau at $\nu = 1$ and the high field insulator state at $\nu = 0$) is independent of the actual index of the quantum Hall state. Microscopically, completely filled Landau levels below the Fermi energy can be considered as an inert background. Experimentally this statement is supported by the observation of a critical exponent χ of the correlation length of the plateau-plateau transition (the localization length ξ) that is the same for all quantum Hall states [29].

2. flux attachment: $\frac{1}{\nu} \leftrightarrow \frac{1}{\nu} + 2$

$$\rho_{xy}\left(\frac{\nu}{2\nu+1}\right) \longleftrightarrow \rho_{xy}(\nu) + 2, \qquad \rho_{xx}\left(\frac{\nu}{2\nu+1}\right) \longleftrightarrow \rho_{xx}(\nu) \tag{3.7}$$

(resistivities are in units of h/e^2). This symmetry relation can be considered as transforming electrons to composite fermions (by attaching two flux quanta to each electron) and therefore to map the integer onto the fractional quantum Hall effect. The validity of this relation is supported experimentally by the observation of identical critical exponents for transitions between two integer and two fractional quantum Hall states.

3. particle hole symmetry: $\nu \leftrightarrow 1 - \nu$

$$\sigma_{xy}(1-\nu) \longleftrightarrow 1 - \sigma_{xy}(\nu), \qquad \sigma_{xx}(1-\nu) \longleftrightarrow \sigma_{xx}(\nu) \tag{3.8}$$

Expresses the fact that the physics of the system doesn't change if electrons are replaced by holes and vice versa.

These three relations can be satisfied by postulating that the conductivities σ_{xx} and σ_{xy}, written as a complex conductivity $\sigma = \sigma_{xy} + i\sigma_{xx}$ are invariant under the action of the symmetry group $\Gamma_0(2)$, which is a subgroup of the full modular group [28]. The elements of this symmetry group can be represented by a 2x2 matrix

$$\gamma \in \Gamma_0(2) : \gamma = \begin{pmatrix} a & b \\ 2c & d \end{pmatrix} \tag{3.9}$$

with a,b,c and d integer and $ad - 2bc = 1$. The flow of the conductivities for increasing L (decreasing T) has to follow flow lines that are also invariant under the action of the group $\Gamma_0(2)$. This requirement is fulfilled by the following function [30]:

$$f(\sigma) = -\frac{{\vartheta_3}^4(q){\vartheta_4}^4(q)}{{\vartheta_2}^8(q)}, \qquad q = e^{i\pi\sigma} \tag{3.10}$$

ϑ_2,ϑ_3 and ϑ_4 are the Jacobi theta functions, given by

$$\vartheta_2(q) = 2\sum_{n=0}^{\infty} q^{(n+\frac{1}{2})^2}, \quad \vartheta_3(q) = \sum_{n=-\infty}^{\infty} q^{n^2}, \quad \vartheta_4(q) = \sum_{n=-\infty}^{\infty} (-1)^n q^{n^2} \tag{3.11}$$

The flow of one fixed starting point then takes place along a trajectory that corresponds to a fixed argument of $f(\sigma)$:

$$\arg f(\sigma) = \alpha \tag{3.12}$$

Valid flow lines for the flow diagram introduced above can therefore be calculated by solving the above implicit equation. The parameter α corresponds approximately to σ_{xy}^{∞}, the Hall conductivity for $\sigma_{xx} \gg 1$:

$$\alpha \approx 2\pi(\sigma_{xy}^{\infty} - \frac{1}{2}) \tag{3.13}$$

A flow diagram calculated according to the described procedure is shown in figure 3.3. One remarkable feature of figure 3.3 is the semicircle with radius 0.5 around (0.5,0). This semicircle, which corresponds to the case $\alpha = 0$, gives the limiting behavior of σ at the plateau-plateau transition for $T \to 0$. It had previously been deduced from a microscopic model [31] and has been verified experimentally [32].
It has to be noted that although the theoretical approach using the law of corresponding states is able to give the correct flow lines for Khmelnitzkii's flow diagram, additional assumptions have to be made to fully determine the beta function of the problem [33]. There exist several Ansätze in the literature [33, 30, 34] without a general consensus.

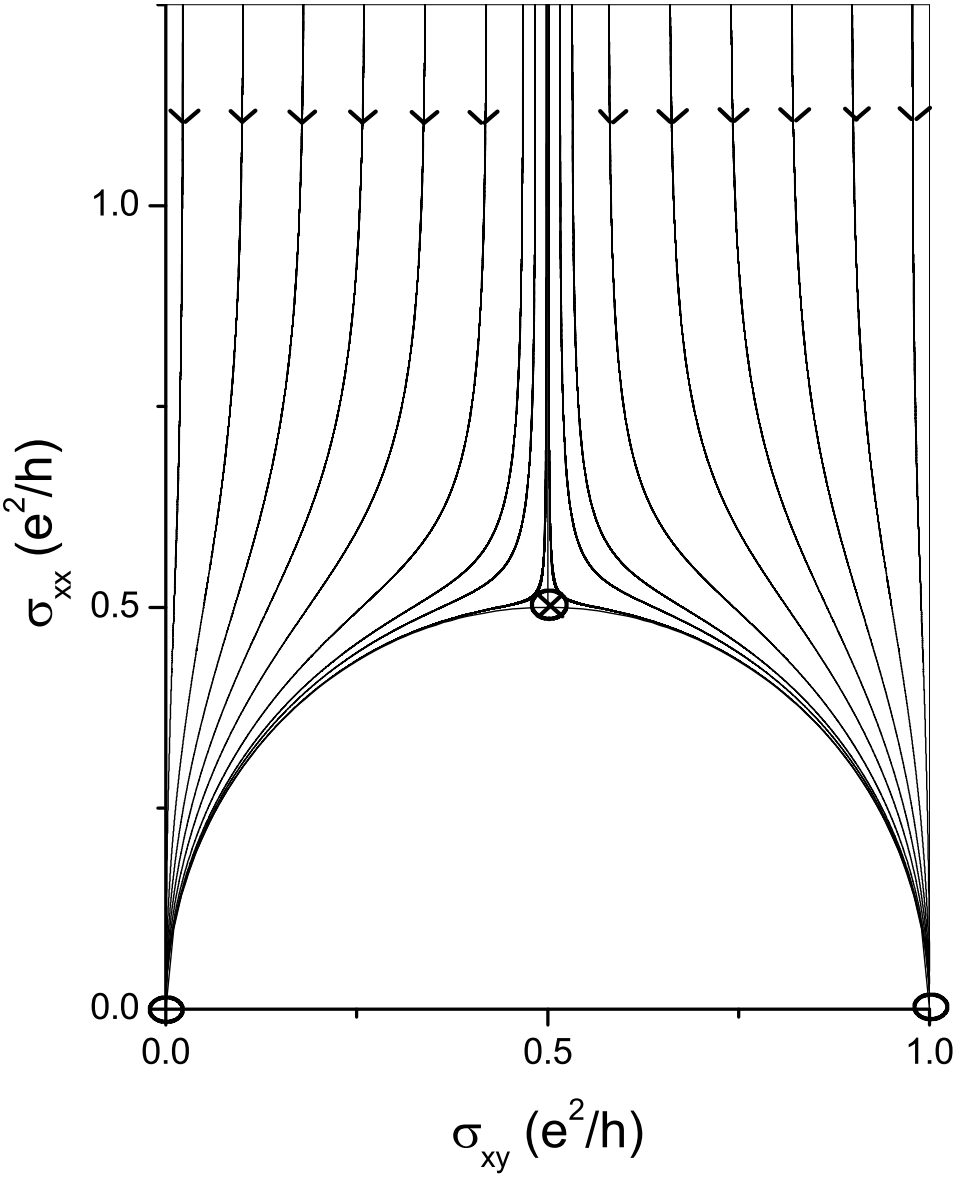

Figure 3.3: Flow diagram according to the theory of B. Dolan [30]. Two stable fixed points, corresponding to two neighboring Hall plateau states, are at (0,0) and (1,0), with an unstable fixed point (corresponding to the transition regime) at (0.5,0.5). The three fixed points are connected by a semicircle.

3.3 Quantum corrections in disordered conductors

A fully quantummechanical calculation of the transport coefficients reveals some deviations from the classical and quasi classical results given in chapter 2. As shown e. g. by Anderson [22], there are a variety of corrections to the Drude conductivities which arise from scattering in different orders and the interference of the wave functions of scattered electrons. These corrections depend essentially on the phase coherence of the electron wave functions, and therefore occur usually at very low temperatures. It turns out, that some corrections can easily be distinguished from each other by their characteristic dependence on magnetic field, as it is the case e. g. for weak localization corrections to be described in chapter 3.3.1

3.3.1 Weak localization

First calculated by P. W. Anderson [22] within the Kubo formalism (performing a sum up to second order over maximally crossed diagrams, the so called Langer-Neal graphs), a more intuitive derivation of the essential results of Anderson was given later by G. Bergman [35]. Considering an electron suffering multiple elastic scattering events so that its trajectory becomes self-intersecting as indicated in figure 3.4. Quantum mechanically, one cannot distinguish, if the loop in the trajectory is being traveled clockwise or anti-clockwise. One has to assume that there are two wave function, representing electrons which travel in opposite sense. Calculating the probability of finding an electron in the point of intersection B, one gets

$$|A + A'|^2 = A^2 + AA' + A'A + A'^2 = 4A^2 \tag{3.14}$$

(assuming $|A|^2 = |A'|^2$) which is twice the value expected from a classical calculation. In a quantum mechanical treatment the probability of finding an electron at the point of intersection is enhanced, and therefore the probability for the electron to penetrate the sample is reduced, resulting in an increase of resistance. This effect is however destroyed by a magnetic field, as the two electron trajectories acquire different phase differences depending on their sense of rotation. The increase of resistance is strongly suppressed for nonzero

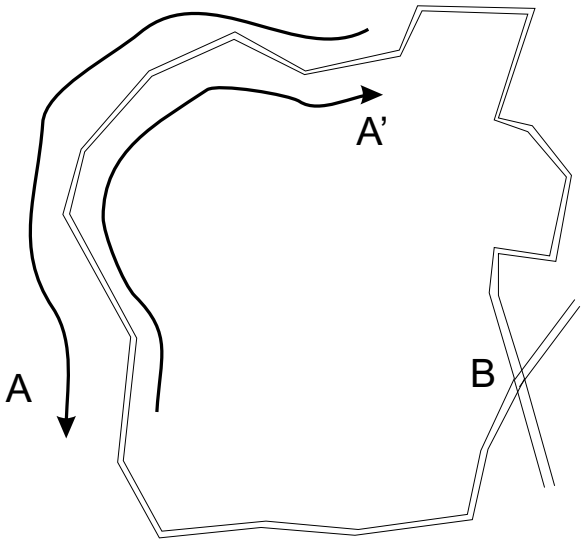

Figure 3.4: self-intersecting trajectory leading to weak localization corrections

magnetic field [35]:

$$\begin{aligned}\Delta\sigma_{xx}(B) &= -\frac{e^2}{2\pi^2\hbar}\left[\Psi\left(\frac{1}{2}+\frac{\hbar}{4eDB\tau}\right)-\Psi\left(\frac{1}{2}+\frac{\hbar}{4eDB\tau_{in}}\right)\right] \\ &= -\frac{e^2}{2\pi^2\hbar}\left[\Psi\left(\frac{1}{2}+\frac{B_0}{B}\right)-\Psi\left(\frac{1}{2}+\frac{B_{in}}{B}\right)\right]\end{aligned} \tag{3.15}$$

Ψ is the digamma function, τ is the elastic and τ_{in} the inelastic scattering time of the conduction electrons, and $D = v_F^2\tau/3$ is the diffusion constant . B_0 and B_{in} give the values of magnetic field where exactly one flux quantum passes through the area which is accessible to a conduction electron by diffusive motion in time τ or τ_{in}, respectively ($B_0 = \hbar/(4eD\tau)$, $B_{in} = \hbar/(4eD\tau_{in})$). In a measurement of $\sigma_{xx}(B)$ a dip at $B = 0$ results, with a width of about $2 \times B_{in}$. A measurement of $\sigma_{xx}(B)$ therefore allows a determination of the inelastic scattering time τ_{in} and the inelastic length $L_{in} = \sqrt{D\tau_{in}}$.
The temperature dependence of the weak localization corrections can be calculated using the results of the one parameter scaling theory of localization. It can be shown, that for $g \gg 1$, the beta function for two dimensions can be expressed as [22]

$$\beta(g) = -\frac{a}{g} + \mathcal{O}(\frac{1}{g^2}) \tag{3.16}$$

This means that σ_{xx} will show a logarithmic temperature dependence

$$\sigma_{xx}(T) = \sigma_{xx}^0 - k \cdot \ln(T) \tag{3.17}$$

(a and k are constants). Note that this result can be confirmed by a direct calculation of the temperature dependence of τ_{in} [35]. As it was shown in [36], weak localization has no effect on the Hall resisitvity.

3.3.2 Second order and interaction corrections

The weak localization corrections introduced in section 3.3.1 exist only if time reversal symmetry is preserved. If this is not the case, as e. g. in the presence of a magnetic field, they are suppressed and only corrections of higher order survive. These higher order corrections are much smaller and show no pronounced dependence on magnetic field.
The theoretical framework for calculating higher order localization corrections is the nonlinear sigma model, which is used to calculate the beta function of the problem. To be noted that in this case it is assumed that the only effect of magnetic field is the suppression of time reversal symmetry. With the results of [37] we get $\beta(g) = -1/g^2$, again for a two-dimensional system, and the following expression for the corrections to conductivity [38]:

$$\sigma_{xx} = \sigma_{xx}^0 - \frac{2}{\pi^2} \cdot \frac{e^4}{\hbar^2 \sigma_{xx}^0} \cdot \ln \frac{L}{L_0} = \sigma_{xx}^0 - \frac{p}{\pi^2} \cdot \frac{e^4}{\hbar^2 \sigma_{xx}^0} \cdot \ln \frac{T_0}{T} \tag{3.18}$$

L corresponds to the effective system size $L_{in} = \sqrt{D\tau_{in}} (\tau_{in} \propto T^{-p})$, L_0 is the distance an electron diffuses in the layer during its time of diffusion across the layer, and T_0 is defined from the equation $d \approx \sqrt{2D_{zz}^0 \tau_{in}(T_0)}$ (d being the thickness of the system in this case). Again, the corrections are logarithmic in T. As the prefactor of the correction term contains the high temperature conductance σ_{xx}^0 (which is a measure for the disorder of a sample) in the denominator, the corrections are small in clean samples, and become important only in strongly disordered systems.
As it was shown by Aronov and Altshuler in 1979 [39], in disordered conductors (more specific: disordered metals and heavily doped semiconductors) quantum corrections due to the electron-electron interaction can become large and comparable to the previously mentioned single particle localization corrections, which are solely due to impurity scattering. A somewhat handwaving but nevertheless convincing picture for this fact is that two electrons moving diffusively in a disordered conductor have a much higher probability to come close and to interact with each other than two electrons moving ballistically in a clean conductor. Quantitatively, also interaction corrections have a logarithmic temperature dependence in two dimensions, mainly due

to contributions from interactions in the diffusion channel [40]:

$$\sigma_{xx} = \sigma_{xx}^0 - \frac{2\lambda e^2}{\pi h} \ln \frac{L}{L_0} = \sigma_{xx}^0 - \frac{\lambda e^2}{\pi h} \ln \frac{T_0}{T} \tag{3.19}$$

In the case of interaction corrections L is given by $L_T = \sqrt{D\hbar/k_B T}$, and $T_0 \approx \hbar D_{zz}^0/k_B d^2$. λ is a material parameter ≤ 1.
In contrast to weak localization corrections there is no pronounced dependence on magnetic field expected for second order and interaction corrections, so we can expect the corrections to persist up to moderate magnetic fields. Note however that (3.18) and (3.19) have been derived assuming $\omega_c \tau \ll 1$.
According to [36], interactions should leave the Hall conductivity σ_{xy} unchanged.

3.4 Conduction by hopping

Even systems with localized states, whose conductivity tends to zero for decreasing temperature show a nonvanishing value of σ for finite temperature due to hopping of electrons between localized states. Although a lot of different mechanisms can be responsible for hopping events, the temperature dependence of the conductivity can be described by a common expression:

$$\sigma_{xx}(T) = \sigma_{xx}^0 \exp\left\{-\left(\frac{T_0}{T}\right)^p\right\} \tag{3.20}$$

with a prefactor σ_0 that can depend on T and a hopping exponent p which is characteristic for the microscopic mechanism responsible for the hopping events.
The most successful theories describing hopping conduction are based on the random resistor network model by Miller and Abrahams [41]. In this model hopping events between two localized sites i and j are associated with a resistance R_{ij}. The basic idea is that while without an electric field the same number of electron will hop from i to j as from j to i, in the presence of a difference in the electrostatic potential between sites i and j the two numbers will be different, a fact which can be seen as a current flow J_{ij}. Associating this effective current with the potential difference U_{ij} between sites i and j allows to define the resistance R_{ij}, which is a measure for the probability of hopping events between the two sites. As shown e. g. in [42], under the assumption of phonon assisted hopping, R_{ij} is equal to

$$R_{ij} = R_{ij}^0 \exp\left(\frac{2r_{ij}}{a} + \frac{E_{ij}}{k_B T}\right). \tag{3.21}$$

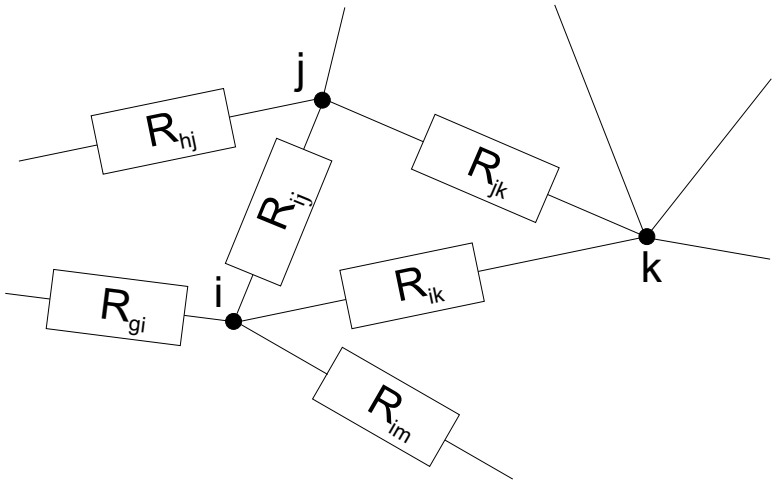

Figure 3.5: Random resistor network according to Miller and Abrahams

Here a is the effective Bohr radius of the electronic states, r_{ij} stands for the distance between site i and j and E_{ij} gives the energy difference between them. Obviously there are two contributions to R_{ij}, due to the spatial separation and the difference in energy between the two sites. The problem of finding the conductivity for a system of localized states at finite temperature is therefore reduced to the calculation of the conductivity of a random resistor network.

3.4.1 Thermally activated hopping

In a system of localized electronic states with the average thermal energy $k_B T$ still being large enough to cause transitions between neighboring sites, the conductivity follows equation (3.20) with an exponent $p = 1$ and a hopping temperature $T_0 = E_0/k_B$ which is roughly one order of magnitude smaller than the ionization energy of a shallow donor. This makes this regime clearly distinct from the regime of activated transport, where charge carriers are thermally activated into extended states in the conduction band and T_0 corresponds approximately to the ionization energy of a shallow donor. Activated transport therefore occurs at a temperature which is one order of magnitude higher. Hopping events in this temperature range essentially take place between neighboring localized states, which has lead to the term of *nearest neighbor hopping* for this transport regime. For the details of the calculation of T_0, which is not straightforward and depends strongly on the material parameters of the semiconductor (carrier concentration, degree of compensation) we refer to [42], chapter 8.

3.4.2 Variable range hopping

At even lower temperatures, when the average thermal energy is not sufficient anymore to cause hopping events, a different mechanism becomes important, which favors hopping events between sites which may be at a larger distance, but are closer in energy. This can easily be demonstrated by the previously introduced random resistor network model. Considering the argument of the exponential in (3.21) it is clear, that only sites with a small E_{ij} will take part in hopping conduction at very low temperature. The states involved in the conduction process can be assumed to lie in a small energy band $E_F - E_0 < E < E_F + E_0$ of width $2E_0$ around the Fermi level E_F. For low enough temperature the density of states $n(E)$ can be assumed to be constant in this small range of energy ($n(E) = n(E_F)$). Then the number of states N in this energy band equals

$$N(E_0) = 2n(E_F)E_0. \tag{3.22}$$

Setting r_{ij} in (3.21) to $[N(E_0)]^{-\frac{1}{d}}$ (d being the dimensionality of the system) and replacing E_{ij} by E_0, equation (3.21) gives for the corresponding resistance:

$$\begin{aligned} R_{ij} &= R_{ij}^0 \exp\left(\frac{2}{[N(E_0)]^{\frac{1}{d}}\, a} + \frac{E_0}{k_B T}\right) \\ &= R_{ij}^0 \exp\left(\frac{1}{[2n(E_F)E_0]^{\frac{1}{d}}\, a} + \frac{E_0}{k_B T}\right) \end{aligned} \tag{3.23}$$

The argument of the exponential contains two contributions, the first dominating for small values of E_0, the second for large values of E_0. R_{ij} has a minimum at an intermediate value of

$$E_{0,min} = \left\{\frac{2k_B T}{da\,[2n(E_F)]^{\frac{1}{d}}}\right\}^{\frac{d}{d+1}} \tag{3.24}$$

It is clear that the resistivity of a sample will mainly be determined by hopping events which take place in a range of $E_0 \approx E_{0,min}$, therefore this energy range is also being labeled the *optimal band*. Substituting (3.24) into (3.23) and associating $R_{ij}(E_{0,min})$ with the total resistivity of the system, one arrives at Mott's law for variable range hopping (VRH):

$$\rho_{xx} = \rho_{xx}^0 \exp\left\{\left(\frac{T_0}{T}\right)^{\frac{1}{d+1}}\right\} \tag{3.25}$$

Although the temperature dependence of ρ is correctly reflected by this rather simple optimal band approach, the constant T_0 has to be calculated with the help of percolation theory (see e. g. [42], chapter 5). The result is :

$$T_0 = \frac{\beta(d)}{k_B n(E_F) a^d} \tag{3.26}$$

The average distance $\bar{r}$ of two states belonging to the optimal band corresponds to the average hopping length. Using (3.22) and (3.24) we get

$$\bar{r} = r_{ij}(E_{0,min}) = \left[\frac{1}{4} \cdot \frac{ad}{n(E_F)} \cdot \frac{1}{k_B T}\right]^{\frac{1}{d+1}} \approx a \left(\frac{T_0}{T}\right)^{\frac{1}{d+1}} \tag{3.27}$$

3.4.3 Hopping in a Coulomb gap

An extension of Mott's equation for hopping conduction became necessary as several experiments were in disagreement with the exponents $p = 1/(d+1)$ predicted by variable range hopping. As shown by Efros and Shklovskii [43], it is necessary to include Coulomb interaction between hopping electrons. As in contrast to a metallic system with extended states no screening of the electron Coulomb potential will happen in a system of localized states, it seems obvious that Coulomb interactions can significantly change the behavior of the system. A simple calculation showing the effect of Coulomb interaction following [42] will be given below.
Main difference to a non-interacting system is that for the transfer of an electron from an occupied state $E_i < E_F$ to an unoccupied state $E_j > E_F$ an energy equal to

$$\Delta E = E_j - E_i - \frac{e^2}{\epsilon r_{ij}} \tag{3.28}$$

is necessary (ϵ is the dielectric constant). ΔE is equal to the difference between the energies of state i and j plus the electrostatic energy of the electron-hole pair, that has been created by the hopping process (a different interpretation is the existence of a Coulomb blockade between two localized states). Replacing r_{ij} by $[N(E_0)]^{-\frac{1}{d}}$, we get for the density of states $n(E) = dN/dE$

$$n(E_j - E_i) = n(E) \leq d \left(\frac{\epsilon}{e^2}\right)^d |E|^{d-1} . \tag{3.29}$$

The density of states shows the so called *Coulomb gap* with a value of 0 at the Fermi energy and a linear increase in its vicinity for $d = 2$ as illustrated

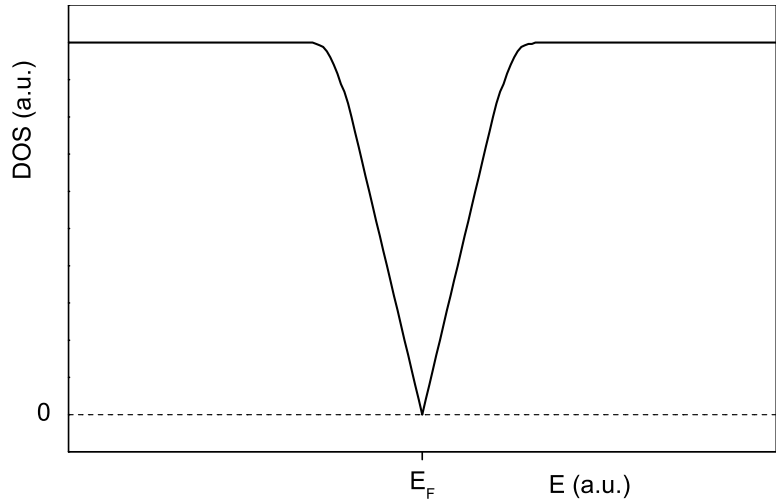

Figure 3.6: Coulomb gap around the Fermi energy in two dimensions.

in figure 3.6.
Using this modified density of states to calculate $N(E_0)$ as in chapter 3.4.2 we get

$$N(E_0) = \int_{E_F-E_0}^{E_F+E_0} d\left(\frac{\epsilon}{e^2}\right)^d |E|^{d-1}\, dE \propto \int_{E_F}^{E_F+E_0} E^{d-1} dE \propto {E_0}^d. \tag{3.30}$$

Repeating the calculation of chapter 3.4.2, the dimensionality of the system drops out, and we get a d-independent result

$$\rho_{xx} = \rho_{xx}^0 \exp\left\{\left(\frac{T_1}{T}\right)^{\frac{1}{2}}\right\} \tag{3.31}$$

with a hopping exponent $p = 1/2$. As in the case of variable range hopping, this simple optimal band approach cannot give the correct values for T_1, which have to be determined by more sophisticated theories [44]:

$$T_1 = C\frac{e^2}{k_B \epsilon a} \quad (d = 2) \tag{3.32}$$

As it was shown both experimentally [45] and theoretically [46] an exponent $p = 1/2$ is also observed in hopping transport occurring in the minima of the conductivity of the quantum Hall effect:

$$\sigma_{xx} = \sigma_{xx}^0(T) \exp\left\{-\left(\frac{T_1}{T}\right)^{\frac{1}{2}}\right\} \tag{3.33}$$

In this case the effective Bohr radius a in (3.32) has to be replaced by the localization length ξ, and the prefactor σ_0 in (3.33) depends on temperature ($\sigma_0 \propto T^{-1}$). It should be noted that due to the tensor nature of σ and ρ in strong magnetic fields we get for ρ_{xx}:

$$\rho_{xx} = \frac{\sigma_{xx}}{\sigma_{xx}^2 + \sigma_{xy}^2} \approx \frac{\sigma_{xx}}{\sigma_{xy}^2} \propto \sigma_{xx} \tag{3.34}$$

This is correct in a quantum Hall plateau as σ_{xy} is quantized (constant) and σ_{xx}, according to (3.33) is exponentially small. Therefore, in contrast to the zero field case (3.31), ρ_{xx} is decreasing with temperature and, somewhat counterintuitively, ρ_{xx} and σ_{xx} are proportional to each other.

3.4.4 The Murzin model

One drawback of the theory for variable range hopping and its modification by the inclusion of Coulomb interaction is that it cannot account for experiments giving hopping exponents $p > 0.5$, that have been reported in the past (e. g. in [47, 48, 49]). As these experiments cover several orders of magnitude in σ and T, they cannot be interpreted in terms of a crossover effect between thermally activated and variable range hopping. As shown by Murzin [38], hopping exponents $p > 0.5$ can be explained taking into account a dependence of the localization length ξ on the energy $\Delta E = |E - E_c|$ with respect to the center of the Coulomb gap. Such a dependence is suggested by recent numerical work for lattice models of interacting electrons [50]. As interaction, which is stronger inside the Coulomb gap compared to regions outside the gap, should lead to reduction of the localization length compared to the noninteracting case, one can assume ξ to depend on energy as follows:

$$\xi = \alpha \, |\Delta E|^s \tag{3.35}$$

Repeating the derivation of (3.31) with this additional dependence (taking into account that ξ replaces a in (3.21)) we arrive at

$$\rho_{xx} \propto \sigma_{xx} \propto \exp\left\{ -\left(\frac{T_1}{T}\right)^{\frac{s+1}{s+2}} \right\} \tag{3.36}$$

with

$$T_1 = \frac{S}{k_B} \left(\frac{Ce^2}{\alpha\epsilon}\right)^{\frac{1}{s+1}}, S = \left[(s+1)^{-\frac{s+1}{s+2}} + (s+1)^{\frac{1}{s+2}} \right]^{\frac{s+2}{s+1}} \tag{3.37}$$

For $s = 0$ (3.31) is recovered, and for $s \gg 1$ activated behavior results.

Chapter 4

Experimentals

This chapter is devoted to the actual experimental realization of a quantum Hall effect experiment. We will describe the magnets of the Grenoble High Magnetic Field laboratory that were used to create high magnetic fields, we will show the cryogenic setups to produce the low temperatures essential for our experiments, and give some details of the actual measurement of the sample resistivities. Our way of realizing a two-dimensional electron system is new - it will be described in detail in the remainder of this chapter.

4.1 Generation of high magnetic fields

Except for measurements below $B = 10$ T, where superconducting solenoids were used, the magnetic field for the experiments was created by the resistive magnets of the GHMFL (sites M3, M6, M7, M9 and M10). As superconducting magnets based on Ni_3Sn are limited with respect to their maximum field (≈ 21 T in a 50 mm warm bore in 2004), fields in excess of 20 tesla have to be produced by resistive magnets or by hybrid magnets that incorporate a superconducting and a resistive part. With resistive magnets, maximum fields of 31 tesla have been reached in a 50 mm warm bore at the Grenoble High Magnetic Field Laboratory; a hybrid magnet that should allow to attain magnetic fields in excess of 40 T is currently under construction and should be operational in the second term of 2004.
The resistive magnets are sophisticated copper coils, that use two design principles. The outer part of the magnet is usually a so called Bitter magnet, realizing a coil by a stack of copper disks. The inner part usually is a polyhelix magnet, that consists of concentric copper tubes that have been cut into helices. As the development and the maintenance of resistive magnets requires a considerable know-how and as their operation needs a large electri-

cal installation (typical power consumption at 30 tesla is around 20 MW DC), resistive magnets are operated only at a few specialized laboratories in the world, like the National High Magnetic Field Laboratory (NHMFL) in Tallahassee (Florida, USA), the High Field Magnet Laboratory at the university of Nijmegen (Netherlands), the High Field Laboratory for Superconducting Materials (HFLSM) in Sendai (Japan), or the Grenoble High Magnetic Field Laboratory (GHMFL).
The magnetic field produced by the resistive magnets of the GHMFL has a spatial homogeneity of the order of 10^{-3} (exact values can be found in [51]) in a sphere of 1 cm in diameter around the field center, and a temporal stability of about 10^{-4}, the latter one basically being caused by parasitic AC-signals at the main power frequency and its higher harmonics. Although the spatial and temporal stability of these magnets, which have been optimized with respect to their maximum field, can be a major problem for some experiments (e. g. magnetic resonance), they are sufficient for our purposes. All superconducting magnets used in this work had temporal and spatial stability parameters at least one order of magnitude better than the resistive magnets.

4.2 Cryotechnics

As will be shown in the following chapter, the quantum Hall effect observed in our samples becomes visible at rather low temperatures below 1 K and, in some cases, develops fully only below 100 mK. For our experiments we therefore needed the lowest possible temperatures available. The technique of choice for creating very low temperatures in high magnetic fields is dilution refrigeration, a method which cools by diffusion of ^{3}He atoms from a ^{3}He-rich phase into a ^{4}He-rich phase in the 2-phase region of the phase diagram for ^{3}He -^{4}He mixtures below 867 mK. With this continuous method of refrigeration we were able to maintain a temperature of $T \leq 50$ mK at magnetic fields up to 28 tesla. For the physical and technical details of dilution refrigerators we refer to [52].
In the experiments described in this thesis we have used two different ^{3}He/^{4}He dilution refrigerators. The angle dependent measurements were done in a commercial, top loading dilution fridge (Oxford Instruments Kelvinox series) equipped with a sample holder that permitted to rotate the sample in situ. For most of the other experiments a small dip-stick dilution fridge with a plastic mixing chamber was used. Due to its non-metallic mixing chamber, this fridge had an almost negligible susceptibility to eddy current heating during a magnetic field sweep. (the commercial Kelvinox dilution refrigerator,

due to its metallic mixing chamber, allowed for sweep rates of the magnetic field not faster than 50 Gauss/second at temperatures below 50 mK due to this problem). The cooling power of the two systems at $T = 100$ mK were 20 μW for the dipstick, and 900 μW for the Kelvinox system, respectively. In all experiments the samples, mounted on industrial chip-carriers made of Al_2O_3 ceramics, were placed inside the mixing chamber and immersed into the diluted (^{4}He-rich) phase. Temperature was measured with Ruthenium oxide thick film chip resistors, that had been calibrated versus a Ge-standard resistor (Lakeshore). As a precise determination of the magnetoresistance error of the Ruthenium oxide thermometers had not been possible over the whole range of temperature covered by our experiments, measurements performed as a function of temperature were limited to a field range where the error in temperature due to thermometer magnetoresistance is smaller than 1% (see also chapter A.1).

4.3 Measurement of the magnetoconductance

For the measurement of the transport parameters, the two-dimensional electron system, to be presented in detail in the following chapter, was processed by optical lithography into a so called Hall bar shape, that permits to measure V_{xx} and V_{xy} independently. Usually two Hall bars, of 200 μm in width and 1400 μm in length were etched on a small piece of wafer. Contacts to the 2DEG were prepared by diffusion of a Cr-Au-Ge alloy into the conducting semiconductor layer and the evaporation of a Au-Cr layer onto the diffused contacts, to facilitate the attachment of bonding wires. The sample was then glued into a chip-carrier and contacted with 16 μm Au-wire bonds. Inside the cryostat the chip-carrier was connected with 100 μm twisted pair manganin wires. Resistances of the cable connections were around 100 Ω typically. V_{xx} and V_{xy} were measured with a standard AC lock-in technique at very low frequencies of 0.5 or 3 Hz. During an experiment we passed a constant current of typically 1 nA through the sample and recorded V_{xx} and V_{xy} as a function of B or T respectively. If necessary, the current was adjusted to avoid self-heating of the sample and to stay in a regime of linear resistance ($dV/dI =$ const.). The lock-in phase was adjusted to zero in a field range where V_{xx} is small. In high magnetic fields, when the samples show a strong increase of the longitudinal resistance, the lock-in phase usually increased to $\pi/2$ rather quickly, showing that the sample or the contacts became insulating. In this case, the data were cut before the onset of the phase shift.

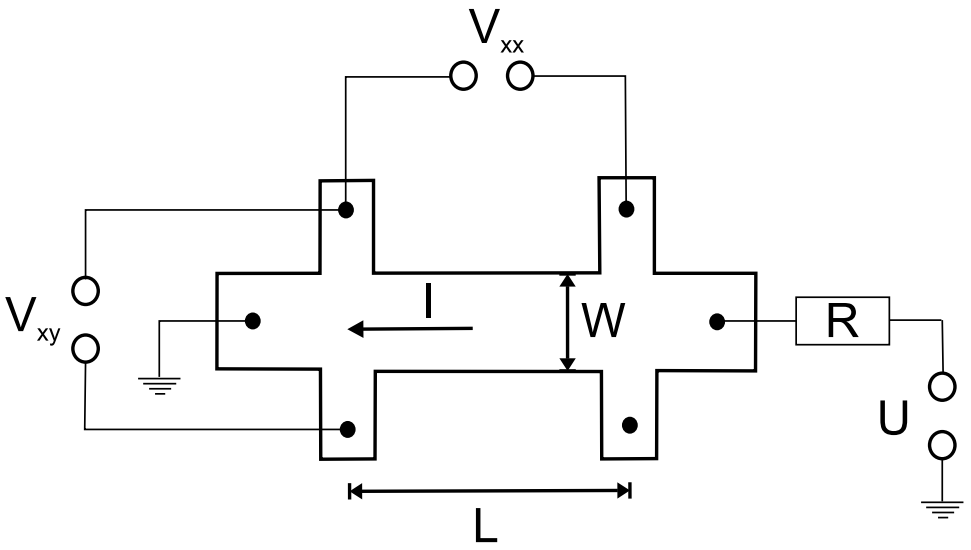

Figure 4.1: Setup for magnetoconductance measurement

From V_{xx}, V_{xy} and I we can the calculate the sample resistances

$$R_{xx} = \frac{V_{xx}}{I} \qquad R_{xy} = \frac{V_{xy}}{I}. \tag{4.1}$$

The resistances, relating the voltage drop between two contacts directly to the current are sample-dependent quantities. A sample made of the same material but of different shape will usually not show the same resistances. It is therefore preferable to express the results as resistivities, that are material parameters, relating the current density to the electric field inside a sample. They do not depend on the macroscopic shape of the sample. In two dimensions the longitudinal (ρ_{xx}) and Hall (ρ_{xy}) resistivity are calculated as follows:

$$\rho_{xx} = \frac{V_{xx}}{I} \cdot \frac{W}{L} \qquad \rho_{xy} = \frac{V_{xy}}{I}. \tag{4.2}$$

The above statements apply as well to the conductances (G_{xx}, G_{xy}), that relate current to the voltage drop between two contacts, and to the conductivities (σ_{xx}, σ_{xy}), relating electric field to current density. The conductivities can easily be calculated from the resistivities by tensor inversion.
The two-dimensional case is special, as resistances and resistivities, or conductances and conductivities have the same unit Ω or $1/\Omega$, respectively. Resistances and conductances are scale invariant, and in addition R_{xy} and ρ_{xy}, as well as G_{xy} and σ_{xy} are identical.

4.4 Samples – impurity confined quantum wells

In contrast to the general trend in experimental quantum Hall physics to low disorder, high mobility systems, the samples that have been investigated in this thesis are strongly disordered, low mobility systems. We have used the most simple way of confining free charge carriers to a layer, just by sandwiching a doped layer of semiconductor between undoped layers of the same material. This way, the electron gas is confined inside the doped layer by a space charge potential that is build up due to charge carriers diffusing from the doped into the undoped layers. We therefore call our systems *impurity confined quantum wells*, because confinement is not caused by a difference of the bandgap in neighboring semiconductor layers, as it is the case in classical AlGaAs/GaAs heterostructures. The same method of confinement is also used in delta-doped quantum wells and in nipi-structures. We note that impurity confined quantum wells have been described before by Maan et al. [53]. Using GaAs (n-type, Si-doped) as semiconductor material for our transport experiments, we have electrons with an isotropic effective mass m=0.067·m_e (m_e being the free electron mass). An anisotropy of the effective mass m, as found for example in Si, can render the magnetotransport data extremely complicated, as it introduces additional splittings of the Landau levels. Due to the small effective mass and a large dielectric constant (ϵ_r = 12.53) of GaAs, the excess electron of a Si-donor will occupy a hydrogen-like state with a large effective radius of $a = \hbar^2\epsilon/me^2 = 10$ nm. With a concentration of $n = 1.5 \cdot 10^{17}\mathrm{cm}^{-3}$ the wavefunctions of neighboring donor-electrons will overlap and form a so called impurity band, at an energy of some meV below the conduction band edge. The donor electrons move freely in this impurity band, and the semiconductor at this doping level shows a finite conductivity even in the limit of $T \to 0$, it behaves like a metal. A strong magnetic field will compress the hydogen-like wavefunctions of the donor electrons [54] and will therefore reduce the effective overlap between neighboring sites, finally leading to a breakdown of the impurity band and a transition to an insulating state in very high magnetic fields.

4.4.1 Conduction band profile

The samples were grown on an undoped (semi-insulating) GaAs wafer with a (100) surface. The exact sequence of the layers is shown in figure 4.2. For the formation of the free electron gas only the upper three layers are important; the sequence of GaAs/AlGaAs layers below are usually called a superlattice buffer. Its purpose is to provide a good, defect free surface for the growth of the layers that carry the free electron gas.

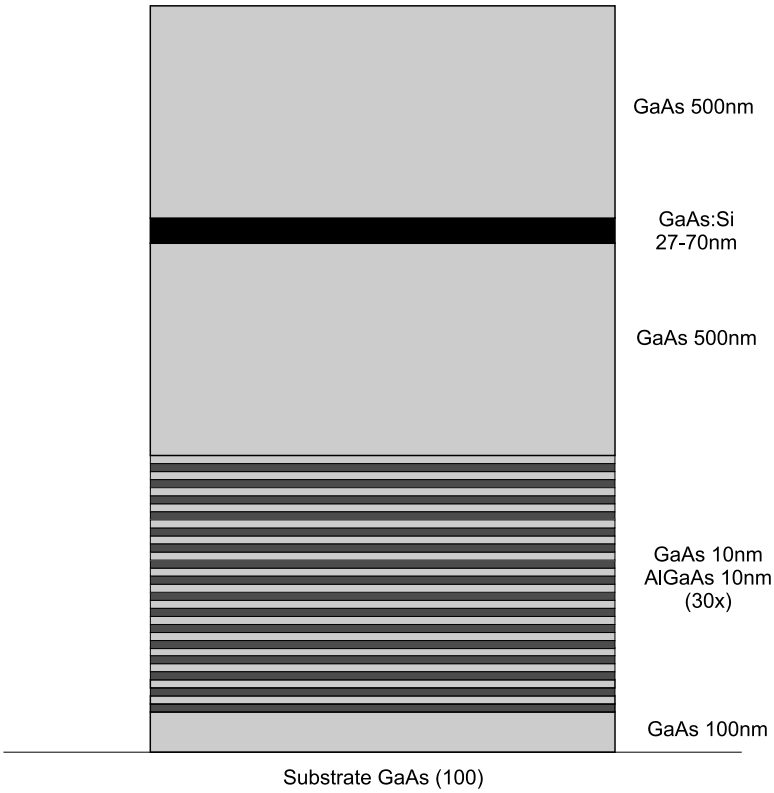

Figure 4.2: Layer sequence grown by molecular beam epitaxy (MBE)

In the following we will give a short calculation of the band profile at the junction between an undoped and a n-type (Si-doped) GaAs layer. This situation corresponds to a *one sided abrupt pn junction*, as it is shown e.g. in [55]. Note that nominally undoped GaAs grown by MBE turns out to be slightly p-type effectively ($n_p \approx 10^{14}\mathrm{cm}^{-3}$[56]). The nominal electron concentration in the doped layer n_n is equal to $1.5{\cdot}10^{17}\mathrm{cm}^{-3}$. Under thermal equilibrium, with no current flowing ($j_z = 0$) and no voltage applied across the layers (E_z=0, unbiased junction)

$$j_z = 0 = -e\mu(nE_z - \frac{kT}{e}\frac{\partial n}{\partial z}) = \mu n \frac{\partial E_F}{\partial z} \tag{4.3}$$

μ is the electron mobility. The steady state condition $j_z = 0$ requires the Fermi energy E_F to be constant across the different layers. As the Fermi energy in n-type GaAs lies in the impurity band of the Si-donors (close to the conduction band edge), and as in the nominally undoped, effectively slightly p-type layer E_F is close to the valence band, some charge transfer will happen creating a space charge layer at the boundaries, which will lead

to a bending of the band edges and therefore a matching of the Fermi energy in the two different layers. A sketch of the space charge layers and the conduction band edge is shown in figure 4.3. A certain amount of electrons

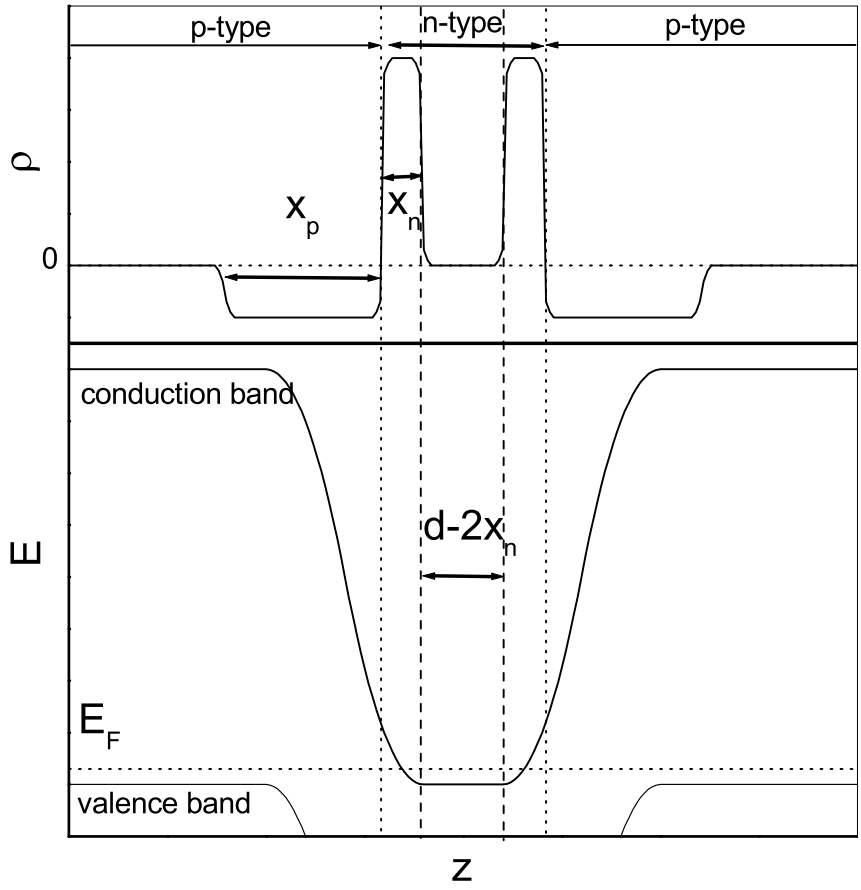

Figure 4.3: Conduction band profile and charge density ρ in the space charge layers for an impurity confined quantum well

will diffuse into the undoped layers, thereby creating the confining space charge layer. These electrons will be captured by acceptor impurities in the undoped layer and are therefore not available for current transport anymore. The effective electron concentration inside the quantum well will therefore be slightly smaller than the nominal density the n-layer has been grown with. And further, the effective thickness of the quantum well will be reduced by twice the thickness of the depletion layer x_n, that after [55] for a pn-junction

is equal to:

$$x_n = \sqrt{\frac{2\epsilon}{e} \cdot \frac{n_p}{n_n(n_n + n_p)} E_G} \tag{4.4}$$

ϵ is the dielectric constant ($12.53\epsilon_0$ for GaAs), n_n and n_p are the electron concentrations of the majority charge carriers in the n- or the p- layer, respectively, and E_G is band gap ($E_G = 1.52$ eV in GaAs). For our samples we get $x_n = 4.6$ nm.
In contrast to conventional 2DEG devices (Si inversion layers, AlGaAs/GaAs heterostructures) in the present system there is no way to change the carrier density. A widely used method to achieve this in AlGaAs/GaAs heterostructures is the illumination with infrared light from a light emitting diode, thereby exciting electrons that are trapped on DX-centers. This method however has been reported to have only a small effect in delta-doped GaAs [57] and has therefore not been applied to our samples.

4.4.2 Basic transport parameters

Basic parameters of a 2DEG that are of interest are the carrier mobility μ, the elastic mean free path l, and the (two-dimensional) carrier density n^{2D}. μ and l can be calculated from ρ_0, the value of ρ_{xx} at zero magnetic field[1], n^{2D} from the slope of ρ_{xy} at small magnetic fields using the Drude model (2.2). As in addition our samples show Shubnikov-de Haas oscillations in ρ_{xx} at relatively high temperatures, when the electronic transport is essentially three-dimensional, we can use this to determine the three-dimensional carrier density n^{3D} from the period of these oscillations using (3.1). The ratio n^{2D}/n^{3D} then corresponds to the effective layer thickness d_{eff} of the sample. Results for the samples investigated in this work are shown below; the values given in table 4.1 are reproducible between different cooldowns to better than 5%. Comparing the nominal thickness d to the effective thickness $d_{eff} = n^{2D}/n^{3D}$ we find that the average difference between them is $\overline{\Delta d} = 10$ nm (we have excluded sample 70 from the average, because it is of poorer quality due to non-optimal conditions during the MBE-growth). This is in agreement with twice the width of the depletion layer x_n calculated in chapter 4.4.1. We can also say that a sample-independent number

[1] Note that for the value of ρ_0 we took ρ_{xx} at small magnetic fields (where weak localization corrections were already suppressed) for the more metallic samples 70, 50, 40 and 37, or ρ_{xx} at the magnetic field value where the $\rho_{xx}(B)$-curves of different temperatures intersect (to avoid large contributions due to Anderson localization) for the more strongly localized samples 34, 30 and 27

sample	$\mu(cm^2/Vs)$	$l(nm)$	$n^{2D}(10^{11}cm^{-2})$	$n^{3D}(10^{17}cm^{-3})$	$d_{eff}(nm)$
70	1300	13	2.7	1.3	21
50	2400	27	5.0	1.7	29
40	2200	24	4.8	1.6	30
37	1600	17	4.8	1.6	30
34	1800	19	4.0	1.5	27
30	1700	17	2.9	1.3	22
27	1100	10	2.3	1.3	18

Table 4.1: Basic sample parameters. The samples are labelled according to their nominal layer thickness in nm.

of electrons $N = 1.5{\cdot}10^{11}\mathrm{cm}^{-2}$ is localized in the space charge layers and forms the confinement potential. The two-dimensional carrier densities n^{2D} are intermediate densities for quantum Hall samples and let a filling factor $\nu = 1$ be expected around $B = 10$ T. We can note that similar values for l and μ have been found in bulk samples with the same n^{3D} in [58]. Using the value $\Gamma = \hbar/\tau \approx 120$ K as a rough estimate for the static disorder broadening of the Landau levels, we can see that the static disorder broadening of the levels is almost as large as the Landau level spacing $\hbar\omega_c$ at $B = 10$ T, which is equal to 200 K. The Landau levels will therefore overlap strongly even in rather high magnetic fields of $B = 10$ T.

4.4.3 Dimensional subbands

Due to the confining potential of the quantum well, electron motion in z-direction is not free, and there is no continuous energy spectrum as for a free electron, but the energy spectrum of the motion in z-direction consists of discrete levels, called dimensional subbands. Treating the quantum well as an infinitely deep rectangular well of with d, the energy spectrum for the dimensional subbands corresponds to

$$E^{(n)} = \frac{\pi^2\hbar^2}{2m} \cdot \frac{n^2}{d^2},\ n = 1, 2, 3, \ldots \tag{4.5}$$

With a Fermi energy $E_F = 180$ K, for the first unoccupied dimensional subband, we get energies ranging from $E^{(2)} \approx 360$ K for sample 27 to $E^{(4)} \approx 210$ K for sample 70. This means that in our samples between one and three dimensional subbands are fully or partially occupied. Given the estimate for the static disorder broadening calculated in the previous chapter it is clear,

that the dimensional subbands overlap strongly and that their structure in the density of states is almost completely washed out into a continuum.

4.4.4 Dimensionality

Although observed in systems that effectively have a finite extension in the third dimension for practical reasons, the quantum Hall effect has always been understood as a two-dimensional phenomenon. As illustrated e.g. in [59], the fact that the value of $R_K = h/e^2$ could be confirmed to be universal up to 8 digits requires the relation

$$\rho_{xy} \equiv R_{xy} \tag{4.6}$$

to hold. R_{xy} is the physical quantity being measured in an experiment, whereas ρ_{xy} can be shown to be quantized from a theoretical point of view. For (4.6) to hold the system under consideration must be two-dimensional with respect to electronic transport, as in three dimensions (4.6) would include a sample dependent scaling factor (the sample thickness) that cannot be determined to one part in 10^8.
Naively, one would chose the elastic mean free path l as criterion for dimensionality. In this case, all our samples would have to be considered three-dimensional. Also the fact that in all of our samples two or more dimensional subband are at least partially occupied seems to indicate three-dimensionality. However, as shown in chapter 2, an essential precondition for the quantum Hall effect is the localization of charge carriers in the Landau level tails. The criterion for a state to be localized is that its localization length is smaller than the effective sample size, which is given by the inelastic scattering length ($\xi < L_{in}$). This indicates that for the occurrence of the quantum Hall effect the inelastic scattering length L_{in} is the relevant length scale.

Chapter 5

Results

After showing the basic experimental results for a quantum Hall system - magnetoresistivity and magnetoconductivity - we present the conductivity data in form a plot of σ_{xx} versus σ_{xy}, to test the agreement with the theoretical flow diagram introduced in chapter 3. Following that, we show a quantitative comparison of our data with microscopic theories for the temperature dependence of σ_{xx}. We further present a detailed investigation of the angle dependence of the quantum Hall effect in two of our samples at the end of this chapter.

5.1 Magnetotransport

The magnetotransport data of a sample – Hall and longitudinal resistivity measured as a function of magnetic field at fixed temperature – are the experimental results of primary interest for a quantum Hall system, as they usually show, with high precision (verified up to 1 part in 10^8) the well known plateaus in ρ_{xy} at simple fractions of the fundamental resistance unit h/e^2=25812.807 Ω. We will therefore give all resistivity and conductivity data in *quantum* units of h/e^2 or e^2/h, respectively. The basic sample parameter that we have varied throughout this work is the layer thickness d. Samples with d = 27, 30, 34, 37, 40, 50 and 70 nm have been grown by MBE and have been investigated at temperatures down to 40 mK in magnetic fields up to 23 tesla (previous work on samples with d = 100, 140 nm has been published in [60, 61, 62]). We will label the samples by their nominal layer thickness d in nm. Looking at their magnetoresistivity data and following a scheme put forward e. g. by Das Sarma in [63], one can classify them into two categories, depending on the temperature dependence of ρ_{xx} at small magnetic fields. Samples with $d \leq 30$ nm show an exponential increase of

ρ_{xx} with decreasing T and are therefore called *insulating*. Samples with $d \geq$ 34 nm show a more or less constant value of ρ_{xx} for decreasing T at small magnetic fields, with only a weak, logarithmic increase of ρ_{xx} due to weak localization in the vicinity of $B = 0$. We will call these samples *metallic*.[1]

5.1.1 Insulating samples

We present the field dependent resistivity for samples 27 and 30 in figures 5.1 and 5.2.

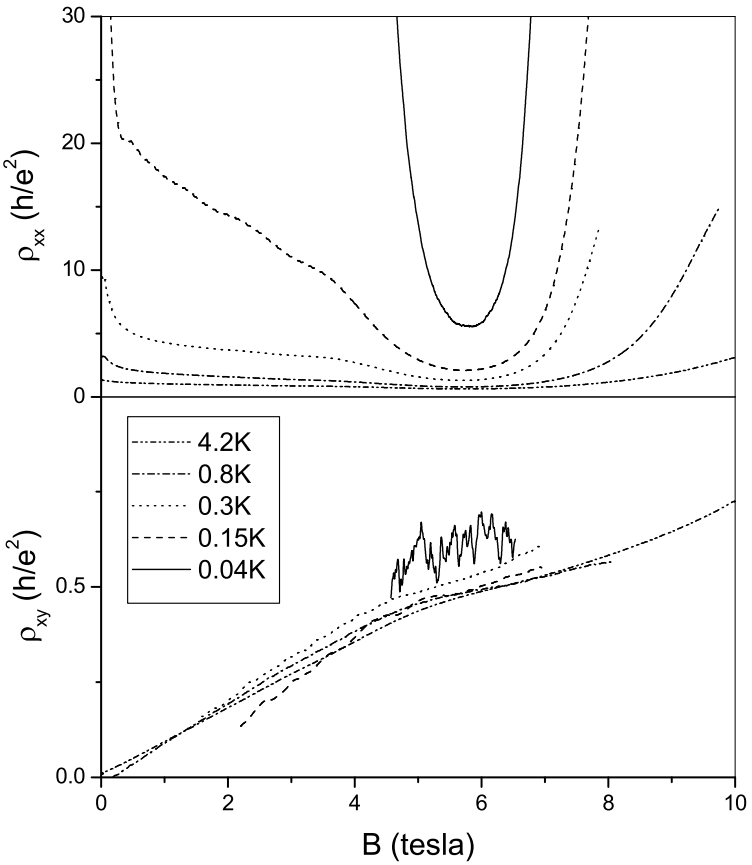

Figure 5.1: Magnetoresistivity data for sample 27. For the lowest temperatures ρ_{xy} is only shown around the minimum of ρ_{xx} as elsewhere, at fields where $\rho_{xx} \gg \rho_{xy}$ it cannot be measured without a large error due to mixing between ρ_{xx} and ρ_{xy}.

[1]The terms *insulating* and *metallic* here have a purely phenomenological definition: $\rho_{xx} \to \infty$ ($\sigma_{xx} \to 0$) for $T \to 0$ defines an *insulator*, $\rho_{xx} \to \rho_0$ ($\sigma_{xx} \to \sigma_0$) for $T \to 0$ defines a *metal*.

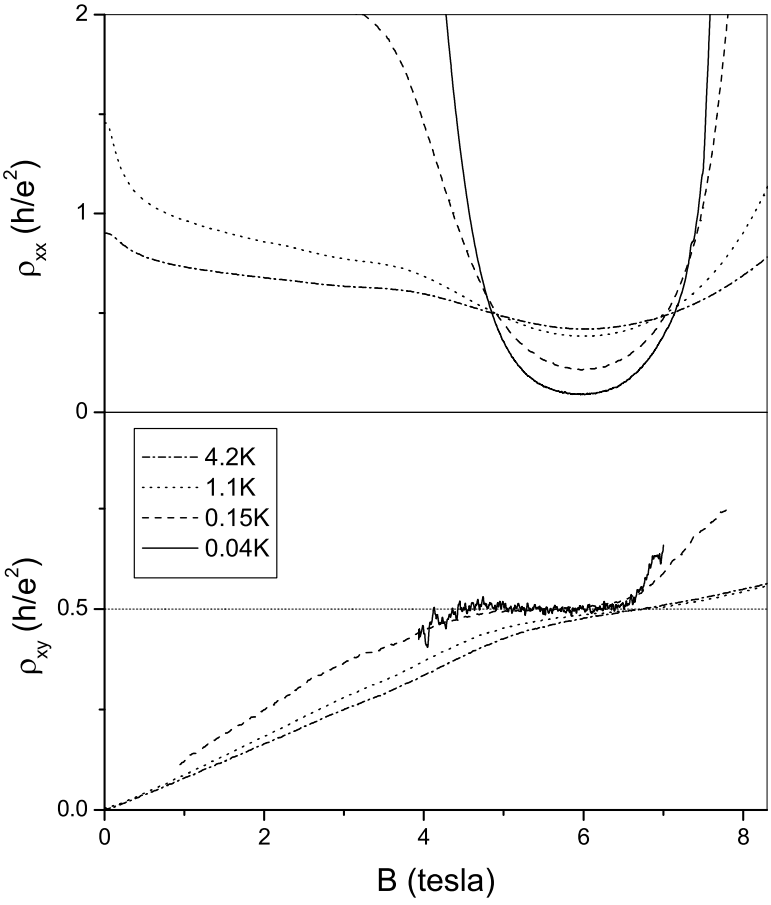

Figure 5.2: Magnetoresistivity data for sample 30. As for sample 27, ρ_{xy} at the lowest temperatures can only be measured around the minimum of ρ_{xx}.

Both have in common a very high resistivity at zero magnetic field (of the order of 10 MΩ at $T = 50$ mK) that is decreasing strongly for increasing magnetic field, giving a minimum around $B = 6$ T, before strongly increasing again in high magnetic fields above 7 tesla. According to our definition, the two samples show insulating behavior in small and in very high magnetic fields. In contrast to sample 27, for which ρ_{xx} increases with decreasing T for all magnetic fields, sample 30 show a quantum Hall phase between 5 and 7 tesla, where ρ_{xx} decreases with decreasing T, and ρ_{xy} shows a plateau at the lowest temperatures. Sample 27 shows an almost temperature independent ρ_{xy}.

In the case of strongly disordered systems it is usually more instructive to

look at the conductivities which, according to (2.3) are calculated as follows:

$$\sigma_{xx} = \frac{\rho_{xx}}{\rho_{xx}^2 + \rho_{xy}^2}, \qquad \sigma_{xy} = \frac{\rho_{xy}}{\rho_{xx}^2 + \rho_{xy}^2}. \tag{5.1}$$

The results for sample 27 and 30 are shown in figures 5.3 and 5.4.

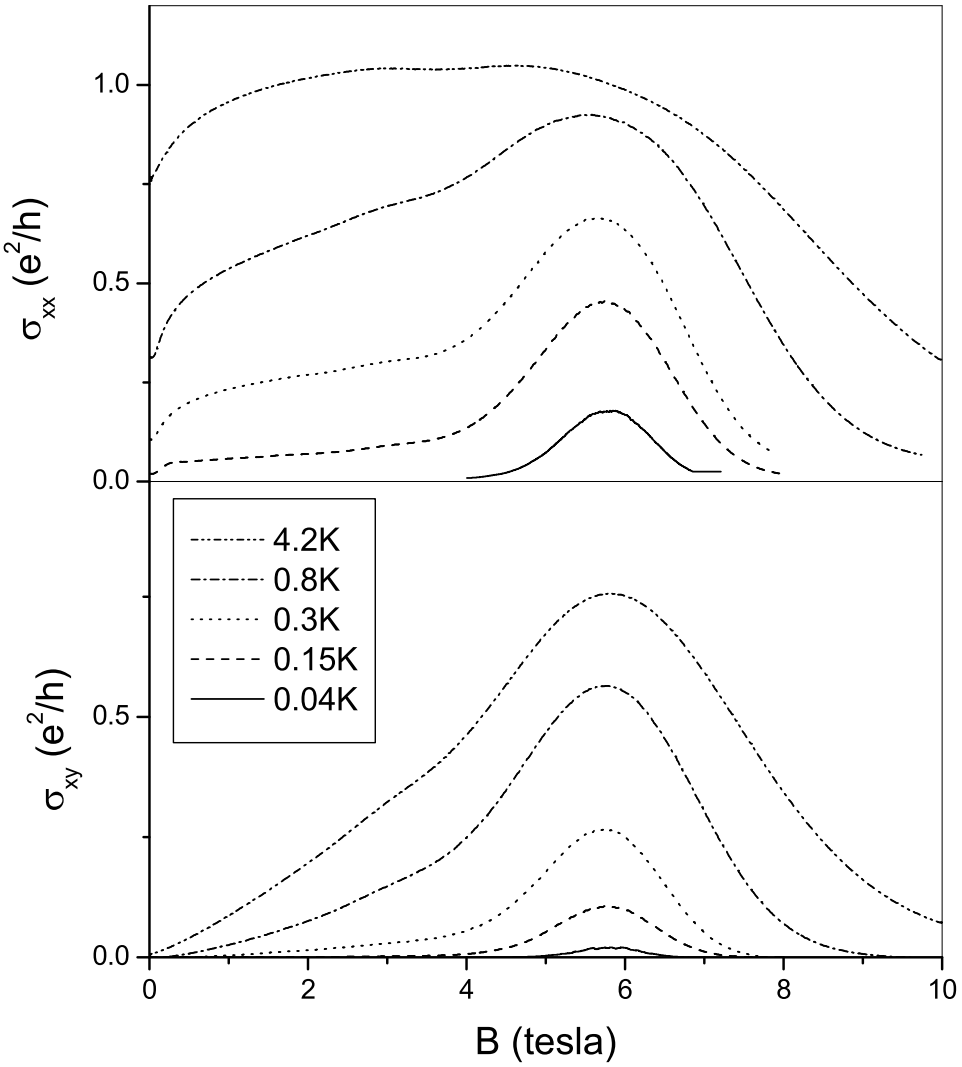

Figure 5.3: Magnetoconductivity data for sample 27

Sample 27 shows no pronounced structure in the magnetoconductivity; one notes that σ_{xx} and σ_{xy} decrease with decreasing T for all magnetic fields and have values close to zero for the lowest temperatures, confirming the behavior already indicated by the resistivity data.

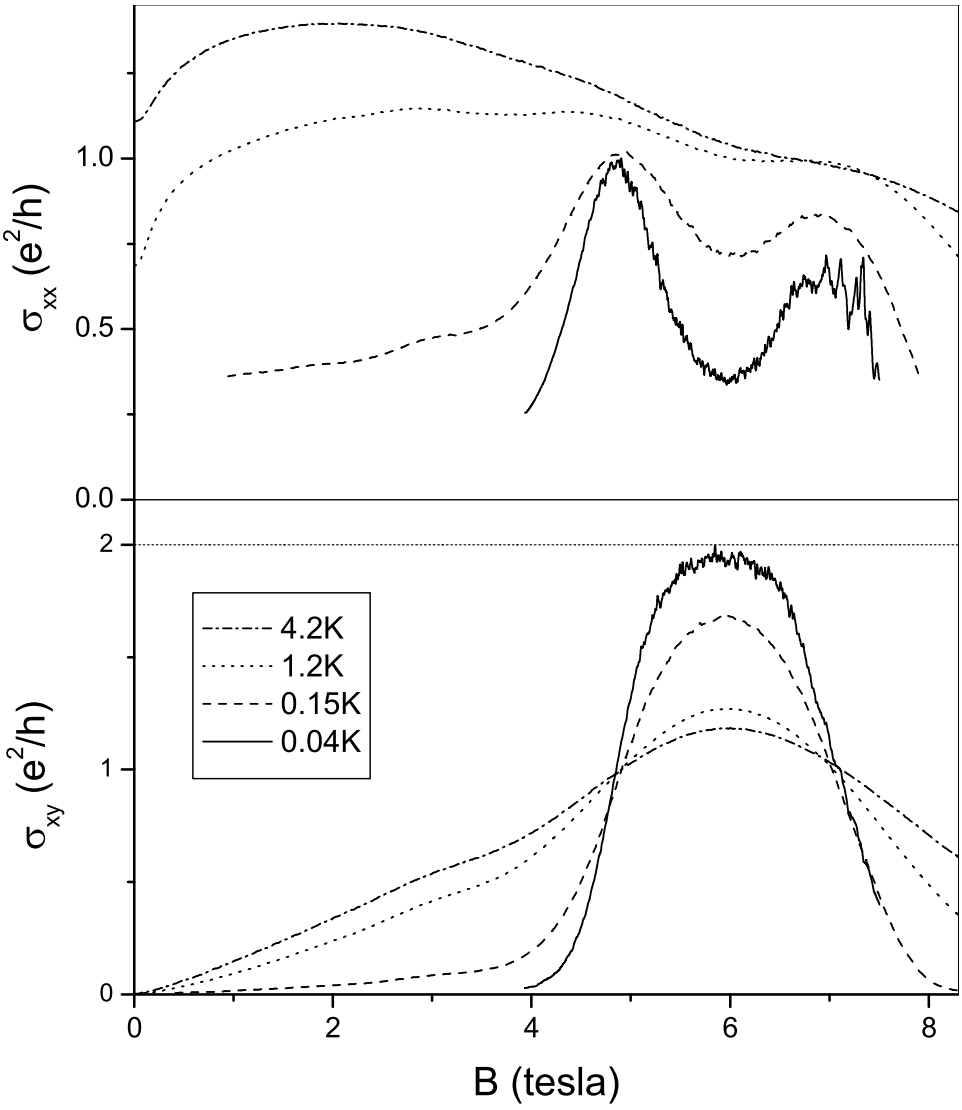

Figure 5.4: Magnetoconductivity data for sample 30

In contrast to this, sample 30 shows a well pronounced quantum Hall phase in σ_{xy} between 5 and 7 tesla, where the Hall conductivity increases with decreasing T and approaches the value of 2. In the same field interval σ_{xx} approaches zero, and develops two peaks around the transition points at 5 and 7 tesla, where σ_{xy} crosses the value of 1. Whereas the peak at $B = 5$ T approaches the value of 1, the second peak at $B = 7$ T is significantly broader and has a smaller maximum value. This is most likely due to the fact that the Zeeman splitting of the conduction electrons starts to become important at higher magnetic field, and begins to show up in the magnetoconductivity

data.

5.1.2 Metallic samples

Samples that fall in the range 34 nm $\leq d \leq$ 50 nm show, at the lowest temperatures, a well pronounced quantum Hall effect structure with a perfectly flat plateau at $\rho_{xy} = 1/2$ and $\rho_{xx} = 0$ between 7 and 11 tesla.

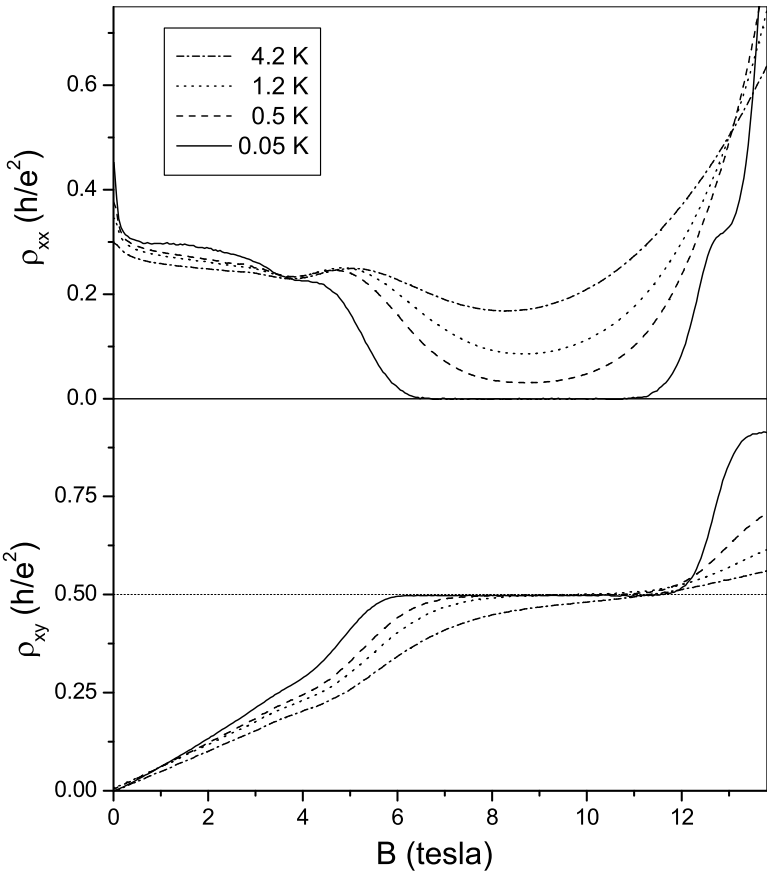

Figure 5.5: Magnetoresistivity data for sample 40

This quantum Hall state can be attributed to the completely filled lowest Landau level with a twofold spin degeneracy. The Fermi energy lies in the energy range of localized states between the 1 $\downarrow$ and the 0 $\uparrow$ Landau level, leading to the vanishing of ρ_{xx} in this field range. As there exist two bands of extended states below the Fermi energy (belonging to the 0 $\uparrow$ and 0 $\downarrow$ Landau levels), ρ_{xy} shows a plateau at the value of 1/2 instead of 1. At magnetic fields around 12 tesla, at $T \leq 100$ mK, one can notice a weakly pronounced saddlepoint in ρ_{xx} and a change of slope in ρ_{xy}. This feature is

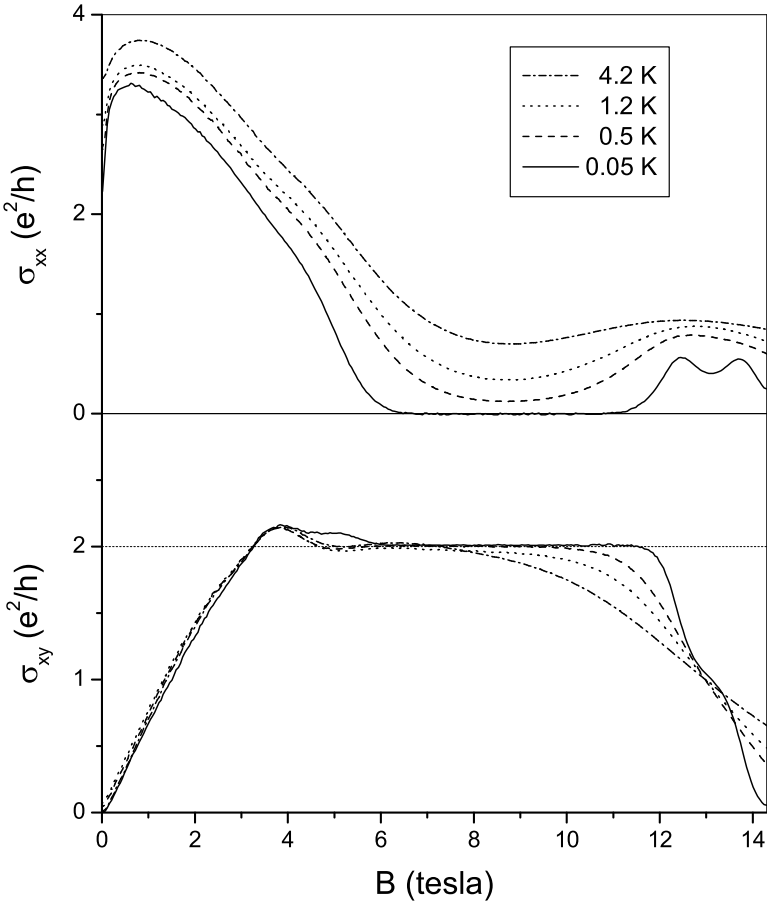

Figure 5.6: Magnetoconductivity data for sample 40

more pronounced in the magnetoconductivity data (figure 5.6), that show a clear minimum in σ_{xx} and the onset of a plateau in σ_{xy}. These features can be seen as the precursors of a quantum Hall state at $\rho_{xy} = 1$, which just begins to develop at these temperatures. As this state is due to the Zeeman splitting $\Delta E_Z = g\mu_B B$ of the lowest Landau level, and as in GaAs with its small g-factor ($g = -0.44$) this splitting is rather small, it only shows up in the magnetotransport data at very low temperatures below 300 mK[2]. The quantum Hall state at $\rho_{xy} = 1/2$, which is due to the Landau level splitting $\Delta E = \hbar\omega_c$ develops already at much higher temperatures and is much more pronounced because the cyclotron gap separating the $1\downarrow$ and the $0\uparrow$ level is much larger than the Zeeman gap between the $0\uparrow$ and $0\downarrow$ levels. This par-

[2] This is true also if we consider the exchange enhancement of the g-factor: $g^*\mu_B B = g\mu_B B + p \cdot e^2/\epsilon l_B$ (with the spin polarization p). g^* will be small, as p is small in our systems.

tially developed quantum Hall state at $\rho_{xy} = 1$ could be observed in samples 34, 37, 40, 50 and, to a smaller extent, also in sample 30 (see chapter 5.1.1). Samples 70 shows only one quantum Hall phase at $\rho_{xy} = 1/2$, which is however not fully developed, with a minimum in ρ_{xx} not decreasing to zero and a plateau in ρ_{xy} that is not perfectly flat. There is no sign of a quantum Hall phase at $\rho_{xy} = 1$ detectable. The magnetoresistivity data for sample 70 is shown in chapter 5.5.

Weak localization in metallic samples

The metallic samples all show a distinct sign of weak localization around $B = 0$, visible as a peak in ρ_{xx} or a dip in σ_{xx}, which can be seen in figures 5.5 - 5.7. As it has been show in chapter 3.3.1, a measurement of the suppres-

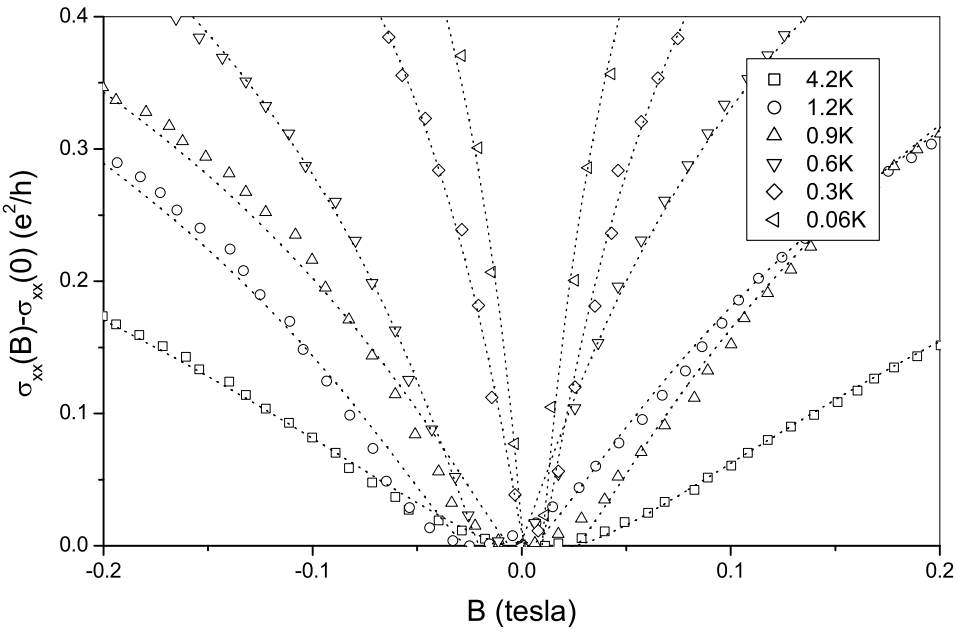

Figure 5.7: Sample 40: dip in σ_{xx} around $B = 0$ due to weak localization corrections. Lines give the results of a fit to (3.15), the corresponding values for L_{in} are given in figure 5.8

sion of weak localization by magnetic field allows to determine the inelastic scattering time τ_{in} and in consequence also the inelastic scattering length $L_{in} = \sqrt{D\tau_{in}}$ of the conduction electrons at $B \approx 0$. We show $\Delta\sigma_{xx}(B)$ in the vicinity of $B = 0$ for sample 40 in figure 5.7, together with fits to (3.15). The corresponding values of the inelastic scattering length L_{in} are shown in figure 5.8. The resulting values for L_{in} lie in the range of 74 - 313 nm, and

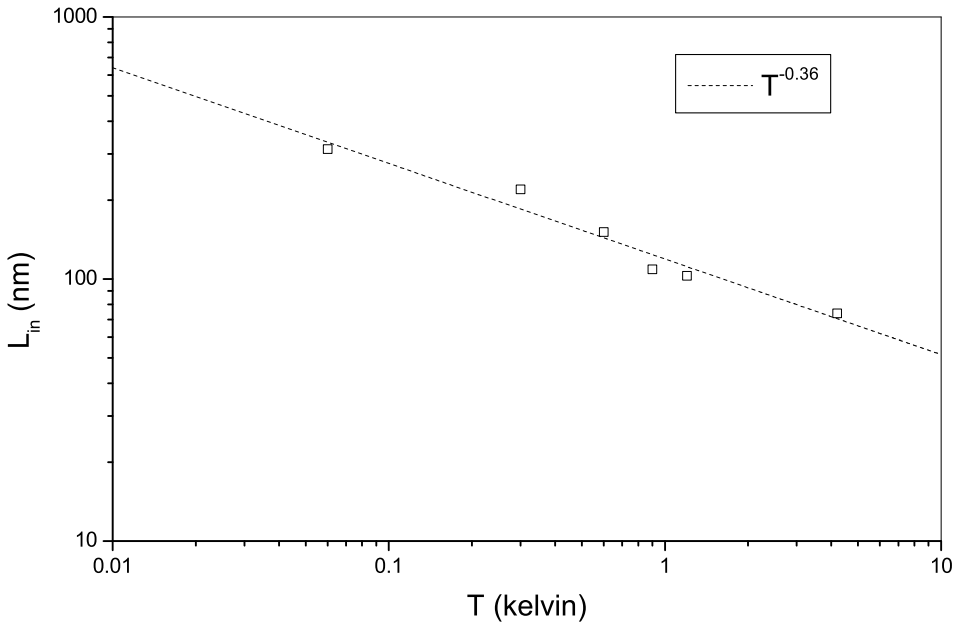

Figure 5.8: L_{in} for sample 40 derived from fits to (3.15) shown in figure 5.7. Values range from 74 nm at $T = 4.2$K up to 313 nm at $T = 60$mK

fit to a simple power law with an exponent close to 0.5, a value predicted by theory. Note that this behavior of L_{in} applies to the vicinity of $B = 0$ only; in strong magnetic fields L_{in} usually shows a different behavior. We think however, that the results for $B \approx 0$ still give the correct order of magnitude that can be expected for L_{in} in high magnetic fields. As a main result it can be retained, that the value of L_{in} increases to values much larger than the layer thickness of our samples, as the temperature decreases to values below 1 K.

5.2 Flow

For samples with a small maximum Hall conductivity (namely samples 27, 30 and 34) we have measured the temperature dependence of σ_{xx} and σ_{xy} at different magnetic fields, to test the agreement with the flow diagram [26] and the theory introduced in [30], that allows an actual calculation of the flow lines in the diagram. As the theory from Dolan [30] has been derived for spinless electrons, the question arises how experimental data from a spin-1/2 electron system can be compared to this theory. We assume, that the conductivities can be separated into two contributions from each spin orientation

$$\sigma_{ij} = \sigma_{ij}^{\uparrow} + \sigma_{ij}^{\downarrow}, \tag{5.2}$$

which is justified in the absence of spin-flip scattering. The theory then should apply to the two spin orientations independently. In general however, $\sigma_{ij}^{\uparrow} \neq \sigma_{ij}^{\downarrow}$, and there is no way to separate the two contributions experimentally except in two limiting cases:

1. total spin polarization
   In this case the total conductivity can be identified with the conductivity of one of the two spin orientations for a certain field interval, the contribution of the other spin orientation being zero in the same magnetic field range:

   $$\sigma_{ij} = \sigma_{ij}^{\uparrow} \quad \text{or} \quad \sigma_{ij} = \sigma_{ij}^{\downarrow}. \tag{5.3}$$

   This case is often found in clean systems in high magnetic fields, when the Zeeman energy is larger than the disorder broadening of the Landau levels.

2. total spin degeneracy
   In this case one can assume the two spin orientations to give identical contributions to the total conductivity:

   $$\sigma_{ij} = 2 \cdot \sigma_{ij}^{\uparrow} = 2 \cdot \sigma_{ij}^{\downarrow}. \tag{5.4}$$

   This is the case in situations where the Zeeman energy is negligible compared to the disorder broadening of the Landau levels, e.g. in strongly disordered systems with a small electronic g-factor.

Case 1 is obviously not realized in our samples. As mentioned in chapter 5.1 there are some signs of spin splitting visible in the magnetotransport of

samples 34-50 around $B = 12$ T, but the splitting is not completely resolved, and a separation of the two spin orientations is not possible. The transition from the low field insulating state to the quantum Hall state at $\sigma_{xy} = 2$ however can be considered as spin degenerate according to case 2, as it occurs at smaller magnetic fields where there is no sign of spin splitting detectable. We can therfore compare the magnetoconductivities of our samples around this transition (around $B = 6$ T) with theory by dividing σ_{xx} and σ_{xy} by 2. The magnetoconductivity data of samples 27, 30 and 34 have been measured as a function of temperature at a number of fixed values of the magnetic field B, and are shown as a plot of $\sigma_{xy}/2$ versus $\sigma_{xx}/2$ (visualizing the so called *temperature driven flow*) in figures 5.9, 5.10 and 5.11. Note that, according to chapter 3.2.2, the flow lines shown in figures 5.9-5.11 are uniquely determined by σ_{xy}^{∞}, the value of σ_{xy} for $\sigma_{xx} \gg 1$.

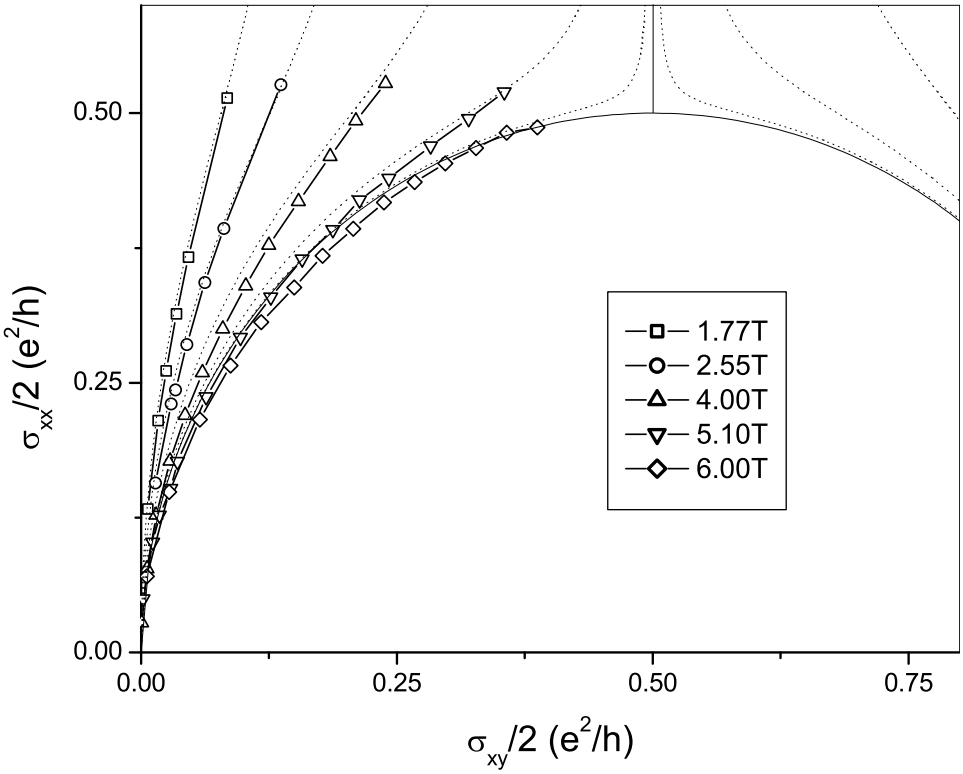

Figure 5.9: Temperature driven flow for sample 27. The temperature ranges from 4.2K down to 50mK. Dotted lines are flow lines calculated from theory.

Sample 27, although strongly insulating and not showing a real quantum Hall phase nevertheless gives temperature driven flow lines that agree nicely with the flow diagram as predicted by theory. All points showing a finite

Hall and diagonal conductivity at high T flow towards the low field insulator state at (0,0) for decreasing temperature and evolve close to the semicircle around (0.5,0).

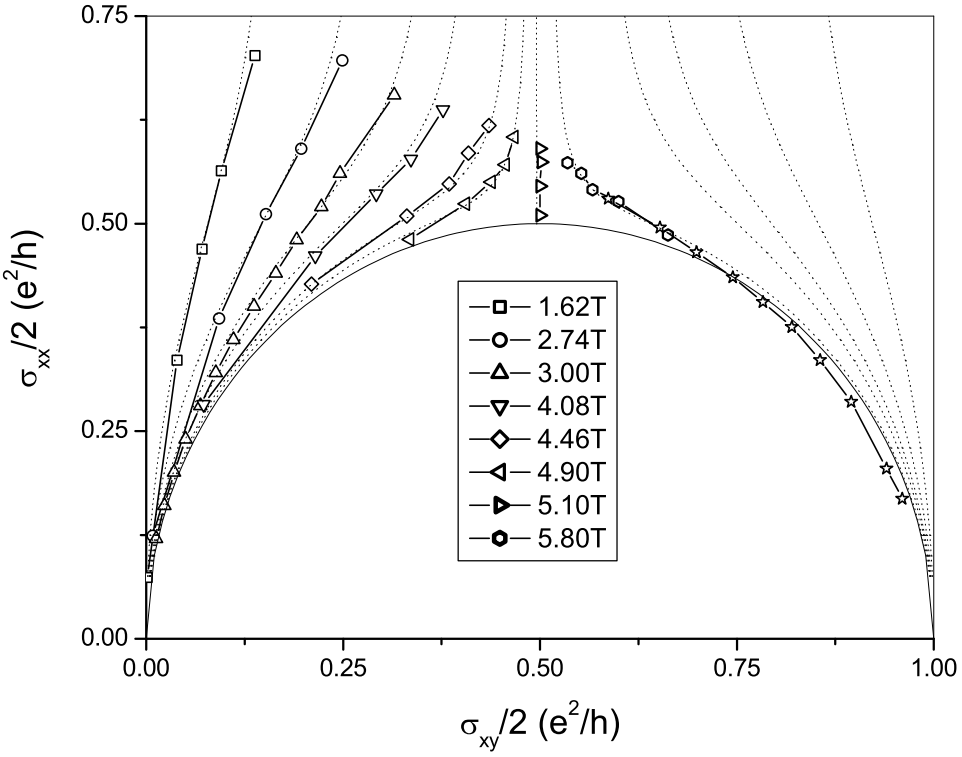

Figure 5.10: Temperature driven flow for sample 30.

Sample 30, having a maximum $\sigma_{xy}^{\infty}/2$ larger than 0.5 and showing a real quantum Hall phase, reproduces both halfs of the semicircle. Points with $\sigma_{xy}^{\infty}/2 < 0.5$ flow to the low field insulator at (0,0) whereas points with $\sigma_{xy}^{\infty}/2 > 0.5$ flow to the point at (1,0), that represents the first quantum Hall phase. The flow line belonging to $\sigma_{xy}^{\infty}/2 = 0.5$ tends towards the unstable fixed point at (0.5,0.5), marking the critical point for the transition between low field insulator and quantum Hall state. Sample 34, being the thinnest metallic sample and therefore showing a rather high conductivity at low fields even at the lowest temperatures doesn't reach the semicircle in its flow lines. But even at rather large values of σ_{xx}, the measured flow lines agree reasonably well with the theoretical ones, and the evolution towards the quantum Hall state at (1,0) happens as expected from theory.

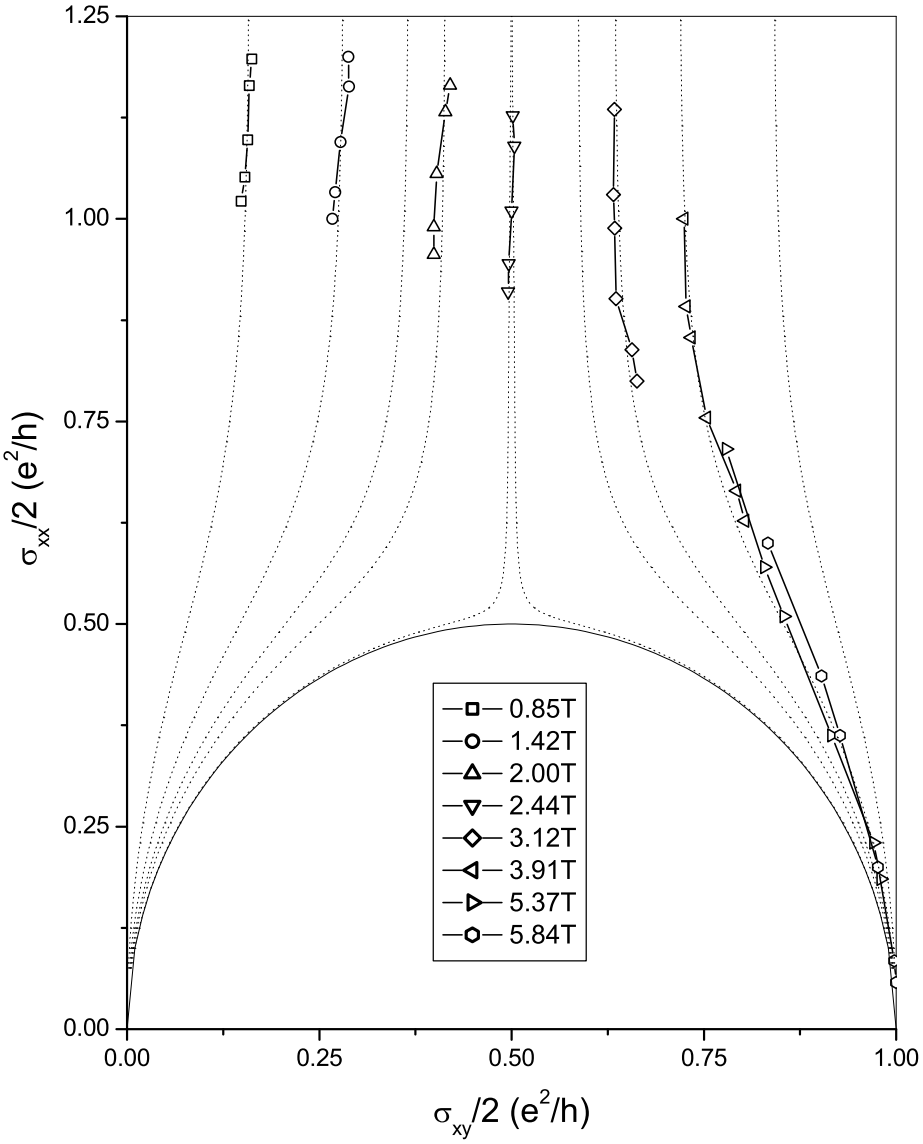

Figure 5.11: Temperature driven flow for sample 34

Trying to compare our results with previous investigations of the flow diagram in the literature, one finds that earlier experiments of the temperature driven flow lines have usually been performed on heterostructure samples with higher mobility [64]. To our knowledge, agreement with an accuracy as presented here has not been observed before.

5.3 Temperature dependence

5.3.1 σ_{xx}(T) for large σ_{xx} – logarithmic corrections

As has been shown in previous work on samples with a larger layer thickness (d = 100, 140 nm [61]), for large values of σ_{xx} the temperature dependence of the diagonal conductivity is logarithmic. According to chapter 3.3.2 this could be due to single particle localization or to interaction corrections. As has been shown in [40], existing models for single particle corrections fail to explain the magnitude of the logarithmic corrections measured in our samples. Therefore we have proposed in [65] to consider interaction corrections for the explanation of the temperature dependence of σ_{xx} in this system in the relevant range of B and T.

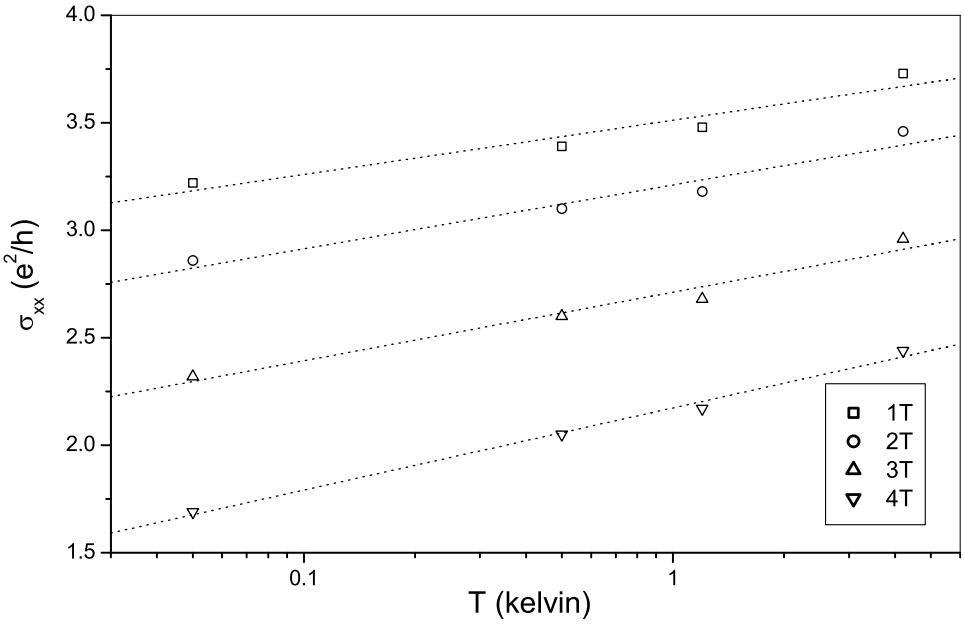

Figure 5.12: T-dependence of σ_{xx} for sample 40 for magnetic fields between 1 and 5 tesla. Dotted lines give the results of fit to (3.19).

As can be seen in figure 5.12, the temperature dependence of σ_{xx} in field ranges where σ_{xx} is large is to a good approximation logarithmic. Deviations at the lowest temperatures are most probably consequence of errors in the temperature due to thermometer magnetoresistance. Fits to (3.19) give a value of $\lambda = 0.43 \pm 0.06$ for the interaction constant λ, which is consistent with the theoretical prediction $\lambda \leq 1$. Fitting the data from figure 5.12 to the formula for single particle localization corrections (3.18) gives values of $\sigma_{xx}^0 < 1$, which is in disagreement with the experimental observations. As can be seen in figure 5.6, for fields up to 4 tesla, σ_{xy} doesn't change significantly between 4.2 and 0.05 kelvin.

5.3.2 $\rho_{xx}(T)$ for $\sigma_{xx}(T) \to 0$ – hopping conduction

In samples showing a well pronounced quantum Hall state, with σ_{xx} approaching 0 in the quantum Hall minimum, a different conduction mechanism becomes important. As in this range of magnetic field the electronic wave functions around the Fermi energy are localized, the finite value of σ_{xx} at nonzero temperature must be due to hopping of electrons between localized states. Different mechanisms of hopping (thermal activation, phonon assisted hopping) have been discussed in chapter 3.4.
We could observe hopping conduction in all metallic samples that show a fully developed quantum Hall state, namely samples 34, 37, 40 and 50. Hopping conduction was found for values of $\sigma_{xx} < 0.1$ at magnetic fields corresponding to the middle of the quantum Hall minimum and up to 1.8 tesla above it. We have investigated this transport regime in detail for sample 40, and have compared $\rho_{xx}(T)$ to the following equation:

$$\rho_{xx}(T) = \rho_{xx}^0 \cdot \exp\left(-\left(\frac{T_0}{T}\right)^p\right) \tag{5.5}$$

As already noted in chapter 3.4, in a quantum Hall minimum, contrary to the zero field case, the argument of the exponential in (5.5) is negative and ρ_{xx}, being proportional to σ_{xx}, decreases with temperature.
To decide about the value of the hopping exponent p one can use a least-square fitting algorithm; but as this method may give values for the fitting parameters that correspond to a local minimum in the fit functional, we have used an alternative method for the determination of p, which is exact in the case of a non-temperature dependent prefactor ρ_{xx}^0. This method was originally proposed by Zabrodski and Zinoveva [66], and makes use of a plot of the reduced activation energy g defined by

$$g = \frac{d\ln\rho_{xx}}{d\ln T} = \frac{T}{\rho_{xx}} \cdot \frac{d\rho_{xx}}{dT}, \tag{5.6}$$

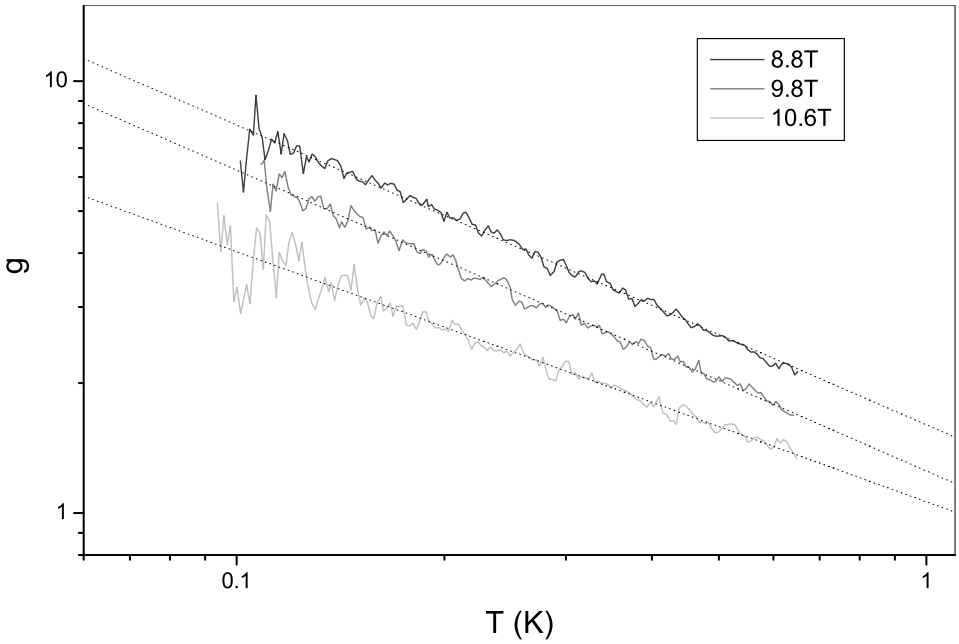

Figure 5.13: Zabrodski-Zinoveva plot of the T-dependence of ρ_{xx} in the quantum Hall minimum for sample 40. The hopping exponents p are 0.69 (B = 8.8 T), 0.69 (B = 9.8 T) and 0.58 (B = 10.6 T). The temperature range has been limited to below 700 mK, as at higher temperatures crossover, probably to thermally activated hopping with $p = 1$ takes place.

which for the case of a hopping law with temperature independent prefactor (3.20) is equal to $p \cdot (T_0/T)^p$. One can then determine p with the help of a double-logarithmic plot of g. A corresponding analysis of the $\rho_{xx}(T)$-data of sample 40, measured at B = 8.8 T, 9.8 T and 10.6 T is presented in figure 5.13[3]. The results for p (extracted from the Zabrodski-Zinoveva plot), T_0 and ρ_0 (found from a subsequent least square fit with p fixed) are shown in the table below.

B (T)	$\rho_0(h/e^2)$	T_0 (K)	p
8.8	0.804±0.004	3.03±0.01	0.69±0.01
9.8	0.672±0.004	2.35±0.02	0.69±0.01
10.6	0.795±0.003	2.38±0.01	0.58±0.01

[3]For the calculation of g a small, home-written C++ program was used. Due to an unavoidable, rather large noise level on both ρ_{xx} and T, careful filtering of our data (using a Lanczos differentiating filter [67]) was necessary. Even the filtered data show an important noise level, but they nevertheless allow for a reliable linear fit on a double-log plot

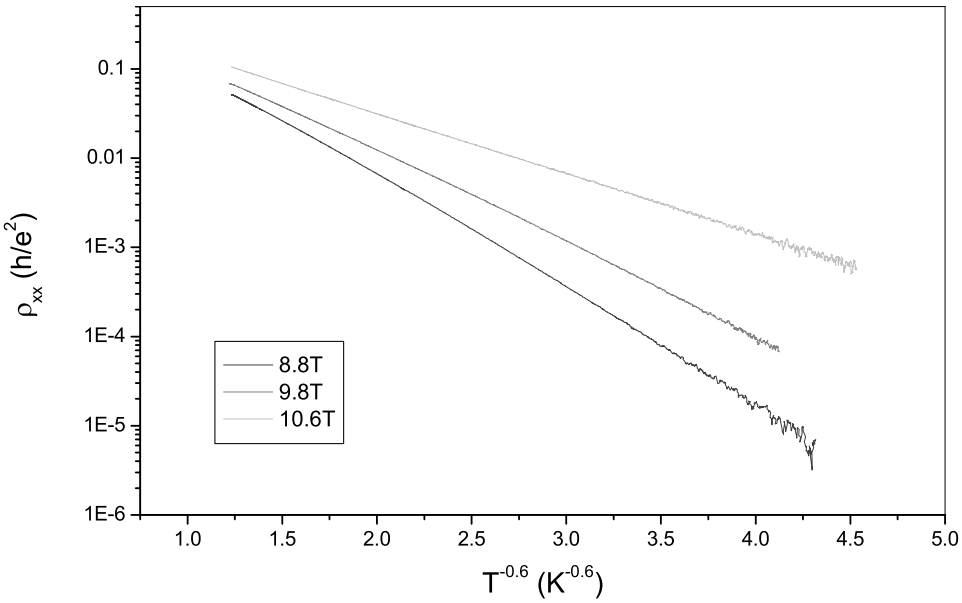

Figure 5.14: Sample 40: T-dependence of ρ_{xx} around the quantum Hall minimum. Dotted lines are fits to (5.5) using the hopping exponents p extracted from figure 5.13.

5.4 Scaling

To observe scaling behavior of a transition between two quantum Hall states or between the high- or low-field insulating state and a quantum Hall state as presented in chapter 2.3, one needs a well developed and well resolved transition region. Unfortunately, in most of our samples this is not the case, as for most transitions between the low field insulating state and the quantum Hall state at $\sigma_{xy} = 2$ either the insulating state (samples 34, 37, 40 50) or the quantum Hall state (sample 27) are not fully developed. The transition between the quantum Hall state and the high field insulating state can not be analyzed either, because a quantum Hall state at $\sigma_{xy} = 1$ only starts to show below $T = 300$ mK and is not fully developed even at the lowest temperatures. It is only in sample 30, that there is a well resolved and well isolated transition visible in the magnetoconductivity data, that we could analyze with respect to its scaling behavior. The scaling exponent extracted from the slope of $\partial\sigma_{xy}/\partial B$ at $B_c = 4.85$ T is equal to $|\mu| = 0.42 \pm 0.04$, and is therefore in agreement with theoretical predictions of $\mu = 0.43$ [68]. We should note however, that our result does not agree with the data of Hwang et al. [69], who have found an exponent of $\mu = 0.21$ for a spin degenerate plateau-plateau transition in low mobility InGaAs/InP heterostructures. It

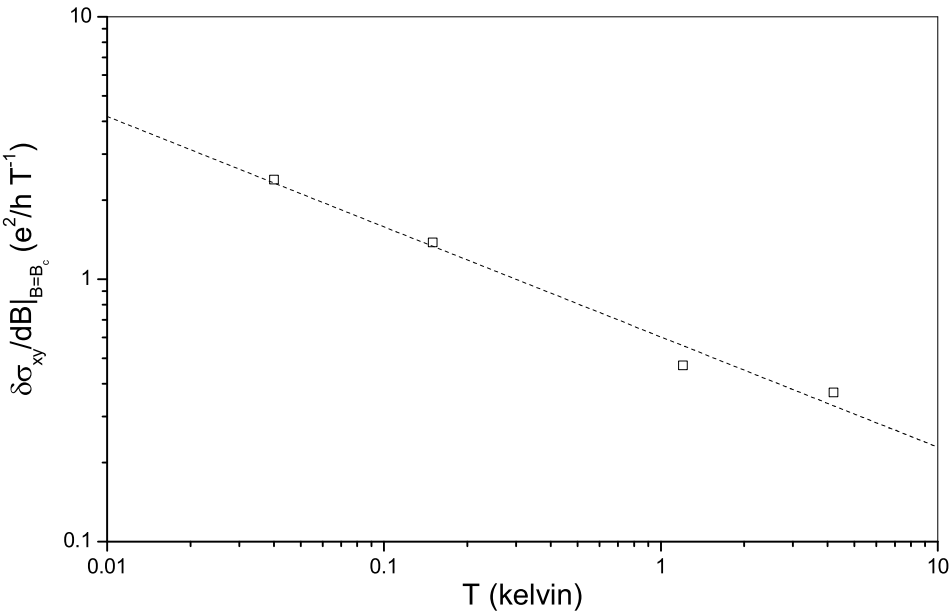

Figure 5.15: Sample 30: T-dependence of $\partial\sigma_{xy}/\partial B$ at $B = B_c$ for sample 30. The dotted line corresponds to a powerlaw with an exponent of -0.42.

should be noted that the phase transition investigated here is a transition between the low field insulating state and a quantum Hall state at $\sigma_{xy} = 2$. It is as such not associated with a Landau level, but it is a real low-field transition in the sense of chapter 2.4 caused by an extended state crossing the Fermi level while floating upwards in energy.

5.5 Angle dependence

As mentioned in chapter 4, in most of our samples the elastic mean free path l of the conduction electrons is clearly inferior to the thickness of the conducting layer. As this of course raises the question if, and under which aspect this might affect the effective dimensionality of the systems, the behavior of the transport coefficients with respect to the orientation of the system to magnetic field is of interest. Having a dilution refrigerator available that permitted to rotate the sample in situ at low temperatures, we could investigate the angle dependence of the quantum Hall effect in our samples with good precision. This has been done for sample 34, showing a fully developed quantum Hall effect state at $\rho_{xy} = 1/2$. and for sample 70, showing a partially developed quantization, also at $\rho_{xy} = 1/2$. The results are shown in figures 5.16 and 5.17. The configuration of the measurement is indicated in

the insert of figure 5.16.

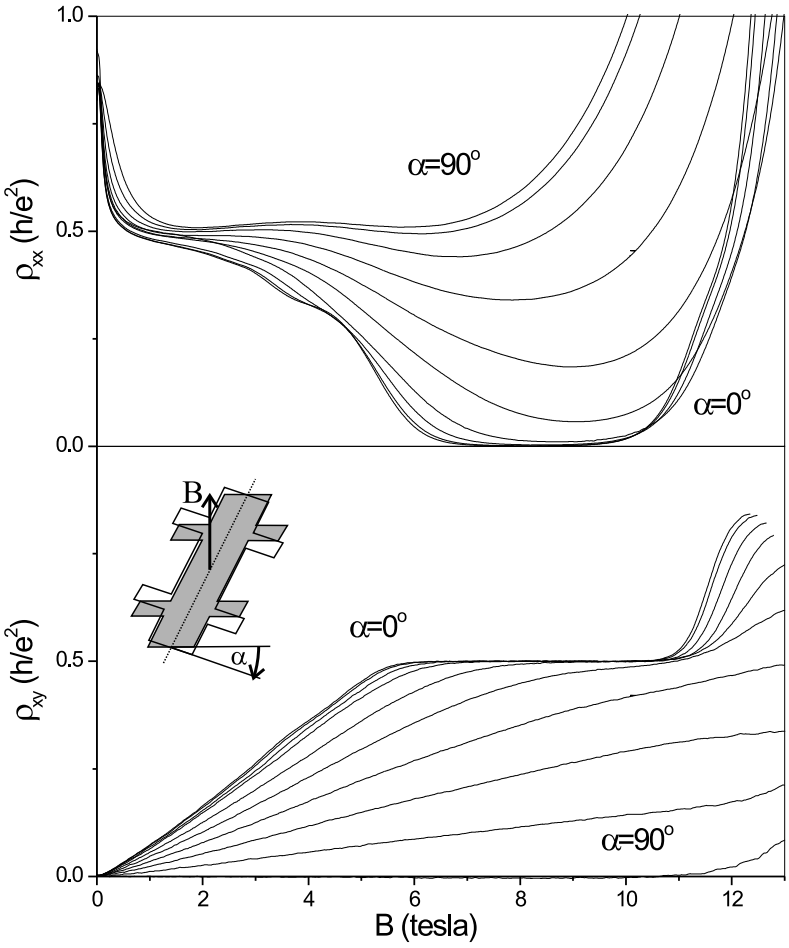

Figure 5.16: Diagonal and Hall resistivity for sample 34 at $T = 50$ mK as a function of the tilting angle α; angles are shown from 0^o to 90^o in steps of 10^o.

As expected, all quantum Hall effect structures are strongly suppressed, as the sample gets turned to an orientation parallel to the magnetic field. The minimum in ρ_{xx} becomes less pronounced, and at $\alpha = 90^o$ is more or less equal to the high temperature ($T = 4.2$ K) data for ρ_{xx} taken in perpendicular orientation. The Hall resistivity ρ_{xy} gradually vanishes and is zero at $\alpha = 90^o$. The small nonzero contribution at $B \geq 11$ T for sample 34 and at $B \leq 1$ T and $B \geq 6$ T for sample 70 at $\alpha = 90^o$ visible in figures 5.16 and 5.17 are due to a small admixture of ρ_{xx} caused by sample inhomogeneities or a small misalignment of the sample.

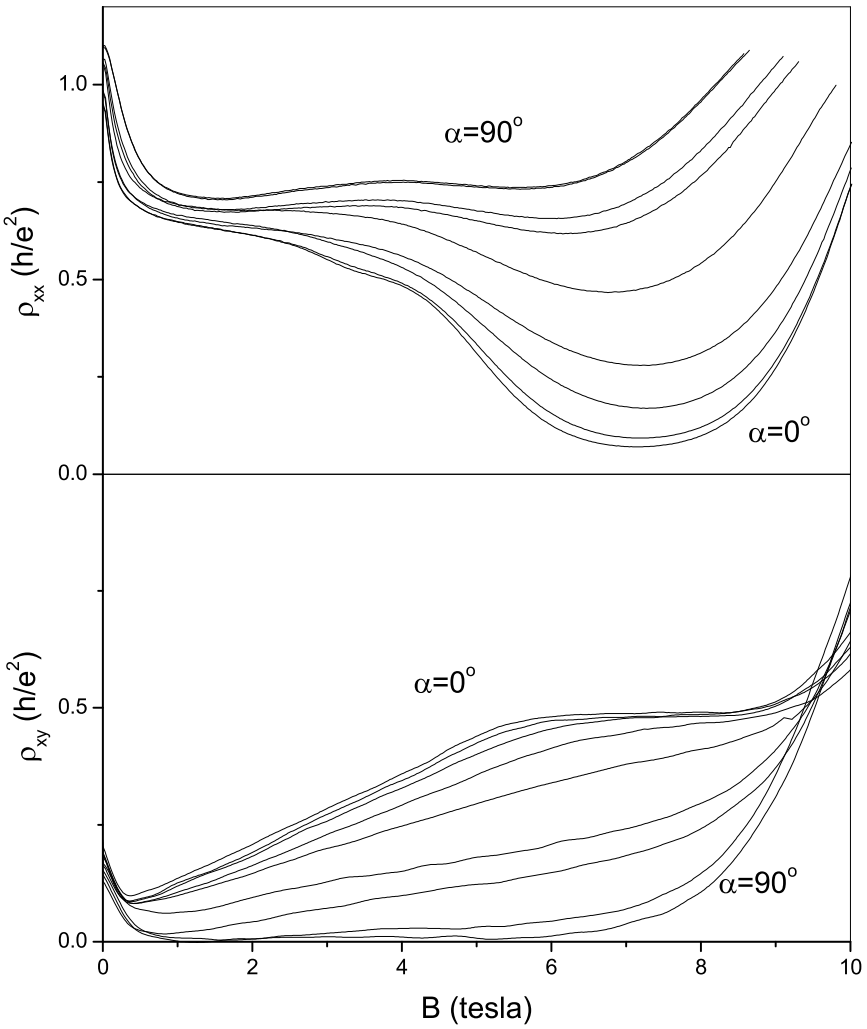

Figure 5.17: Diagonal and Hall resistivity for sample 70 at $T \approx 50$ mK as a function of the tilting angle α

In figures 5.18 and 5.19 we show the position of the minimum in $\rho_{xx}(B)$ as a function of α. As a purely two-dimensional system should only "feel" the perpendicular component $B_\perp = B \cdot \cos(\alpha)$ of the magnetic field, in a plot versus the total field B the minimum should shift to higher fields with a $1/\cos(\alpha)$ characteristics. One can see in figure 5.18 that for sample 34 this

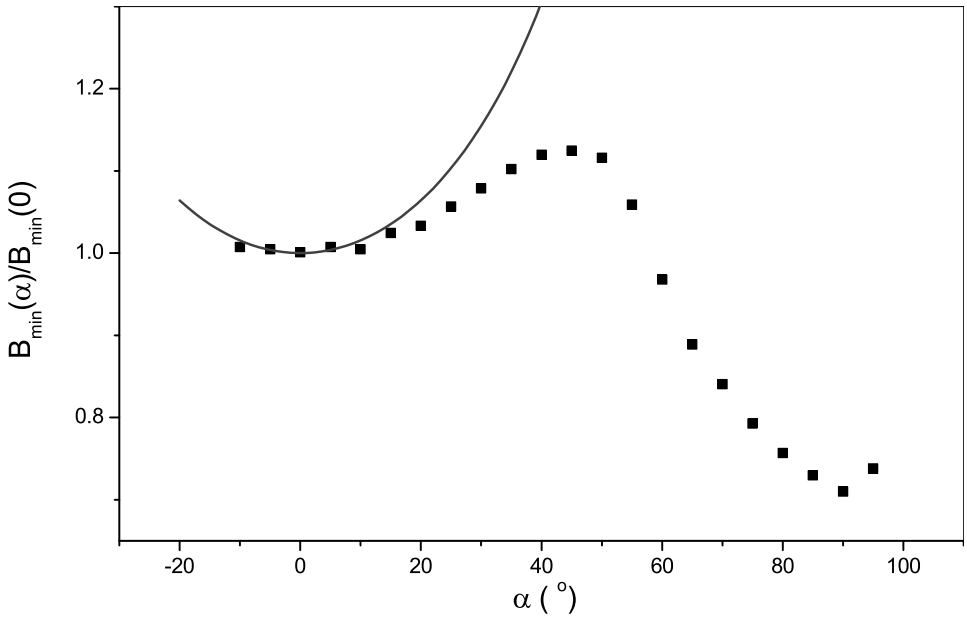

Figure 5.18: Position of the minimum of ρ_{xx} in figure 5.16 (sample 34) as a function of the tilting angle α. The line shows the $1/\cos(\alpha)$ behavior, expected for an ideal two-dimensional system

is the case for angles up to $\alpha \approx 20^o$. Sample 70 doesn't show the expected $1/\cos(\alpha)$-behavior at any angle (see figure 5.19). For $\alpha > 50^o$ the minimum of ρ_{xx} even starts to shift in the opposite direction towards lower fields for both samples. Obviously, this behavior is due to a different effect, which we were not able to determine up to now.

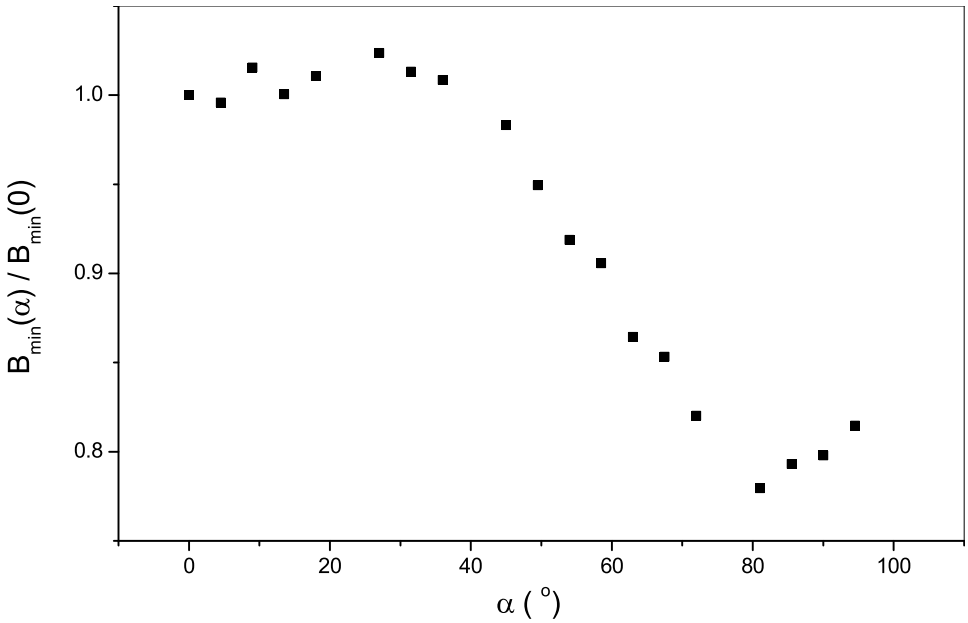

Figure 5.19: Position of the minimum of ρ_{xx} in figure 5.17 (sample 70) as a function of the tilting angle α

For the value of ρ_{xx} at its minimum theoretical predictions are much more difficult to make, as the transport properties are affected by a lot of factors that are mostly unknown. An important contribution in parallel orientation ($\alpha = 90^o$) in general is the scattering of conduction electrons between states belonging to different dimensional subbands. These transitions are normally forbidden in perpendicular orientation ($\alpha = 0^o$), and can only take place in the presence of an in-plane magnetic field $B_{\|}$. In the samples we have investigated, there are two (sample 34) or four (sample 70) subbands occupied. However, as it has been shown in chapter 4, the dimensional subbands will overlap strongly due to disorder broadening. We therefore do not believe that increased inter-subband scattering is responsible for the unusual angle dependence of the quantum Hall effect observed here. As discussed in chapter 3.3.2, the mechanism leading to a decrease of ρ_{xx} with temperature is due to diffusive transport. With this in mind, we have derived a simple, phenomenological model based of the anisotropy of carrier diffusion in a layer in tilted magnetic field to describe the angular dependence of ρ_{xx} at its minimum. Details of the calculation are given in appendix B; as a main result we get

$$\rho_{xx}^{min}(\alpha) \propto \frac{1}{\sqrt{1 - A \cdot \cos^2 \alpha}} \qquad (A = 1 - \frac{\sigma_{xx}}{\sigma_{zz}}) \tag{5.7}$$

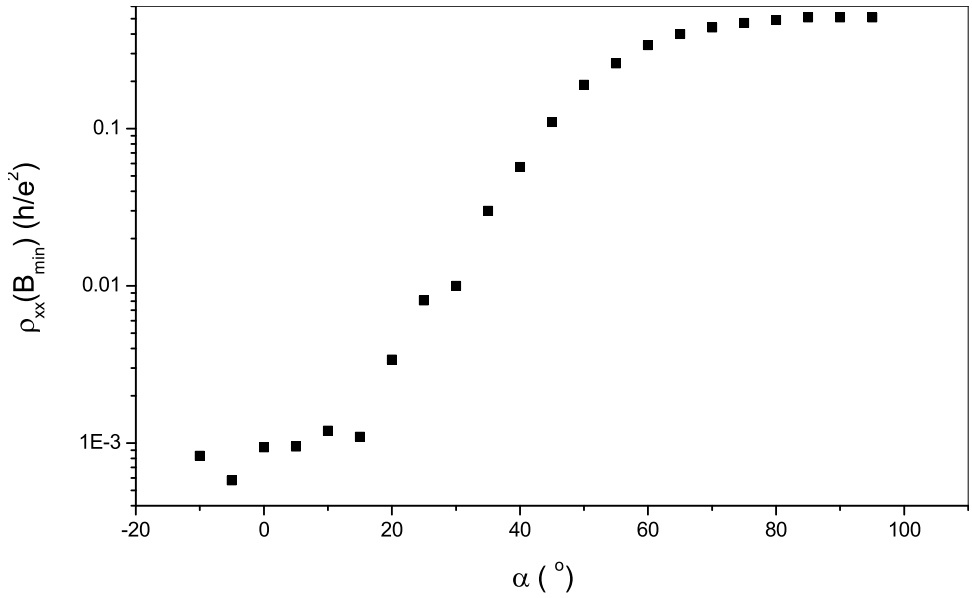

Figure 5.20: Value of the minimum of the diagonal resistivity ρ_{xx} in figure 5.16 (sample 34) as a function of the tilting angle α

For sample 70 a fit of $\rho_{xx}(B_{min})(\alpha)$ to (5.7) is shown in figure 5.21. The rather good fit yields a parameter $A = -0.78$, which implies $\sigma_{xx} > \sigma_{zz}$. This of course is unphysical, the Drude model suggests $A > 0.5$ for $\omega_c\tau > 1$. The model presented in chapter B therefore only gives qualitative agreement; for a quantitative description a more detailed theoretical approach would be necessary. The data for sample 34 cannot be fit with (5.7), a fact which is not surprising, as for this sample transport for small angles is dominated by hopping, and not by diffusion.

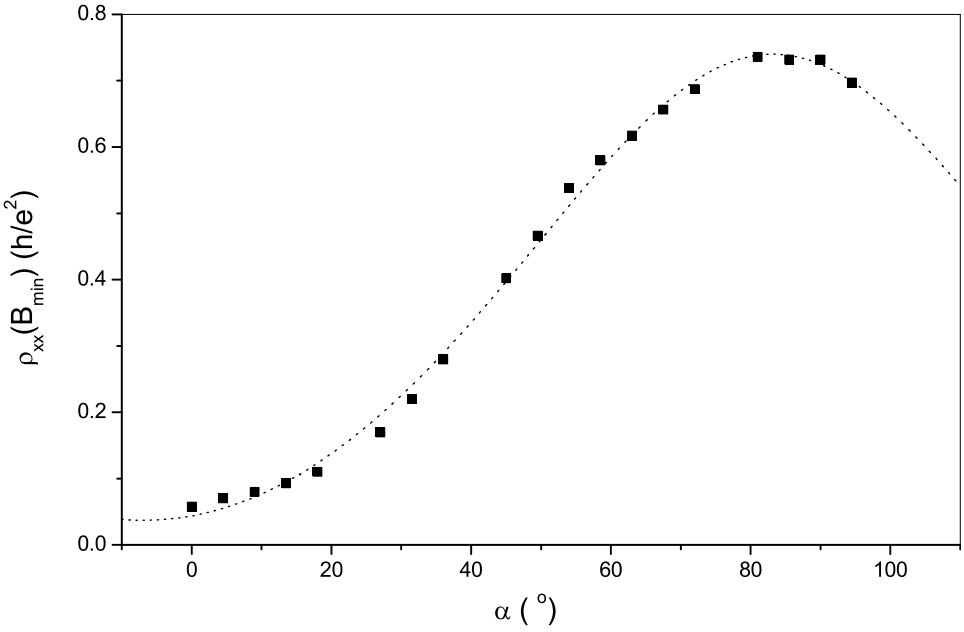

Figure 5.21: Value of the minimum of the diagonal resistivity ρ_{xx} in figure 5.17 (sample 70) as a function of the tilting angle α. The dotted line is a fit to (5.7).

Appendix A

Thermometry

In this chapter we will discuss a general problem that one has to face when doing experiments in magnetic fields and that becomes severe at temperatures below 1 kelvin: the determination of temperature in an experimentally suitable way. The major problem here is that commonly used resistance thermometers all develop a considerable magnetoresistance error at $T < 1$ K, and that other methods of thermometry are difficult to realize in real experimental situations. We will present a measurement of the magnetoresistance error of one Ruthenium-Oxide thick film resistor, that was used as resistance thermometers during this work; in a second part we report an experimental test of a new kind of primary thermometer that uses the Coulomb blockade effect and that we could show to be independent of magnetic field.

A.1 Field sweep experiments at constant temperature

In experimental physics at cryogenic temperatures one is usually faced with the need to measure temperature under various constraints, which can be limited space, fast response time, the presence of ionizing radiation or magnetic field. The thermometry method of an experiment therefore has to be chosen carefully, to exclude as far as possible any effect of the experimental environment onto the temperature measurement. One often encountered need is the determination of temperature in an arbitrary magnetic field, a task which is already quite difficult to achieve because most of the commonly used thermometers are to a certain extent affected by magnetic field and can give considerable errors in their temperature reading when used in magnetic field (see refs. [70] and [52] chapter 12 for some examples). In real world experiments temperature is almost always determined by a resistance mea-

surement. A special resistor, with a known dependence $R(T)$ is attached to the experiment with a good thermal contact and allows to determine T by measuring R. As $R(T)$ is usually determined by material parameters that are usually not precisely known, it cannot be calculated theoretically, and the resistance thermometer has to be calibrated against a different temperature standard. It is therefore called a secondary thermometer in contrast to primary thermometers, where the temperature dependence of a physical quantity is uniquely determined by first principles, and temperature can therefore be calculated directly from a measured quantity without the need for a calibration.

Resistance thermometers are widely used because they allow for an easy determination of T, they are cheap and can be made small in size. A major disadvantage is that their resistance in general will be affected by the experimental environment, which will lead to an error in a temperature reading, as the exact effect on the resistor is usually difficult to quantify. As can be seen in the main part of this work, magnetic field can have a dramatic effect onto resistance and, unfortunately, this is also the case for resistance thermometers.

The thermometers used to measure temperature in this work are Ruthenium oxide thick film chip resistors, which are cheap (they are a mass product of electronics industry), small in size, and usually have a good sensitivity in the temperature range of our experiments. They are believed to show a moderate magnetoresistance in the range of some percent. To check if this is true also at millikelvin temperatures and in high magnetic fields, we performed a field calibration of one of the thermometers that were used for this work.

This calibration was done in the Oxford Instruments Kelvinox$^{\text{TM}}$ top-loading dilution refrigerator described in chapter 4.2. The dilution cryostat was installed on a resistive magnet capable of producing a maximum magnetic field of $B = 28$ T. As magnetic field independent temperature standard we used a dielectric constant thermometer [71], consisting of a cylindrical capacitor with a special glass dielectric (Spectrosil, SiO_2 doped with 1200 ppm OH^-). The capacitance of the sensor as a function of temperature is shown in figure A.1. It shows a pronounced minimum at around 100 mK, and increases strongly for temperatures below. The sensitivity at 50 mK is about 0.5 fF per mK for our sensor with a total C of 370 pF. The capacitance of this type of sensor has been confirmed to be field independent up to values of $B = 9$ T [72].

Because of the poor reproducibility of the dielectric constant thermometer,

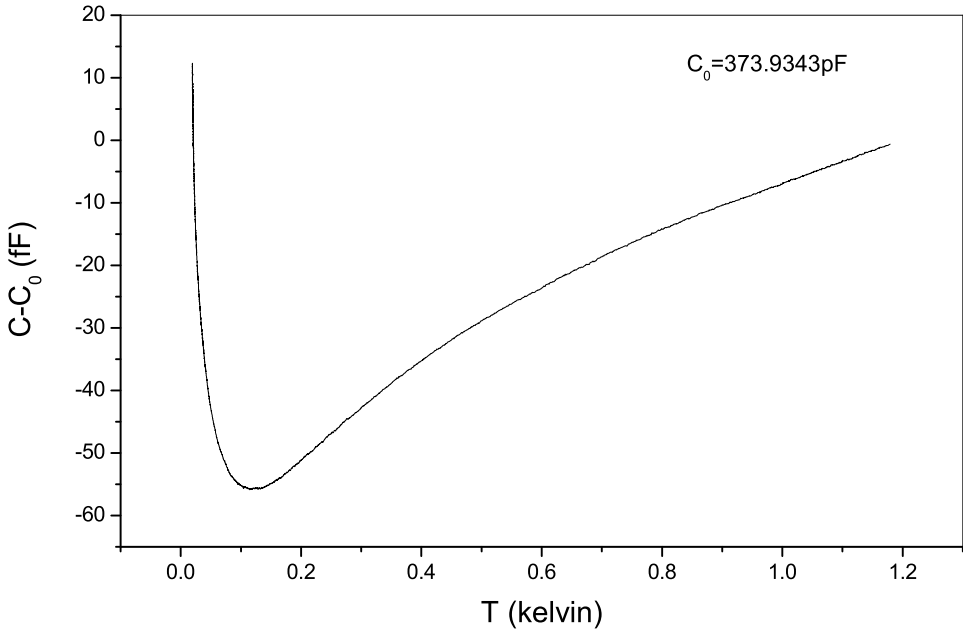

Figure A.1: $C(T)$ for the glass capacitor used as a magnetic field independent temperature standard

we used a calibrated Ge-resistor (Lakeshore) as our absolute temperature standard in zero magnetic field. All sensors were placed inside the mixing chamber of the dilution refrigerator in the diluted phase. They were positioned close together with good thermal coupling to each other in order to avoid temperature differences between them. The sensors were connected inside the cryostat by four 100 μm twisted-pair manganin wires, with a total lead resistance of about 100 Ω. Appropriate low-pass filters were connected at the top of the cryostat.
The capacitance of the dielectric constant thermometer was measured with a passive capacitance bridge (General Radio 1616) in a three terminal measurement mode, to eliminate the cable capacitances. The excitation of 5 V RMS amplitude at a frequency of $\nu = 4.8$ kHz was provided by the internal oscillator of a Stanford Research 830 Lock-In amplifier, which was also used to detect the off-balance signal of the capacitance bridge. The Ge-resistor was measured with a standard resistance bridge (Barras ORPX 2). The excitation voltage for the resistance measurement was checked to be low enough to avoid self heating of the sensor. For an experiment at fixed temperature, the mixing chamber was first adjusted to the desired temperature in zero field (verified by the Ge-sensor) and the capacitance bridge was balanced. For

the experiment in magnetic field, the mixing chamber temperature was then regulated by keeping the capacitance bridge balanced. For the regulation we used an analog PID controller (Linear Research 130). The amplified off-balance signal of the capacitance bridge provided by the analog output of the Lock-In amplifier was used as the temperature offset signal. With this setup, the capacitance of the dielectric constant thermometer could be kept stable to within 2×10^{-6} (± 0.8 fF) during the experiments at any field, giving a magnetic field independent temperature stability of ± 1.6 mK at $T = 50$ mK.

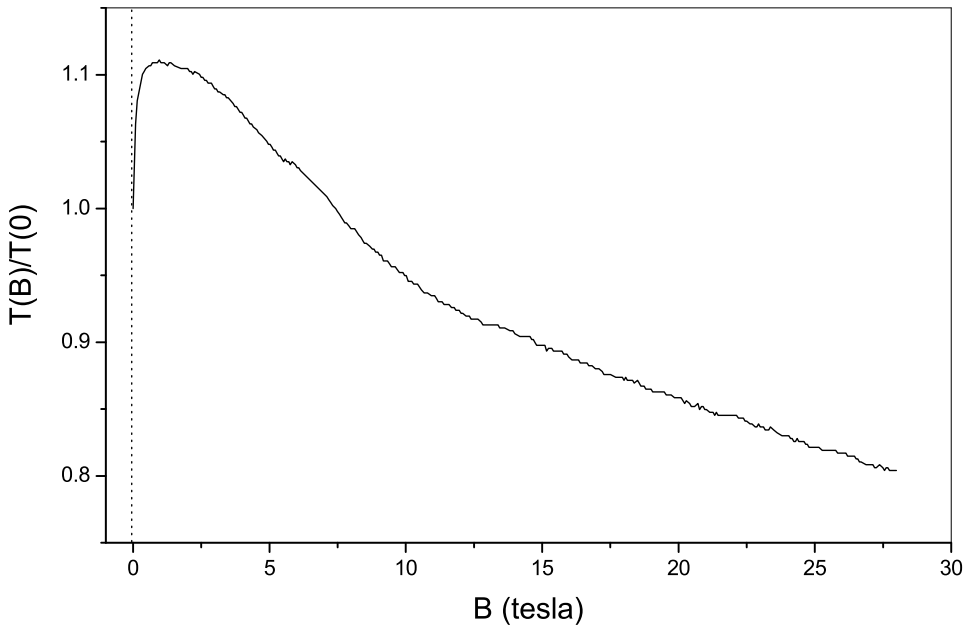

Figure A.2: Magnetoresistance error at $T \approx 50$ mK for the Ruthenium oxide thermometer of the Kelvinox$^{\mathrm{TM}}$ dilution refrigerator. Plotted is the erroneous temperature $T(B)$ given by the Ruthenium oxide sensor divided by the correct temperature $T(0)$ that is maintained during the field sweep experiment with the help of the dielectric constant thermometer.

The measurement of the magnetoresistance error of a thermometer was then performed as a field sweep experiment, where the temperature was regulated in a way that the capacitance of the dielectric constant thermometer remained constant. The erroneous temperature $T(B)$ given by the investigated thermometer, that was recorded during a temperature stabilized sweep, normalized with respect to the real temperature $T(0)$ then gives the magnetoresistance error of the thermometer at this special temperature, and can be used to calculate a correction formula, to compensate for this error

in later experiments. The magnetoresistance error of the Ruthenium oxide thermometer used in the toploading dilution fridge is shown in figure A.2. It turned out, that the sensitivity of our setup allowed a useful determination of the magnetoresistance error only in the range of maximum sensitivity of the dielectric constant thermometer at $T < 100$ mK. We therefore were only able to determine the magnetoresistance error for $T \approx 50$ mK. All attempts to do the same measurement above 100 mK failed due to the insufficient sensitivity of the dielectric constant thermometer.

A.2 Coulomb blockade thermometry

Considering the importance of magnetic field e. g. for experimental solid state physics, it is clear that there exists a great need for thermometric methods, which are insensitive to magnetic fields. At liquid Helium temperatures there exist some magnetic field insensitive resistive sensors like Zirconium oxynitride film resistors (Cernox^{TM}), which however develop a huge negative magneto-resistance for lower temperatures [73]. For the temperature range below 1 kelvin, accessible by ^{3}He evaporation cryostats or ^{3}He/^{4}He dilution cryostats there are only few methods available, which are moreover limited in their range of applicability. For T down to 550 mK one can use the temperature dependence of the vapor pressure of ^{3}He, which is magnetic field independent. This method provides a secondary thermometer, which has been included into the International Temperature Scale of 1990 (ITS90) [74]. For lower temperatures the anisotropy of the γ-ray emission of radioactive nuclei like ^{60}Co or ^{54}Mn is the most widely applied method, but it is a slow method and useful only below 50 mK. It is the temperature range between 50 and 550 mK, which is nowadays available in a great number of laboratories, that lacks a magnetic field insensitive way of measuring temperature for every day use.
Over the last couple of years, the possibility of using the Coulomb blockade effect for thermometry has been demonstrated to be suitable for real experimental situations [75, 76, 77]. The principle of CBT thermometry is to use the temperature dependence of the $I - V$ curve of a device consisting of several tunnel junctions connected in series. To see a noticeable and predictable temperature dependence due to Coulomb blockade, the charging energy $e^2/2C$ of one island between two tunnel junctions must be smaller than the average thermal energy $k_B T$. The $I - V$ curve for an array of tunnel junctions in this high temperature, or weak Coulomb blockade regime can be calculated with an approach similar to the orthodox theory where the tunneling rate of the system is affected by the charging by individual

electrons. For details see refs. [75, 76]. As a main result the differential conductance $G(V)$ of a linear array of tunnel junctions scaled by its asymptotic value $G_\mathrm{T} \equiv \lim_{V\to\pm\infty} G(V)$ in the first order approximation is equal to

$$G(V)/G_\mathrm{T} = 1 - \frac{\epsilon_\mathrm{C}}{k_\mathrm{B}T}\, g(\frac{eV}{Nk_\mathrm{B}T}) \tag{A.1}$$

with $\epsilon_\mathrm{C} \equiv [(N-1)/N]e^2/C$ and the number of tunnel junctions N. The function g determines the bias dependence of G/G_T:

$$g(x) = [x\sinh(x) - 4\sinh^2(x/2)]/8\sinh^4(x/2). \tag{A.2}$$

Deviations from (A.1) can occur due to non-uniformity in tunneling resistances in the array and due to higher order corrections, which can become important at very low temperatures. One way of determining the temperature from a $G(V)$ curve then is to use the half width $V_{1/2}$ of the conductance dip around zero bias, which equals

$$eV_{1/2}/Nk_BT \simeq 5.439, \tag{A.3}$$

according to (A.1). $V_{1/2}$ does not depend on any device parameters and it is not affected by stray capacitances or differing mutual capacitances of the array. Nonuniform tunneling resistances, which might modify (A.3) have a minor influence because the junctions in the sensors for low temperatures are rather large and can be fabricated with sufficient precision. Taking second order corrections to (A.1) into account, the result of (A.3) is somewhat modified for low temperatures:

$$V_{1/2} = (1 + 0.39211\frac{\Delta G}{G_\mathrm{T}})5.439Nk_\mathrm{B}T/e, \tag{A.4}$$

where $\Delta G/G_\mathrm{T}$ is the measured depth of the conductance curve ($\Delta G = G_\mathrm{T} - G(V=0)$). $V_{1/2}$ still gives the temperature, independent of any device parameters and therefore provides, in this mode of operation, a primary (calibration-free) thermometer. For a measurement of T from $V_{1/2}$ a full conductance curve has to be measured by sweeping the bias voltage, which can take up to a few minutes. A faster temperature reading is provided by a secondary mode, where the minimum value of the conductance dip at zero bias voltage is measured, which, in the first order approximation is equal to

$$\Delta G/G_\mathrm{T} = \frac{1}{6}\frac{\epsilon_\mathrm{C}}{k_\mathrm{B}T}. \tag{A.5}$$

As G/G_T via ϵ_C depends on the capacitances of the device, which may be subject to a certain variation due to the production process, this mode provides a secondary thermometer that needs to be calibrated versus one temperature reading in the aforementioned primary mode. Operated in this

secondary mode, a CBT can give temperature readings at a rate of about 1 sample/second with typically better than 10^{-3} resolution in temperature. A fast way of primary Coulomb blockade thermometry, which in practice however has turned out to be difficult to realize with competitive precision, was recently shown by Bergsten et al. [78].
Coulomb Blockade thermometers (CBTs) are nowadays commercially available and are routinely being used for measuring temperatures between 0.05 and 10 K. As for a precise temperature reading in primary mode the dip width $V_{1/2}$ has to be much larger than the typical noise level of the experiment, CBT sensors for very low temperatures, in particular in noisy experimental conditions like in high magnetic fields produced by resistive magnets, have to consist of a large number of tunnel junctions connected in series and are therefore more difficult to fabricate. In this paper we report of a first test of a new type of sensor consisting of 100 tunnel junctions in series and 10 of these series connected in parallel, giving a sensor with an overall resistance of about 300 kΩ. The sensors were produced by a standard two-angle shadow evaporation technique on an oxidized Si-substrate. Tunnel junctions were produced by vacuum evaporation of a 100 nm layer of Al, which was subsequently oxidized, and a 200 nm Cu-layer above, forming junctions of 1.5 μm^2 area and islands of an area of 30 μm^2. Further details of the fabrication process are described in ref. [77]. The size of a sensor is about $3 \times 2 \times 1.5$ mm^3. The characteristics of the CBTs have been found to be perfectly reproducible after thermal cycling to room temperature. As all of the CBT-measurements reported here were done below the superconducting critical temperature of aluminum, a minimum magnetic field (of the order of tens of milli-tesla) was applied to suppress superconductivity. This problem can be circumvented by packaging the sensors with a ferromagnetic support, for experiments which have no external magnetic field available. All temperature sensors were installed as described in the previous chapter, the CBT sensors were placed so that the magnetic field was oriented perpendicular to the aluminum films of the sensors. The measurements described here were done on one of four installed CBT sensors, the other three sensors were verified to give equivalent results.

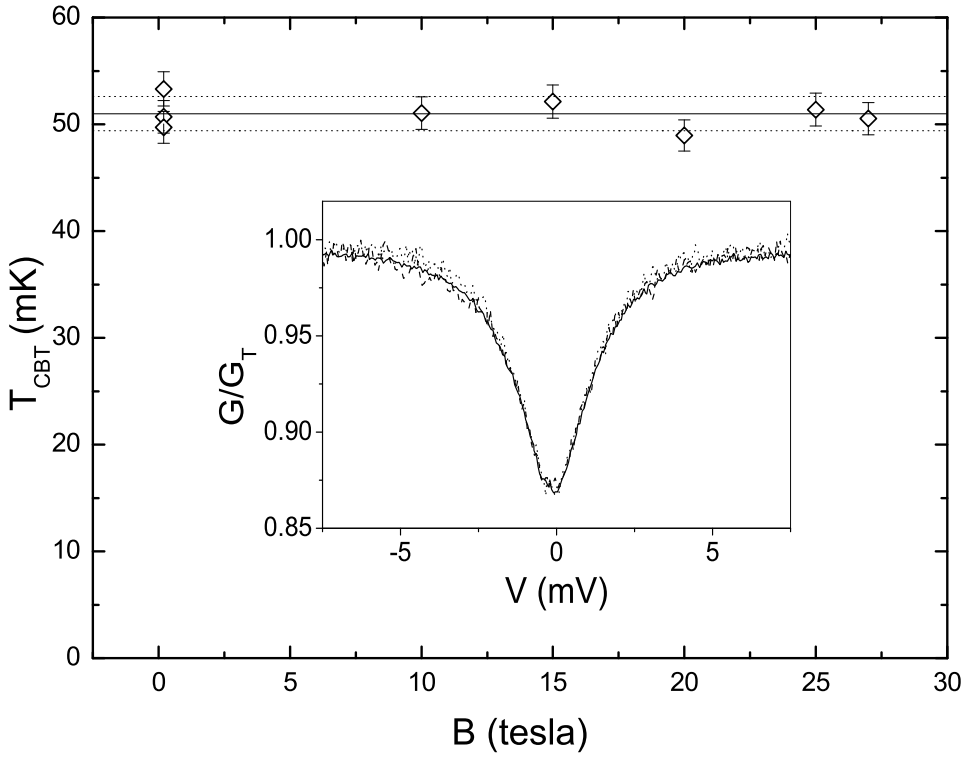

Figure A.3: Temperature readings by CBT taken in the primary mode for different magnetic fields at $T = 51 \pm 1.6$ mK, including the examples shown in the insert

Besides the check for well-known problems at milli-Kelvin temperatures such as poor thermalization or sensor heating, we especially looked for effects of a strong magnetic field onto the sensors. An earlier test at temperatures down to 0.4 kelvin and magnetic field up to 23 tesla had already shown negligible magneto-resistance of CBT and has been published elsewhere [79]. In the insert of figure A.3 we show three examples of the differential conductance measured at different magnetic fields. Deviations between the three curves are hardly visible and are significantly smaller than the noise level of the experiment. The mixing chamber temperature had been stabilized to 51 ± 1.6 mK for this experiment. The statistical error of the CBT temperature measurements amounts to $\pm 1.5\%$. As can be seen in figure A.3, the spread between the different temperatures measured by CBT does not exceed the temperature range that is given by the uncertainty of the dielectric constant thermometer. Within the precision of this measurement ($\pm 3\%$), which is rather low due to an extraordinarily high noise level of this type of experiments on resistive magnets, the CBT sensors are not affected by the

magnetic field.

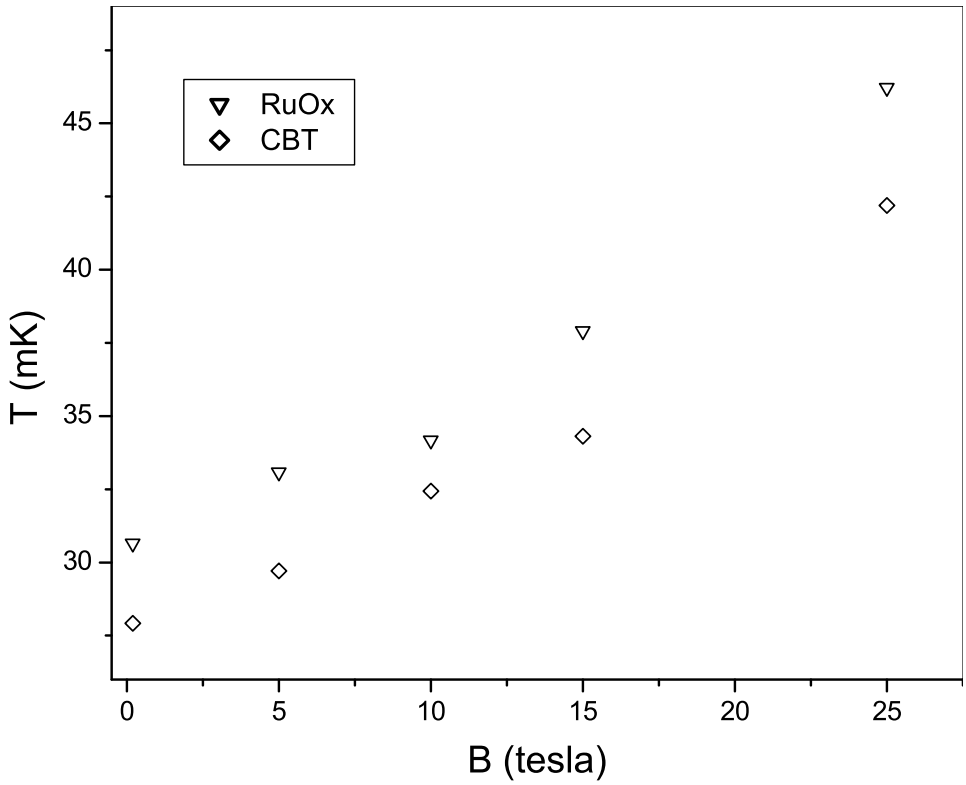

Figure A.4: CBT-temperatures for an unstabilized field run together with T derived from a Ruthenium oxide sensor which had been corrected with respect to its magneto-resistance error

In the second experiment the dilution fridge was run at its base temperature without regulation. As a temperature reference in this case we used a Ruthenium oxide thick film chip resistor supplied together with a zero-field calibration from Oxford Instruments. The magneto-resistance error of this sensor had been determined in the experiment described in the previous chapter, and could therefore be corrected for. It should be noted however, that the Ruthenium oxide thermometer was situated approximately 10 cm above the other sensors (but still in the diluted phase of the mixing chamber). As can be seen in figure A.4, the base temperature increases by a factor of ≈ 1.5 with B increasing from 0.2 to 27 tesla. This is due to the increase of mechanical vibrations and magnetic field noise of the resistive magnet, leading to an additional source of heating via eddy currents. Nevertheless, the two sensors show the same evolution of T with B with an almost field independent temperature difference of (3.1 ± 0.5) mK, which is partly due

to the large distance between the two sensors in the mixing chamber of the dilution cryostat. In this range of temperature bias self heating of the sensor can be partially responsible for the measured difference. Counterintuitively, the CBT-temperature reading in primary mode is lowered by this effect [80]. The fact that the offset between the two sensors is constant over the whole temperature range from 28 up to 43 mK shows that error due to slow thermalization of the sensor is unimportant.
In conclusion, we have confirmed experimentally the insensitivity of Coulomb blockade thermometers (CBTs) to magnetic field up to $B = 27$ T for temperatures around $T = 50$ mK with an experimental uncertainty of $\pm 3\%$. Problems due to slow thermalization could be shown to be negligible. CBT therefore provides a new, magnetic field independent thermometer, which is able to fill the gap between the working range of nuclear orientation and vapor pressure thermometers. While theoretically there are no indications for an effect due to even higher magnetic fields or lower temperatures, the usability at lower temperatures, which should be limited by slow thermalization and sensor self heating rests to be investigated.

Appendix B

Diffusive transport in tilted magnetic field

One can assume, that the magnitude of the corrections to σ_{xx} due to diffusive interference effects is proportional to the find again probability $P(t)$ either of one single electron (in the case of single particle corrections) or of two diffusing electrons (considering diffusive interaction corrections):

$$\Delta\rho_{xx} = |\rho_{xx}(\alpha) - \rho_{xx}(90^o)| \propto P(t) \tag{B.1}$$

$P(t)$ can be expressed as the ratio of the volume over which an electron is delocalized (${\lambda_d}^3$, λ_d is the de-Broglie wavelength) and the volume which is accessible to it by diffusive motion ($V = d \cdot L_x \cdot L_y = d \cdot \sqrt{D_{xx}t}\sqrt{D_{yy}t}$):

$$P(t) \simeq \frac{{\lambda_d}^3}{d \cdot \sqrt{D_{xx}D_{yy}} \cdot t} \propto \frac{1}{\sqrt{\sigma_{xx}\sigma_{yy}}} \tag{B.2}$$

Here we have used the Einstein relation, that relates the diffusion coefficients D_{ij} to the corresponding conductivities [81]:

$$\sigma_{ij} = 2e^2 N(E_F) D_{ij} \tag{B.3}$$

For the conductivity tensor in perpendicular magnetic field we have (chapter 2.1.1):

$$\underset{\approx}{\sigma} = \begin{pmatrix} \sigma_{xx} & \sigma_{xy} & 0 \\ -\sigma_{xy} & \sigma_{xx} & 0 \\ 0 & 0 & \sigma_{zz} \end{pmatrix} \qquad (\vec{B} = B \cdot \hat{e_z}) \tag{B.4}$$

The tensor of the measured conductivities $\underset{\approx}{\sigma'}$, which is fixed to the reference frame of the sample layer, can be calculated from $\underset{\approx}{\sigma}$ by a simple rotation by

α around x:

$$\underset{\approx}{\sigma'} = \begin{pmatrix} \sigma'_{xx} & \sigma'_{xy} & \sigma'_{xz} \\ \sigma'_{yx} & \sigma'_{yy} & \sigma'_{yz} \\ \sigma'_{zx} & \sigma'_{zy} & \sigma'_{zz} \end{pmatrix} = \underset{\approx}{D}^{-1} \cdot \underset{\approx}{\sigma} \cdot \underset{\approx}{D} =$$

$$\begin{pmatrix} 1 & 0 & 0 \\ 0 & \cos\alpha & -\sin\alpha \\ 0 & \sin\alpha & \cos\alpha \end{pmatrix} \cdot \begin{pmatrix} \sigma_{xx} & \sigma_{xy} & 0 \\ -\sigma_{xy} & \sigma_{xx} & 0 \\ 0 & 0 & \sigma_{zz} \end{pmatrix} \cdot \begin{pmatrix} 1 & 0 & 0 \\ 0 & \cos\alpha & \sin\alpha \\ 0 & -\sin\alpha & \cos\alpha \end{pmatrix} = \quad \text{(B.5)}$$

$$\begin{pmatrix} \sigma_{xx} & \sigma_{xy} \cdot \cos\alpha & \sigma_{xy} \cdot \sin\alpha \\ -\sigma_{xy} \cdot \cos\alpha & \sigma_{xx} \cdot \cos^2\alpha + \sigma_{zz} \cdot \sin^2\alpha & (\sigma_{xx} - \sigma_{zz}) \cdot \sin\alpha\cos\alpha \\ -\sigma_{xy} \cdot \sin\alpha & (\sigma_{xx} - \sigma_{zz}) \cdot \sin\alpha\cos\alpha & \sigma_{xx} \cdot \sin^2\alpha + \sigma_{zz} \cdot \cos^2\alpha \end{pmatrix}$$

With this we get for $P(t)$:

$$\begin{aligned} P(t) \propto \frac{1}{\sqrt{\sigma'_{xx}\sigma'_{zz}}} &= \frac{1}{\sqrt{\sigma_{xx}(\sigma_{xx} \cdot \cos^2\alpha + \sigma_{zz} \cdot \sin^2\alpha)}} \\ &= \frac{1}{\sqrt{\sigma_{xx}\sigma_{zz}[1 - (1 - \frac{\sigma_{xx}}{\sigma_{zz}})\cos^2\alpha]}} \end{aligned} \quad \text{(B.6)}$$

and for $\Delta\rho_{xx}(\alpha)$:

$$\Delta\rho_{xx}(\alpha) \propto \frac{1}{\sqrt{1 - A \cdot \cos^2\alpha}} \qquad (A = 1 - \frac{\sigma_{xx}}{\sigma_{zz}}) \quad \text{(B.7)}$$

Conclusions

The subject of this thesis is the quantum Hall effect observed in a new, strongly disordered two-dimensional electron system. In the system under investigation, that we call *impurity confined quantum well* throughout this work, we have been the first to report the observation of a fully developed integer quantum Hall effect. Our system, consisting of a n-type Gallium-Arsenide (GaAs) layer sandwiched between undoped GaAs, is a strongly disordered system with electron mobilities of about 2000 cm^2/Vs. An important difference to other GaAs-based systems is that the mean distance between ionized donors, that are mainly responsible for the disorder potential, and both the de-Broglie wavelength and the elastic mean free path of the electrons have values of around 20 nm. This means that our system has a dominating short range disorder potential, which is in contrast to most other GaAs-based two-dimensional systems, that show a long range disorder potential. This subtle difference has important consequences for the scaling behavior of the quantum Hall effect.

We have investigated the integer quantum Hall effect in this new two-dimensional electron system with respect to its dependence on layer thickness, temperature, and angle between the magnetic field and the layer plane. Changing the layer thickness of the doped layer, we change the effective 2D-carrier density and also the effective disorder of the system. We have realized a number of samples with conducting layers of thickness d = 27, 30, 34, 37, 40, 50 and 70 nm, each Si-doped with $n = 1.5{\cdot}10^{17}\mathrm{cm}^{-3}$. This leaves us with strongly localized systems for d = 27 and 30 nm, showing strong (Anderson) localization at zero magnetic field with an exponentially increasing resistance for decreasing temperature, and with only weakly localized, metallic systems for d = 34, 37, 40, 50 and 70 nm, showing a logarithmic increase of ρ_{xx} with temperature at zero magnetic field and an almost temperature independent resistivity at small magnetic fields. For all samples ρ_{xx} decreases with increasing magnetic field, going through a minimum at intermediate values of B, to increase again exponentially in high magnetic fields. Samples with d = 34, 37, 40 and 50 nm show a fully developed quantum Hall effect with

a Hall plateau at $\rho_{xy} = h/2e^2$ at intermediate magnetic fields. They even show the onset of a quantum Hall state at $\rho_{xy} = h/e^2$, which is due to the spin splitting of the lowest Landau level. In low mobility systems this has not been observed before as here, due to the small g-factor and the larger disorder broadening, the two spin-split Landau levels overlap strongly. For even stronger magnetic field, the transition to the high field insulating state takes place, where all samples again become insulating, and ρ_{xx} increases exponentially with B.

We have shown that the longitudinal resistance ρ_{xx} in the quantum Hall minimum of samples with $d = 40$ and 50 nm is governed by variable range hopping with a hopping exponent of $p \approx 0.6$. This value of p is slightly larger than the value predicted by theory for variable range hopping in a Coulomb gap ($p = 0.5$). We can explain this difference by assuming a dependence of the localization length ξ on the energy in the Coulomb gap, which should exist in the case of Anderson localization.

Recent developments in the field of two parameter scaling theory (the theory of localization in magnetic field) have resulted in quantitative predictions for the flow of the conductivities of a two-dimensional electron system in a renormalization group description. A representation of this so called renormalization group flow, a plot of σ_{xx} versus σ_{xy} showing the evolution of a point in the (σ_{xy},σ_{xx})-plane for increasing system size L (or decreasing temperature T) is usually called the flow diagram of the quantum Hall effect. We were able to verify this flow experimentally with the magnetotransport data of our samples by plotting the conductivities measured as a function of temperature at different magnetic fields. Our experimental data agree well with theory over a large temperature range from 4.2 K down to 50 mK and with a level of precision that has not been reported before.

As the electronic mean free path in our systems is smaller than the extension of the system in z-direction, transport perpendicular to the layer is diffusive. This turns out to have rather drastic consequences for the behavior of the quantum Hall effect in tilted magnetic field, that we have investigated in detail for two of our samples. The observed behavior is atypical compared to what is usually observed in high mobility systems, where the quantum Hall effect structures just shift to higher fields with a $1/\cos(\alpha)$-characteristics up to angles close to 90^o. We can state clearly from our experiments that our systems do not follow this behavior, but that they show a much weaker dependence on the angle than the expected $1/\cos(\alpha)$-dependence. Our systems therefore do not seem to be sensitive only to the perpendicular component $B_\perp = B \cdot \cos(\alpha)$ of the magnetic field, but more to the total magnetic field B.

In a separate project dealing with the measurement of temperature below

$T = 100$ mK in high magnetic fields up to $B = 28$ T, we were able show that the commonly used Ruthenium oxide thermometers develop a considerable magnetoresistance, resulting in an error of up to 20% in the temperature reading, if this effect is not being corrected for. We demonstrated that a new kind of thermometer, which is based on the Coulomb blockade effect, is suitable for temperature measurement at milli-kelvin temperatures even in noisy environments like on resistive magnets. We were further able to show that this Coulomb blockade thermometer (CBT) is insensitive to magnetic field up to 28 tesla.

Zusammenfassung

In dieser Arbeit wurde der ganzzahlige Quanten Hall Effekt in einem neuen, stark ungeordneten System umfassend beschrieben und charakterisiert. Bei dem untersuchten, neuartigen Halbleitersystem handelt es sich um einen Quantentrog, der im wesentlichen aus einer stark n-dotierten Schicht Galliumarsenid (GaAs) besteht, die in undotiertes GaAs eingebettet ist. Das freie Elektronengas, das sich in dieser Struktur bildet, ist am Ort maximaler Unordnung gebunden, und zeigt dementsprechende Transportparameter mit einer mittleren freien Weglänge von etwa 20 nm und einer Ladungsträgermobilität von 2000 cm^2/Vs. Mit diesem System konnten wir einen GaAs-basierten Quantentrog realisieren, in dem ein überwiegend kurzreichweitiges Unordnungspotential dominiert; dies hat bedeutende Konsequenzen für das Skalierungsverhalten des Quanten Hall Effekts.
Wir haben in einer Reihe von Proben mit verschiedenen Schichtdicken den ganzzahligen Quanten Hall Effekt beobachtet und bezüglich seiner Abhängigkeit von der Breite des Quantentrogs, der Temperatur, und des Winkels zwischen der Ebene des Elektronengases und dem Magnetfeld untersucht. Proben mit Dicken der n-dotierten Schicht von $d = 27$, 30, 34, 37, 40, 50 und 70 nm, jeweils mit einer Elektronenkonzentration von $1.5 \cdot 10^{17}\mathrm{cm}^{-3}$ wurden per Molekularstrahlepitaxie hergestellt. Die dünnsten der Proben ($d = 27$, 30 nm) zeigten isolierendes Verhalten (der spezifische Widerstand der Proben nahm bei abnehmender Temperatur exponentiell zu) um $B = 0$. Dickere Proben ($d = 34$, 37, 40, 50, 70 nm) zeigten eher metallischen Charakter, mit konstantem Widerstand bei abnehmender Temperatur. Mit zunehmenden Magnetfeld nahm in allen Proben der elektrische Längswiderstand ab, zeigte ein Minimum bei mittlerem Feld um $B = 8$ T, um in starken Magnetfeldern, einem Isolator entsprechend, exponentiell anzusteigen. In den Proben mit $d = 34$, 37, 40 und 50 nm konnte ein voll ausgebildeter Quanten-Hall Effekt, mit einem perfekt flachen Plateau im Hallwiderstand bei $\rho_{xy} = h/2e^2$ und einem Minimum im Längswiderstand mit $\rho_{xx} = 0$ beobachtet werden. In diesen Proben zeigte sich zusätzlich bei Feldern um $B = 12$ T der Ansatz eines Quanten-Hall Plateaus bei $\rho_{xy} = h/e^2$, was durch die Spinaufspaltung

des untersten Landauniveaus verursacht sein muß und damit sehr ungewöhnlich für ein stark ungeordnetes, GaAs basiertes System ist, da hier die zwei spinaufgespaltenen Landauniveaus aufgrund der großen Verbreiterung der Niveaus und der geringen Zeemanaufspaltung, Konsequenz eines sehr kleinen g-Faktors von -0.44, sehr stark überlappen. In GaAs-basierten Proben mit ähnlichen Mobilitäten ist unseres Wissens nach bisher noch kein Anzeichen von Hall Quantisierung bei ungeraden Quantenzahlen beobachtet worden.
Wir konnten zeigen, daß der Transportmechanismus im Bereich des Quanten-Hall Minimums der Proben mit $d = 40$ und 50 nm durch Hopping-Leitung in einem Coulomb-Gap dominiert ist. Der Hopping-Exponent von $p \approx 0.6$, den wir bei verschieden Werten des Magnetfelds im Quanten-Hall Minimum der beiden Proben messen konnten, ist deutlich größer als der Wert ($p = 0.5$) der von der Theorie für Hopping-Leitung in einem Coulomb-Gap vorhergesagt wird. Unter der Annahme, daß die Lokalisierunglänge der Elektronen von der Energie ihres lokalisierten Zustands im Coulomb-Gap über ein Potenzgesetz abhängt, was für Systeme mit starker (Anderson) Lokalisierung vorstellbar ist, konnten wir ein Modell zur Erklärung von Hopping-Exponenten $p \geq 0.5$ ausarbeiten, und waren somit in der Lage unsere experimentellen Ergebnisse theoretisch zu beschreiben.
Neuere Entwicklungen in der Zwei-Parameter Skalentheorie der Lokalisierung (der Theorie der Lokalisierung im Magnetfeld) haben vor kurzem zu ersten quantitativen Vorhersagen für den "Fluß " der beiden unabhängigen Komponenten des Leitfähigkeitstensors $(\sigma_{xx}, \sigma_{xy})$ im Rahmen der Beschreibung per Renormierungsgruppe geführt. Eine einfache graphische Darstellung dieses sogenannten Renormierungsgruppenflusses, ein graphische Auftragung von σ_{xx} gegen σ_{xy}, die die Entwicklung eines Punktes in der $(\sigma_{xx}, \sigma_{xy})$-Ebene mit zunehmender Größe L (bzw. abnehmender Temperatur T) des Systems angibt, wird gewöhlich als das Flußdiagramm des Quanten-Hall Effekts bezeichnet. Wir konnten dieses Flußdiagramm experimentell, durch Auftragung von σ_{xx} gegen σ_{xy}, gemessen bei fixem Magnetfeld als Funktion der Temperatur, verifizieren. Unsere Daten stimmen quantitativ mit den theoretischen Vorhersagen über einen weiten Temperaturbereich (4.2 K $\rightarrow$ 50 mK) mit einer bisher nicht erreichten Präzision überein.
Da die mittlere freie Weglänge der Leitungselektronen in unseren Proben kleiner ist als die Ausdehnung des freien Elektronengases in z-Richtung, muß der elektronische Transport entlang z als diffusiv angenommen werden. Dies hat drastische Konsequenzen für das Verhalten des Quanten-Hall Effekts wenn die Probe gegen das Magnetfeld geneigt ist. Wir haben die Abhängigkeit vom Neigungswinkel α der Probe systematisch untersucht, und sind auf ein überraschendes Ergebnis gestoßen: In einem perfekt zweidimensionalen System sollte der elektronische Transport nur von der Komponente

des Magnetfelds senkrecht zur Ebene des zweidimensionalen Elektronengases abhängen. In einer Auftragung gegen das gesamte Magnetfeld B sollten daher alle Strukturen, z. B. das Minimum im Längswiderstand ρ_{xx} mit einer $1/\cos(\alpha)$-Charakteristik zu höheren Feldern verschoben werden. Es kann klar gesagt werden, daß unsere Proben dieses Verhalten nicht zeigen, sondern daß sie eine sehr viel schwächere Abhänbgigkeit von Neigungswinkel zeigen, und somit nicht nur gegen die Normalkomponente $B_\perp = B \cdot \cos(\alpha)$ des Magnetfelds, sondern eher gegen das totale Magnetfeld B empfindlich sind.
Gegenstand eines weiteren, separaten Projekts war die Messung der Temperatur bei Werten um $T = 50$ mK in hohen Magnetfeldern bis zu $B = 28$ T. Mit Hilfe eines magnetfeldunabhängigen Kapazitätsthermometers konnten wir zeigen, daß die weitverbreiteten und vielbenutzten Rutheniumoxid-Schichtwiderstände in diesem Temperaturbereich einen erheblichen Magnetowiderstand entwickeln, was zu Fehlern von bis zu 20% in der Temperaturmessung führen kann, wenn dieser Fehler nicht korrigiert wird. Wir konnten weiterhin zeigen, daß ein neuartiges Thermometer, das auf dem Effekt der Coulombblockade basiert, zur Temperaturmessung bei $T = 50$ mK in Magnetfeldern bis $B = 28$ T auch in relativ verrauschten experimentellen Situationen geeignet ist. Des weiteren konnten wir zeigen, daß besagtes Coulombblockadethermometer (CBT) auch von Magnetfeldern von $B = 28$ T selbst bei tiefen Temperaturen um $T = 50$ mK in seiner Funktion nicht vom Magnetfeld beeinflußt wird.

Acknowledgments

First of all I would like to thank Prof. P. Wyder, my supervisor, for giving me the possibilty to perform this work at the Grenoble High Magnetic Field Lab, and for his continuous interest and motivations during this thesis ("Quantelt es schon ?").
Vielen Dank and Prof. Schatz, der sich bereiterklärt hat als Koreferent und Prüfer zu fungieren. Ebenso vielen Dank an Prof. Dehnen, der den Vorsitz der Prüfungskomission übernommen hat
Dank je wel to Louis Jansen, my second supervisor, who always had an open ear for questions and experimental Problems.
Я очень благодарен Сергею Мурзину, с которым я выполнил большую часть экспериментов, описанных в этой работе.
Thanks also to Jukka Pekola, Juha Kauppinen and Janne Suoknuuti, who I had the pleasure to explore the world of Coulomb blockade thermometry with.
A big thanks of course to Peter van der Linden, who was a great help in cryogenic problems.
Thanks also to Nicolas Freytag, Enno Bibow, David Schäffer and Phillipe Lafarge for sharing with me the *diluette*, the pump group, or both.
I am grateful to Laurent Levy for magnet time in his bipolar superconducting magnet.
Für die Präparation unserer Proben danke ich Karl Eberl, Birgit Lemke, Claudia Didschies und Frank Schartner am MPI in Stuttgart.
Vielen Dank ebenfalls an Brigitte Indigo, Uschi Leitenberger und Ingrid Giradet-Beier für ihre Unterstützung in allen administrativen Fragen.
Thanks to Duncan Maude for proofreading the manuscript.
Merci beaucoup a tous mes amis (au laboratoire et en dehors) pour leur soutien et pour beaucoup d'heures passés ensemble, en montagne ou ailleurs.

Bibliography

[1] K. v. Klitzing, G. Dorda, and M. Pepper, Phys. Rev. Lett. **45**, 494 (1980) 5

[2] D. C. Tsui, H. L. Störmer, and A. C. Gossard, Phys. Rev. Lett. **48**, 1559 (1982) 5

[3] M. A. Zudov, R. R. Du, J. A. Simmons, and J. L. Reno, Phys. Rev. B **64**, 201311 (2001) 5

[4] U. F. M. Janßen, O. Viehweger and J. Hajdu, Introduction to the Theory of the Integer Quantum Hall Effect, VCH (1994) 9, 12

[5] D. Yoshioka, The Quantum Hall Effect, Springer (2002) 12

[6] R. R. Gerhardts, Z. Phys. B **21**, 275, 285 (1975) 12

[7] D. J. Thouless, Phys. Rev. Lett. **39**, 1167 (1977) 16

[8] J. T. Chalker and P. D. Coddington, J. Phys. C **21**, 2665 (1988) 16

[9] A. M. M. Pruisken, Phys. Rev. Lett. **61**, 1297 (1988) 17

[10] R. B. Laughlin, Phys. Rev. B **52**, 2304 (1984) 18

[11] D. E. Khmelnitskii, Phys. Lett. **106A**, 182 (1984) 18

[12] B. Huckestein, Phys. Rev. Lett. **84**, 3141 (2000) 18

[13] R. J. Hughes, J. T. Nicholls, J. E. F. Frost, E. H. Linfield, M. Pepper, C. J. B. Ford, D. A. Ritchie, G. A. C. Johnes, E. Kogan, and M. Karvey, J. Phys. Cond. Matt. **6**, 4763 (1994) 18

[14] R. B. Laughlin, Phys. Rev. B **23**, 5632 (1981) 19, 20

[15] B. I. Halperlin, Phys. Rev. B **25**, 2185 (1982) 19

[16] J. E. Avron, D. Osadchy, and R. Seiler, Physics Today **56**, 38 (2003) 20

[17] R. E. Prange and S. M. Girvin (editors), The Quantum Hall Effect, Springer (1987) 20, 26, 27

[18] M. Büttiker, Phys. Rev. B **38**, 9375 (1988) 20

[19] L. M. Roth and P. N. Argyres, Magnetic Quantum effects, in R. K. Willardson and A. C. Beer (editors), Semiconductors and Semimetals 1, page 159, Academic Press, New York (1966) 24

[20] D. J. Thouless, Phys. Rep. **13C**, 93 (1974) 24

[21] F. Wegner, Z. Phys. B **25**, 327 (1976) 24

[22] E. Abrahams, P. W. Anderson, D. C. Licardello, and T. V. Ramakrishnan, Phys. Rev. Lett. **42**, 673 (1979) 24, 31, 32

[23] H. Levine, S. B. Libby, and A. M. M. Pruisken, Nuclear Physics B **240**, 30 (1984) 26

[24] H. Levine, S. B. Libby, and A. M. M. Pruisken, Nuclear Physics B **240**, 49 (1984) 26

[25] H. Levine, S. B. Libby, and A. M. M. Pruisken, Nuclear Physics B **240**, 71 (1984) 26

[26] D. E. Khmelnitskii, JETP Lett. **38**, 552 (1983) 26, 27, 60

[27] S. Kivelson, D. Lee, and S. Zhang, Phys. Rev. B **46**, 2223 (1992) 27

[28] C. A. Lütken and G. G. Ross, Phys. Rev. B **48**, 2500 (1993) 27, 28

[29] F. Hohls, U. Zeitler, and R. J. Haug, Phys. Rev. Lett. **88**, 036802 (2002) 28

[30] B. P. Dolan, Nucl. Phys. B **554**, 487 (1999) 29, 30, 60

[31] A. M. Dykhne and I. M. Ruzin, Phys. Rev. B **50**, 2369 (1994) 29

[32] M. Hilke, D. Shahar, S. Song, D. Tsui, Y. Xie, and M. Shayegan, Europhys. Lett. **46**, 775 (1999) 29

[33] C. P. Burgess and C. A. Lütken, Phys. Lett. B **451**, 365 (1999) 29

[34] N. Taniguchi, cond-mat/9810334 (1998) 29

[35] G. Bergman, Physics Reports **107**, 1 (1984) 31, 32, 33

[36] B. L. Altshuler, D. Khmelnitzkii, A. L. Larkin, and P. A. Lee, Phys. Rev. B **22**, 5142 (1980) 33, 34

[37] S. Hikami, Phys. Rev. B **24**, 2671 (1981) 33

[38] S. S. Murzin, M. Weiss, A. G. M. Jansen, and K. Eberl, Phys. Rev. B **64**, 233309 (2001) 33, 39

[39] B. L. Altshuler and A. G. Aronov, in A. L. Efros and M.Pollak (editors), Electron-Electron Interaction in Disordered Systems, North-Holland, Amsterdam (1987) 33

[40] S. S. Murzin, JETP Lett. **67**, 216 (1998) 34, 64

[41] A. Miller and E. Abrahams, Phys. Rev. **120**, 745 (1960) 34

[42] B. I. Shklovskii and A. L. Efros, Electronic Properties of Doped Semiconductors, Springer (1984) 34, 35, 37

[43] A. L. Efros and B. I. Shklovskii, J. Phys. C **8**, L49 (1975) 37

[44] V. L. Nguyen, Sov. Phys. Semicond. **18**, 207 (1984) 38

[45] G. Ebert, K. von Klitzing, C. Probst, E. Schubert, K.Ploog, and G. Weimann, Solid State Comm. **45**, 625 (1983) 38

[46] D. G. Polyakov and B. I. Shklovskii, Phys. Rev. B **48**, 11167 (1993) 38

[47] W. F. van Keuks, X. L. Hu, H. W. Jiang, and A. J. Dahm, Phys. Rev. B **56**, 1161 (1997) 39

[48] M. E. Gershensen, Y. B. Khavin, D. Reuter, and et al., Phys. Rev. Lett **85**, 1718 (2000) 39

[49] N. Markvić, C. Christiasen, D. E. Grupp, and et al, Phys. Rev. B **62**, 2195 (2000) 39

[50] E. Epperlein, M. Schreiber, and T. Vojta, Phys. Rev. B **56**, 5890 (1997) 39

[51] http://ghmfl.grenoble.cnrs.fr/ 42

[52] F. Pobell, Matter and Methods at Low Temperatures, Springer, 2nd edition (1995) 42, 75

[53] J. C. Maan, T. Englert, C. Uihlein, H. Künzel, A. Fischer, and K. Ploog, Solid State Comm. **47**, 383 (1983) 45

[54] S. Ishida and E. Otsuka, J. Phys. Soc. Japan **43**, 124 (1977) 45

[55] S. M. Sze, Physics of Semiconductor Devices, Wiley (1981) 46, 47

[56] K. Eberl, private communication 46

[57] G. Li and C. Jagadish, Appl. Phys. Lett. **70**, 90 (1997) 48

[58] K. I. Amirkhanov, P. I. Bashirov, and A. Y. Mollaev, Sov. Phys. Semicond. **4**, 1616 (1970) 49

[59] S. M. Girvin, The Quantum Hall Effect: Novel Excitations and Broken Symmetries, cond-mat/9907002 50

[60] S. S. Murzin, A. G. M. Jansen, and P. v. d. Linden, Phys. Rev. Lett. **80**, 2681 (1998) 51

[61] S. S. Murzin, I. Claus, A. G. M. Jansen, and K. Eberl, Phys. Rev. B **59**, 7330 (1999) 51, 64

[62] S. S. Murzin, I. Claus, and A. G. M. Jansen, JETP Lett. **68**, 327 (1998) 51

[63] S. D. Sarma and A. Pinczuk (editors), Perspectives in Quantum Hall Effects, Wiley (1997) 51

[64] C. T. Liang, C. F. Huang, Y. M. Cheng, T. Y. Huang, Y. H. Chang, and Y. F. Chen, Chinese Journal of Physics **39**, L305 (2001) 63

[65] S. S. Murzin, M. Weiss, A. G. M. Jansen, and K. Eberl, Phys. Rev. B **66**, 233314 (2002) 64

[66] A. G. Zabrodskii and K. N. Zinoveva, Sov. Phys. JETP **59**, 425 (1984) 65

[67] R. W. Hamming, Digital Filters, Dover, 3rd edition (1998) 66

[68] B. Huckestein, Rev. Mod. Phys. **67**, 357 (1995) 67

[69] S. W. Hwang, H. P. Wei, L. W. Engel, D. C. Tsui, and A. M. M. Pruisken, Phys. Rev. B **48**, 11416 (1993) 67

[70] M. Watanabe, M. Morishita, and Y. Ootuka, Cryogenics **41**, 143–148 (2001) 75

[71] P. J. Reijntjes, W. van Rijswijk, G. A. Vermeulen, and G. Frossati, Rev. Sci. Instr. **57**, 1413 (1986) 76

[72] S. A. J. Wiegers, R. Jochemsen, C. C. Kranenburg, and G. Frossati, Rev. Sci. Instr. **58**, 2274 (1987) 76

[73] R. Rosenbaum, B. Brandt, S. Hannahs, T. Murphy, E. Palm, and B.-J. Pullum, Physica B **294-295**, 489 (2001) 79

[74] H. Preston-Thomas, Metrologia **27**, 3 (1990) 79

[75] J. P. Pekola, K. P. Hirvi, J. P. Kauppinen, and M. A. Paalanen, Phys. Rev. Lett. **73**, 2903 (1994) 79, 80

[76] S. Farhangfar, K. P. Kirvi, J. P. Kauppinen, J. P. Pekola, J. J. Toppari, D. V. Averin, and A. N. Korotkov, J. Low Temp. Phys. **108**, 191 (1997) 79, 80

[77] J. P. Kauppinen, K. T. Loberg, A. J. Manninen, J. P. Pekola, and R. V. Voutilainen, Rev. Sci. Instr. **69**, 4166 (1998) 79, 81

[78] T. Bergsten, T. Claeson, and P. Delsing, Appl. Phys. Lett. **78**, 1264 (2001) 81

[79] J. P. Pekola, J. J. Toppari, J. P. Kauppinen, K. M. Kinnunen, A. J. Manninen, and A. G. M. Jansen, J. Appl. Phys. **83**, 5582 (1998) 82

[80] J. P. Kauppinen and J. P. Pekola, Phys. Rev. B **54**, 8353 (1996) 84

[81] S. Chakravarty and A. Schmid, Phys. Rep. **140**, 193 (1986) 85